Johannes M. Tändl, Dipl.-Ing.

Precipitation and recrystallization kinetics in a novel Al-Mg-Sc-Zr alloy

DOCTORAL THESIS

to achieve the university degree of
Doktor der technischen Wissenschaften
submitted to

Graz University of Technology

Supervisor

Prof. Dr. Maria Cecilia Poletti
Institute of Materials Science and Welding
Graz University of Technology

Graz, November 2016

Für Strahli-san

AFFIDAVIT

I declare that I have authored this thesis independently, that I have not used other than declared sources/resources, and that I have explicitly indicated all material which has been quoted either literally or by content from the sources used. The text document uploaded to TUGRAZonline is identical to the present doctoral thesis.

Date	Signature

Preface

This PhD thesis was accomplished at the Institute of Materials Science and Welding at Graz University of Technology and was submitted to the Faculty of Mechanical Engineering and Economic Sciences to achieve the academic degree *Doktor der technischen Wissenschaften*. The work was supervised by Prof. Dr. Maria Cecilia Poletti.

Financial support was provided by the Austrian Research Promotion Agency FFG. The project OscAR *"Oesterreichische supply-chain für Aluminium Rumpfkomponenten"* with the project number 839002 was funded within the program TAKE OFF. The Synchrotron experiments were performed at the Austrian SAXS beamline at Elettra Sincrotrone Trieste under the proposal number 20130138. The transmission electron microscopy investigations were carried out at the Institute of Electron Microscopy and Nanoanalysis and the Austrian Centre for Electron Microscopy and Nanoanalysis at Graz University of Technology. Parts of this work result of a research stay at the Department of Materials Engineering at The University of Tokyo in Japan which was financially supported by Graz University of Technology.

Major parts of this thesis and the outcome of additional activities in the project were published in written and oral form, as listed below.

Journals and international conference proceedings:

1. J. Taendl, C. Poletti, "Characterization of electron beam and friction stir welds in a novel Al-Mg-Sc-Zr alloy", Proceedings of the 10^{th} International Conference on Trends in Welding Research, pp 313-316, 2016.

2. J. Taendl, S. Nambu, J. Inoue, T. Koseki, C. Poletti, "Kinetics of hardening and softening in an Al-Mg-Sc-Zr alloy: Analyses of the driving pressure and Zener pinning effect", in submission.

3. M. Dikovits, J. Taendl, C. Poletti, "Deformation behaviour of a rapidly solidified Al-Mg-Sc-Zr alloy", in submission.

4. J. Taendl, A. Orthacker, H. Amenitsch, G. Kothleitner, C. Poletti, "Influence of the degree of scandium supersaturation on the precipitation kinetics of rapidly solidified Al-Mg-Sc-Zr alloys", Acta Mater., vol 117, pp 43-50, 2016.

5. J. Taendl, C. Poletti, "Influence of Al_3(Sc,Zr) precipitates on the deformability and friction stir welding behavior of Al-Mg-Sc-Zr alloys", BHM Berg- und hüttenmännische Monatshefte, vol 161, pp 330-333, 2016.

6. J. Taendl, S. Nambu, A.Orthacker, G. Kothleitner, J. Inoue, T. Koseki, C. Poletti, "In-situ observation of recrystallization in an AlMgScZr alloy using confocal laser scanning microscopy", Mater. Charact., vol 108, pp 137-144, 2015.

7. A. Orthacker, G. Haberfehlner, J. Taendl, C. Poletti, G. Kothleitner, "Analytical electron tomographic investigation of an aluminium alloy with nano-precipitates", ASEM Workshop Advanced Electron Microscopy, pp 39, 2015.

8. J. Taendl, M. Dikovits, C. Poletti, "Investigation of the hot deformation behavior of an Al-Mg-Sc-Zr alloy under plane strain condition", Key Eng. Mater., vols 611-612, pp 76-83, 2014.

9. J. Taendl, F. Palm, K. Anders, R. Gradinger, C. Poletti, "Investigation of the precipitation kinetics of a new Al-Mg-Sc-Zr alloy" Mater Sci. Forum, vols 794-796, pp 1038-1043, 2014.

10. A. Orthacker, G. Haberfehlner, J. Taendl, C. Poletti, G. Kothleitner, "Tomography in analytical transmission electron microscopy of nanomaterials", European Workshop on Spatially Resolved Electron Spectroscopy, pp 29, 2014.

Talks at international conferences:

1. J. Taendl, C. Poletti, "Characterization of electron beam and friction stir welds in a novel Al-Mg-Sc-Zr alloy", 10^{th} International Conference on Trends in Welding Research, Tokyo, Japan, 2016.

2. J. Taendl, S. Nambu, A.Orthacker, G. Kothleitner, J. Inoue, T. Koseki, C. Poletti, "Precipitation and recrystallization in a rapidly solidified AlMgScZr alloy", 15^{th} International Conference on Aluminum Alloys ICAA15, Chongqing, China, 2016.

3. J. Taendl, C. Poletti, "Investigations on precipitation and recrystallization kinetics in Al-Mg-Sc-Zr alloys using in-situ methods", ASMET Forum, Leoben, Austria, 2016

4. J. Taendl, S. Nambu, A.Orthacker, G. Kothleitner, J. Inoue, T. Koseki, C. Poletti, "In-situ study of the recrystallization behavior of an age hardening Al-Mg-Sc-Zr alloy", International Conference on Processing and Manufacturing of advanced Materials THERMEC, Graz, Austria, 2016 (invited).

5. J. Taendl, A. Huetter, C. Poletti, "Subjecting a novel AlMgScZr alloy to electron beam and friction stir processing", International Insitute of Welding IIW Annual Assembly, Seoul, Korea, 2014.

6. J. Taendl, F. Palm, K. Anders, R. Gradinger, C. Poletti, "Investigation of the precipitation kinetics of a new Al-Mg-Sc-Zr alloy", 14^{th} International Conference on Aluminum Alloys ICAA14, Trondheim, Norway, 2014.

7. J. Taendl, M. Dikovits, C. Poletti, "Investigation of the hot deformation behavior of an Al-Mg-Sc-Zr alloy under plane strain condition", ESAFORM 2014, Espoo, Finland, 2014.

8. J. Taendl, F. Palm, K. Anders, C. Poletti, C. Sommitsch, "Investigation of the Al_3(Sc,Zr) precipitation behavior of a novel AlMgScZr alloy", 60. Metallkunde Jubilläumskolloquium, Lech am Arlberg, Austria, 2014

"Thank you quote"
(someone very smart)

During the work on this thesis and my entire life I was supported by wonderful people.
Thank you for everything!

Abstract

Al-Mg alloys modified with Sc and Zr possess superior mechanical properties than conventional Al-Mg alloys while maintaining the beneficial materials characteristics such as weldability and corrosion behavior. This unique combination of materials properties makes this type of alloys a promising candidate for applications in aircraft fuselage components. However, so far there exist no Al-Mg-Sc-Zr alloys that reach the required strength level of the currently used Al-Cu-Mg alloys. In this study, a newly developed material produced using an alternative rapid solidification process is investigated.

This thesis deals with the fundamental characterization of a novel Al-Mg4-Sc0.4-Zr0.12 alloy produced on industrial belt-casting equipment. The precipitation of the strengthening Al_3(Sc,Zr) phase is studied in different materials conditions with respect to the degree of Sc-supersaturation, temperature and time. In a temperature range between 250°C and 400°C, the hardness evolution is correlated to in-situ synchrotron X-ray diffraction measurements and the precipitate evolution is studied using high-resolution scanning transmission electron microscopy. The recrystallization kinetics of cold deformed material is analyzed by means of in-situ confocal laser scanning microscopy, electron backscatter diffraction, and energy filtered transmission electron microscopy. The results are correlated to the hardness evolution during ageing between 325°C and 500°C for 60 min.

The age hardening effect from Al_3(Sc,Zr) precipitates occurs slightly faster and is considerably more pronounced at larger solute Sc-content. The Al_3(Sc,Zr) precipitate size at a given ageing temperature is not affected by the degree of Sc-supersaturation, while their volume fraction and number density increase with the Sc-content in solution. Peak ageing is achieved at temperatures from 325°C within 180 min. Precipitation and recrystallization occur simultaneously during ageing of cold deformed material. Full recrystallization is not observed and the grain boundary migrations cease once the Zener pinning effect from growing Al_3(Sc,Zr) precipitates is strong enough. The annealing duration to reach this critical time is reduced with increasing ageing temperature and is observable in-situ using confocal laser scanning microscopy. The softening kinetics follows a power-law relation and reaches a steady state when significant Zener pinning is exerted.

Contents

1 Introduction

The civil aircraft market showed a considerable growth over the last decades and is expected to grow further substantially in the near future. The market performance of the civil aircraft industry is put into numbers in Fig. 1.1 by means of the worldwide annual revenue-passenger kilometers (RPK), i.e. the total number of air kilometers travelled by paying customers. According to this forecast [1], the RPK will double in the next 20 years leading to an increasing need for civil aircrafts. In the same market study, a total need for 32 600 aircrafts is expected until 2034, amongst which around 23 000 single-aisle types. This considerable demand for new aircrafts, in consequence, leads to a significant need for structural materials (Fig. 1.2).

When considering the fraction of materials used in Airbus aircrafts over the last 50 years, Al-alloys were the dominant material until the latest twin-aisle aircraft A350 launched in 2014, as shown in Fig. 1.3. For this long-range aircraft a large volume of composite materials, for example carbon-fiber reinforced plastics (CFRP), was used for structural components at the expense of Al-alloys. Despite the higher materials price, apparently, composite materials are profitable over the entire life cycle of long-range airplanes as a result of lower weight and energy consumption. A study on the life cycle

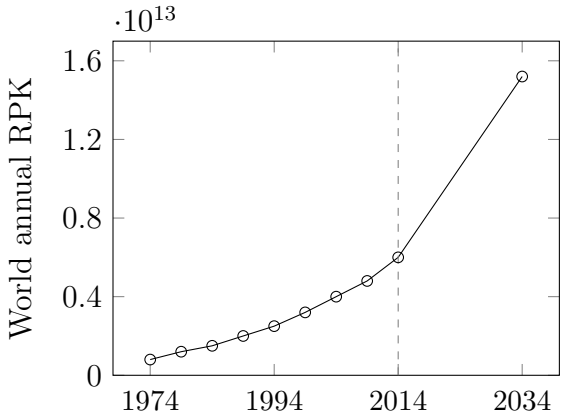

Fig. 1.1: Development and forecast of annual worldwide revenue-passenger kilometers (RPK) until 2034 [1]

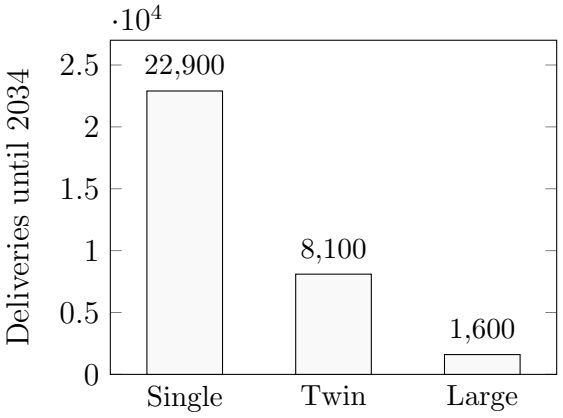

Fig. 1.2: Forecast of total sales for single-aisle, twin-aisle and very large aircrafts until 2034 [1]

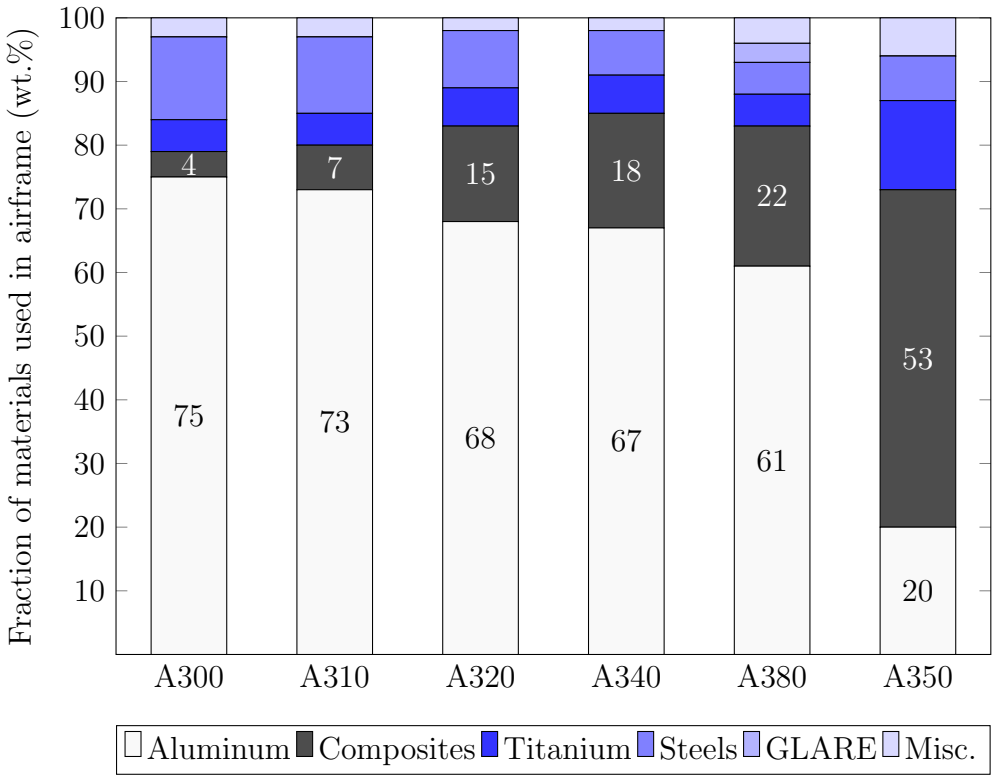

Fig. 1.3: Material mix used in Airbus planes over ∼50 years from A300 (1972) to A350 (2014) showing the reduced use of Al and the concurrently increased use of composite materials. Data kindly provided by Airbus Group Innovations.

energy consumption of several types of transport vehicles [2], however, showed that the cost savings due to weight reduction are less pronounced for short-range aircrafts. A comparable replacement of Al components by composite materials as for the Airbus A350 is therefore not expected for the prognosticated 23 000 next generation single-aisle aircrafts, specifically the successor of Airbus A320 [3]. For fuselage components, in particular, it is assumed that the weight reduction achieved by using expensive composite materials instead of Al-alloys is not profitable.

The fuselage of an aircraft is a stiffened shell containing an external skin, as well as longitudinal and transverse structural elements. The longitudinal reinforcing parts are usually called stringers, the transverse parts are referred to as the frame. A typical structural design of an aircraft fuselage is given in Fig. 1.4. Most of the primary loads due to fuselage bending, shear, torsion, and cabin pressure are carried by the stringers and the skin, while the frame supports to maintain the shape of the aircraft cross section and prevent buckling. The major portion of the fuselage bending moment is carried by the stringers wich are therefore loaded by axial forces resulting from the bending moment

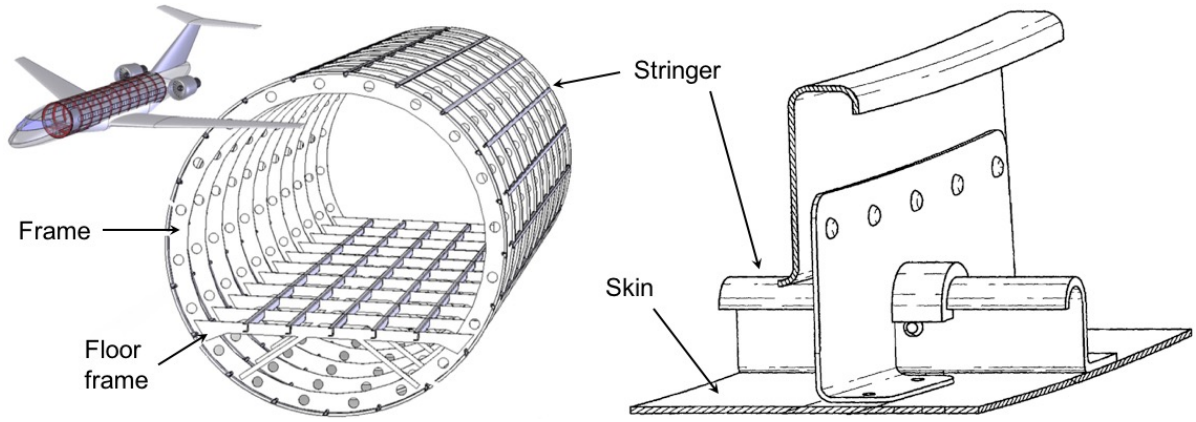

Fig. 1.4: Structural design of an aircraft fuselage. The main components are the outer skin, the frames, and stringers. The typical shape of an Al stringer is illustrated in the right image. Based on [5,6].

[4]. Therefore, main requirements for stringer materials are high strength and stiffness. The shape of a typical Al stringer is given in the right image of Fig. 1.4. The production of a metallic part of such shape requires several production steps including casting, rolling, heat treatments, welding, and forming. In addition, the in-service behavior of the part is crucial for the life cycle costs of the entire component. The in-service behavior in that context particularly refers to the corrosion behavior. Besides the requirement of sufficient strength, therefore, an Al-alloy used for stringers needs to be processable in several ways and corrosion resistant.

Currently Al-Cu-Mg alloys, for example 2024, are the dominant stringer material in Al-based airframe structures due to their high strength. On the other hand, these alloys are susceptible to corrosion and are relatively heavy compared to other alloys such as Al-Mg. In addition, Al-Cu-Mg alloys are non-weldable using fusion welding processes such as laser welding, a process considered to replace riveted structures [7]. Consequently, the currently used alloys should be replaced by novel materials that achieve similar strength levels while outperforming the Al-Cu-Mg alloys along the production and life cycle. A material that could be capable to meet these requirements is Al-Mg-Sc [3].

Al-Mg alloys modified with small amounts of Sc (or Sc and Zr) are potential candidates to replace Al-Cu-Mg alloys for airframe stringers of future single-aisle aircrafts [3,7]. It is expected [8] that alloys of this type could have the positive processing properties of Al-Mg alloys but achieve higher strength levels due to the formation of hardening Sc- and Zr-containing phases. These phases of the type Al_3(Sc,Zr) precipitate out of a supersaturated solid solution at elevated temperatures and determine to a large extent

the mechanical properties as well as the processability of the alloy. The most important effects of Al_3(Sc,Zr) are the hardening effect due to fine precipitates and their effect on preventing recrystallization in a deformed microstructure. The precipitation of Al_3(Sc,Zr) initially requires a solid solution supersaturated in Sc and Zr. As a solution heat treatment on industrial scale is practically not feasible with an Al-Mg-Sc-Zr alloy, a high degree of supersaturation and, in consequence, a pronounced precipitate hardening effect is only achievable using rapid solidification processes.

According to Røyset and Ryum [9], Sc-containing Al-alloys were first mentioned in the 1960's in the former Soviet Union. Since then, the promising materials properties have basically been known, however, the breakthrough as a structural material for the civil aircraft industry has not yet occurred. The main reason for this is quite simple: The positive properties could not compensate for the high price of Sc [10]. In addition, an efficient use of Sc was not possible using conventional methods for Al-alloy production. As the Sc-price was reduced to an acceptable yet still rather high level over the last years [11], more efficient methods for alloy production were considered and evaluated. Amongst these methods rapid solidification processes appear to be very promising. In order to optimize a rapidly solidified Al-Mg-Sc-Zr alloy and to control the mechanical properties of a final product, it is essential to understand the evolution of the microstructure and, in particular, the evolution of the strengthening Sc- and Zr-containing phases during materials production. Knowledge of this fundamental behavior is necessary, for example, to determine thermo-mechanical processing parameters and to understand the behavior of welded structures to finally set-up a suitable production process for an entire component. However, there exist no studies reporting on the fundamental behavior of rapidly solidified Al-Mg-Sc-Zr alloys produced on industrial equipment.

This work deals with the fundamental characterization of a novel Al-Mg-Sc-Zr alloy produced on industrial belt-casting equipment. The main focus is put on the kinetics of precipitation of strengthening Sc- and Zr-containing phases, and in particular on the interaction between precipitation and recrystallization in cold deformed material.

2 Literature Review

In this chapter, first the most relevant metallurgical phenomena that are investigated in this work are explained. Second, the system Al-Mg-Sc-Zr is described in detail. Finally, the properties of such alloys depending on the chemical composition and the processing of the material are discussed and the most relevant open questions are highlighted.

2.1 Strengthening mechanisms in Al-alloys

The strength of a material is defined as its resistance to plastic deformation [12]. In metals, plastic deformation is associated with the movement of dislocations through a crystal, as illustrated in Fig. 2.1. By applying a shear stress, a dislocation glides through the crystal in its slip plane until a step forms on the surface or grain boundary. The shear stress must exceed the critical resolved shear stress (CRSS) necessary to move a dislocation through the crystal. When the shear stress is released, a plastic deformation remains. Consequently, the movement of dislocations must be hindered or even inhibited by increasing CRSS in order to increase the strength of a metallic material [13,14].

In metals and alloys, strengthening is achieved by introducing barriers to the movement of dislocations. These barriers are commonly categorized in four groups, whereas each group represents one strengthening mechanism. The four mechanisms are [15]:

- Solid solution hardening
- Grain size hardening
- Precipitation hardening
- Strain (dislocation) hardening

The total strength of a material can be considered as a sum of the contributions of the strengthening mechanisms, as suggested in [16]:

$$\sigma = \sigma_0 + \sigma_{sol} + \sigma_{gs} + \sigma_{prec} + \sigma_{dis}, \tag{2.1}$$

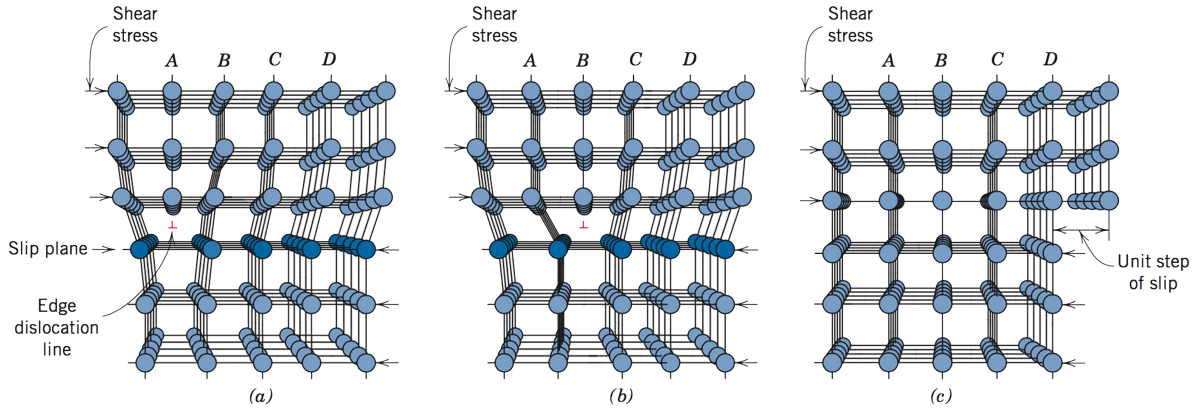

Fig. 2.1: Schematic illustration of the movement of an edge dislocation in a crystal: (a) initial position of the dislocation line, (b) movement of the dislocation for one lattice plane, (c) plastically deformed crystal [13].

with the intrinsic strength σ_0, and the strengthening contributions from solid solution σ_{sol}, grain size σ_{gs}, precipitates σ_{prec}, and dislocations σ_{dis}. The addition of the strengthening terms in Eq. 2.1 is not necessarily linear, as demonstrated by Fazeli *et al.* [17], who modeled the superposition of solid solution, precipitation, and strain hardening in an Al-Mg-Sc alloy using the expression:

$$\sigma = \sigma_{sol} + (\sigma_{prec}^{n} + \sigma_{dis}^{n})^{1/n}. \tag{2.2}$$

They suggested values of the exponent n ranging from 1 to 2. Marquis *et al.* [18] calculated the superposition of solid solution and precipitate hardening using:

$$\sigma = (\sigma_{sol}^{n} + \sigma_{prec}^{n})^{1/n}, \tag{2.3}$$

where the best correspondence to experimental data of an Al-Mg-Sc alloy was found at an exponent of $n = 1$. A linear strength superposition model was also used to calculate the yield strength due to σ_{sol} and σ_{gs} in Al-Mg alloys [19] or to simulate the strengthening contributions in steel containing Cu-precipitates [20]. In summary, a linear superposition of the strengthening terms (Eq. 2.1) is reasonable but represents the upper limit of the total strength calculated from individual contributions. The connection of the strength σ of a polycrystalline material and CRSS τ_{cr} is given by the Taylor factor M (Eq. 2.4). The Taylor factor considers randomly oriented grains and equals $M = 3.06$ for Al [21].

$$\sigma = M \cdot \tau_{cr}. \tag{2.4}$$

The four strengthening mechanisms in principle apply to all metallic materials including Al-alloys, however, their effect is more or less pronounced for different types of metals. In the following sections, the single mechnisms are explained in different levels of detail depending on the respective importance for Al-alloys in general, and Al-Mg-Sc-Zr alloys in particular.

2.1.1 Solid solution hardening

A solid solution of atoms A and atoms B generally has a higher strength than pure metal A. In other words, alloys are almost always stronger than high-purity metals. The reason with respect to solid solution strengthening is that different atoms have different sizes, leading to lattice strains around the solute alloying elements, as illustrated in Fig. 2.2. A solute atom that is smaller (Fig. 2.2 a) than the host atom produces tensile strain and a larger solute atom (Fig. 2.2 b) produces compression strain. Either way, the solute atoms are surrounded by a stress field that has to be overcome by the dislocation in order to pass by, thus hindering the dislocation movement and increasing the strength of the alloy. Moreover, solute atoms tend to diffuse to dislocations, as shown in the respective right images in Fig. 2.2, leading to dislocation locking, i.e. a significant increase in stress necessary to start dislocation movement. The strength increment introduced by solid solution hardening is often described in a general form by [13,16]:

$$\sigma_{sol} = k_1\sqrt{C}, \tag{2.5}$$

with the constant k_1 representing the specific strengthening effect of atom B in material A accounting for the shear modulus and atomic misfit. The concentration of the solute element is considered by C [22].

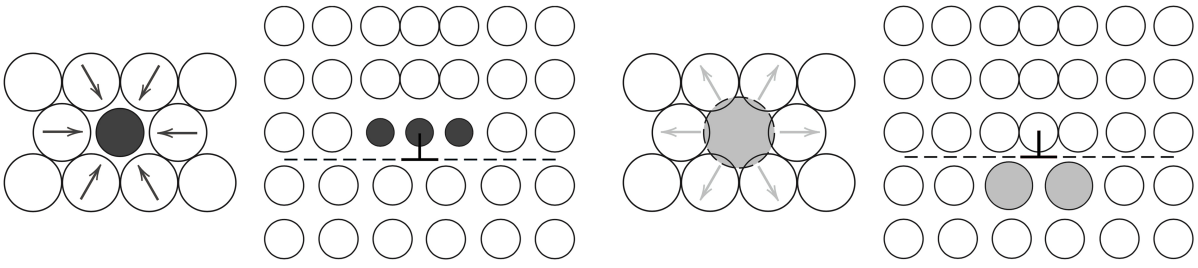

(a) Smaller alloying element (b) Larger alloying element

Fig. 2.2: Lattice strains due to solid solution strengthening and possible positions of alloying elements with respect to edge dislocations [13]

Magnesium is one of the most common alloying elements to achieve solid solution strenghtening in Al-alloys. Fig. 2.3 shows the influence of the Mg-concentration in Al on the tensile properties of fully recrystallized alloys. Both the yield and ultimate tensile strengths increase with increasing Mg-content of up to 10 wt.% [19].

In contrast to pure Al showing a smooth stress-strain curve in Fig. 2.3, the curves for the different Al-Mg alloys reveal serrated shapes. This serrated flow behavior referred to as Portevin-Le Chatelier (PLC) effect is typical for Al-Mg alloys. According to several investigations [23–26], the most prominent and generally accepted explanation of the PLC effect is based on dynamic strain aging (DSA) resulting from dynamic solute-dislocation interactions. The DSA effect is described as follows: A dislocation enriched in solute atoms (Fig. 2.2) requires a higher stress level to start dislocation movement than to continue this movement. In other words, once the dislocation has overcome the starting barrier it can move at a lower stress level. When the dislocation is temporary trapped at local obstacles such as dislocations or precipitates, the solute atoms diffuse to and pin the dislocation, thus increasing the dislocation activation barrier again [25,27]. The PLC effect is less pronounced at higher strain rates and lower temperatures (below room temperature) in Al-Mg alloys as a result of the reduced Mg diffusion [28,29].

In commercial Al-Mg alloys, usually a maximum of 6 wt.% Mg is added due to limited solubility and corrosion resistance [15,30].

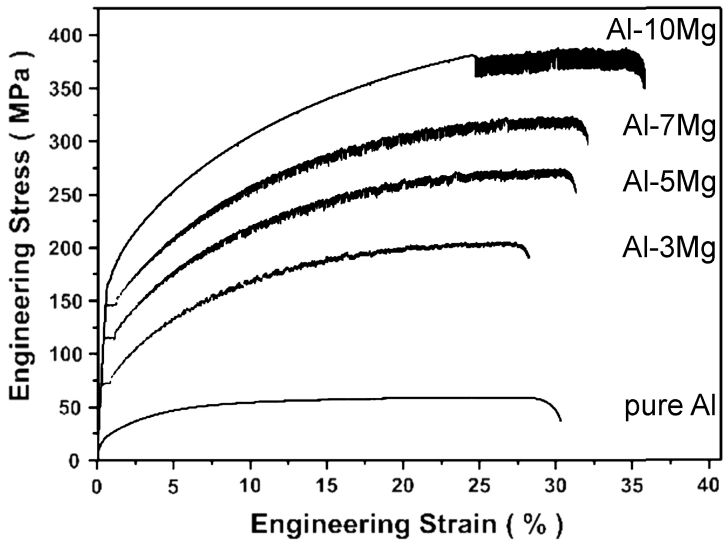

Fig. 2.3: Stress-strain curves of fully recrystallized Al-Mg alloys showing an increase in tensile strength with increasing Mg concentration [19].

2.1.2 Grain size hardening

A dislocation that reaches a grain boundary cannot continue its slip motion because of the difference in orientation between the two neighboring grains (Fig. 2.4 a). The grain boundaries serve as obstacles to the movement of dislocations, which pile up near the boundaries. With decreasing grain size, the number of grain boundaries increases and less distance can be travelled by a moving dislocation [16]. The strengthening effect due to grain size can be expressed by the Hall-Petch relation:

$$\sigma_{gs} = \frac{k_2}{\sqrt{D}}, \tag{2.6}$$

where D is the grain size and k_2 is a constant that is affected by alloy content, grain size uniformity and shape, and crystallographic texture. The coefficent k_2 equals 0.065 $\mathrm{MPam}^{-\frac{1}{2}}$ for pure Al and $0.1-0.2\,\mathrm{MPam}^{-\frac{1}{2}}$ for many Al-alloys [16]. Among the Al-alloys, higher k_2-values of up to $0.3\,\mathrm{MPam}^{-\frac{1}{2}}$ are only reached in Al-Mg-alloys [31]. Although this level is only slightly below that of Mg-alloy AZ31 (up to $0.4\,\mathrm{MPam}^{-\frac{1}{2}}$) [32], it is considerably lower compared to several steel types ($0.5-1.0\,\mathrm{MPam}^{-\frac{1}{2}}$) [33]. In consequence of comparably low k_2 values, grain size hardening does not provide significant strengthening in a large variety of Al-alloys, including Al-Mg.

It was shown for Al-Mg alloys [19] that the presence of Mg decreased the grain size in deformed and recrystallized materials, as shown in Fig. 2.4 (b). However, despite the significant grain size reduction from roughly 215 μm to 21 μm, the yield strength incre-

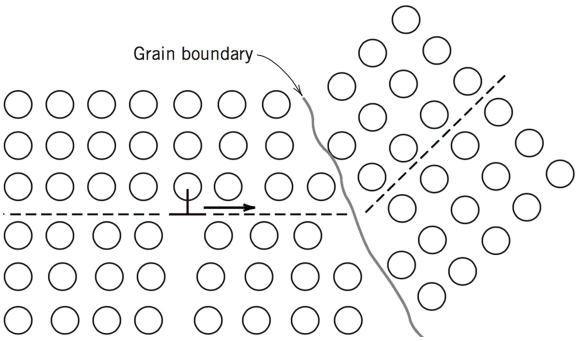

(a) Dislocation movement is stopped at a high angle grain boundary [13]

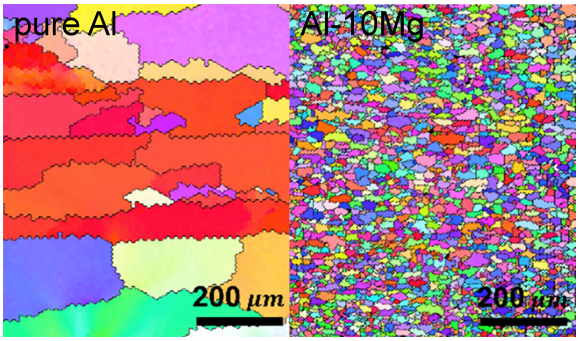

(b) Micrographs showing large grains in pure Al and finer grains in Al-Mg10 [19]

Fig. 2.4: Dislocation movements are stopped at high angle grain boundaries (a) leading to an increased strength in materials revealing a large amount of grain boundaries. In consequence, fine-grained materials are stronger than coarse-grained materials (b).

ment due the reduced grain size σ_{gs} equalled only around 35 MPa. This strenghtening increment was considerably smaller than that of solid solution hardening due to the addition of 10 wt.% Mg. For the same Al-Mg10 alloy, the strength increment σ_{sol} equalled roughly 110 MPa.

It should be noted that the Hall-Petch relation given in Eq. 2.6 is only valid for grain sizes in the micrometer range and not for ultra-fine grained nanostructures, e.g. [34].

2.1.3 Precipitation hardening

Precipitation is a phenomenon where particles of a new phase form out of a supersaturated solid solution [35]. If such particles are present in a material, they interfere with the movement of dislocations, and therefore, increase the strength. The basic requirement for precipitation-hardening alloy systems is that the solid solubility limit of the main precipitate forming element decreases with decreasing temperature. This facilitates the typical precipitate strengthening process consisting of solution heat treatment, rapid quenching, and ageing.

The heat treatment process as well as its connection to a theoretically relevant phase diagram are illustrated in Fig. 2.5. First, a solution treatment at T_S is carried out to dissolve the large β phases located at the grain boundaries and to generate a homogenous solid solution α. After quenching to T_Q, e.g. to room temperature, only α grains supersaturated in atoms B are present while the formation of β phases is suppressed. The ageing step occurs at the temperature T_A to form β phase precipitates. The ageing temperature and time strongly influence the strengthening effect by affecting the nature of the precipiates, i.e. the size, structure, amount, and distribution [36,37].

The nature of the precipitates determines the interaction mechanism between dislocations and precipitates. The possible dislocation-precipitate interaction mechanisms are particle shearing and Orowan looping. Fig. 2.6 shows that, for a given precipitate volume fraction, particle shearing is the dominant mechanism at small precipitate sizes, whereas Orowan looping dominates at larger precipitate radii. The transition from one mechanism to the other occurs at the transition radius r_t, where the maximum strength is reached [36]. The dislocation-precipitate interaction mechanisms are explained in the following sections.

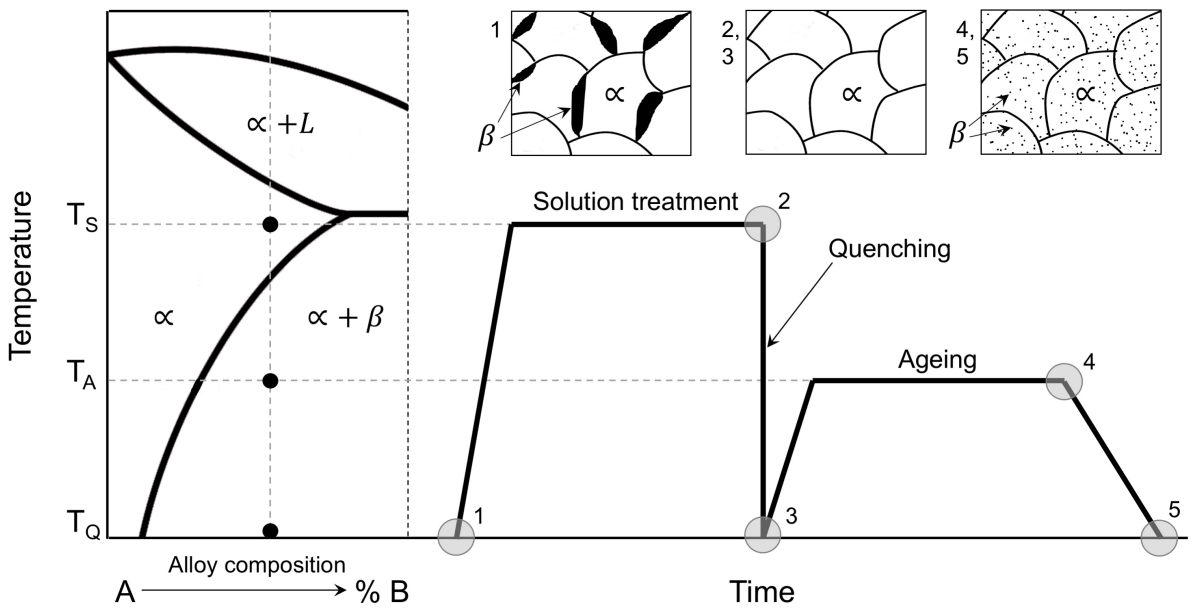

Fig. 2.5: Illustration of the precipitation hardening process using a schematic phase diagram (left) and a corresponding heat treatment (right): Solution treatment (1,2) to dissolve β phases located at grain boundaries, followed by quenching (3) to achieve a supersaturated solid solution. Ageing in $\alpha + \beta$ phase field (4,5) to form small β phase precipitates inside the α grains. Based on [13,14,37]

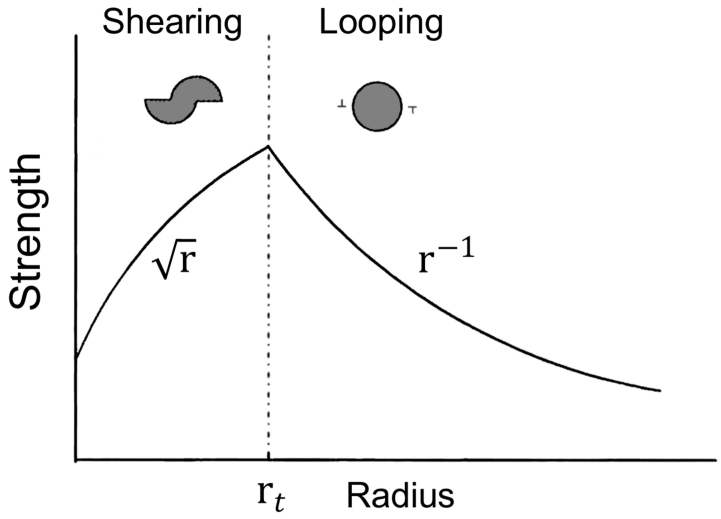

Fig. 2.6: Correlation of the strengthening increment due to precipitation hardening and the precipitate radius for a given precipitate volume fraction. The precipitate-dislocation interaction mechanism changes from particle shearing to Orowan looping at the transition radius r_t [16].

2.1.3.1 Shearing mechanism

Coherent precipitates with a size smaller than the critical radius r_t are sheared by a moving dislocation. The actual dislocation-precipitate interaction mechanism varies from one alloy to another, whereas it is generally accepted, that one or often more of the following mechanisms apply [21]:

- Chemical strengthening
- Stacking-fault strengthening
- Modulus strengthening
- Coherency strengthening
- Order strengthening

It was proposed by Seidman, Marquis *et al.* [18,38] that the relevant contributions in Al-(Mg)-Sc alloys are modulus, coherency, and order strengthening. Furthermore, they showed that the transition radius r_t (Fig. 2.6) was determined by the combination of these three shearing mechanisms and the Orowan strength (looping). In the present work it is intended to estimate r_t for a novel Al-Mg-Sc-Zr alloy. Accordingly, the relevant mechanisms are explained more in detail including mathematical formulations, while the principles behind chemical and stacking-fault strengthening are only described briefly. For details on these mechanisms the reader is referred to [21].

2.1.3.1.1 Chemical strengthening

Chemical strengthening results from the production of additional particle-matrix interfacial area due to the shearing process. The magnitude of the strengthening increment depends on the interfacial energy between precipitate and matrix. In [18,38] the neglect of chemical strengthening for Al-Sc alloys is not specifically justified, however, according to [20,21], the chemical strengthening effect is usually small compared to the other shearing mechanisms.

2.1.3.1.2 Stacking-fault strengthening

The motion of dislocations is impeded, when the stacking-fault energies γ_{sf} of the precipitate and matrix differ. The stacking-fault energy describes the extent to which dislocations dissociate and split up into partial dislocations. When γ_{sf} is different in precipitate and matrix, the separation of the partial dislocations varies depending on the phase in

which the dislocation resides. The strengthening increment depends on the magnitude of the difference $\Delta\gamma_{sf}$ [21]. For Al-Sc alloys, this mechanism was neglected without explanation, thus it can be assumed that the influence is comparably small [17,18,38].

2.1.3.1.3 Modulus strengthening

Modulus or modulus mismatch strengthening results from the difference in shear modulus between matrix and precipitate. There exist several mathematical formulations of this phenomenon in literature, all of which having very similar dependencies, e.g. [20,21,38]. For Al-(Mg)-Sc alloys, the following expression was used [18,38]:

$$\sigma_m = 0.0055M(\Delta G)^{3/2}\left(\frac{2f_V}{Gb^2}\right)^{1/2} b\left(\frac{r}{b}\right)^{\frac{3m}{2}-1}, \tag{2.7}$$

where M is the Taylor factor, ΔG is the shear modulus mismatch between precipitate and matrix, f_V is the precipitate volume fraction, r is the mean precipitate radius, G is the shear modulus of Al, b is the Burgers vector, and m is a constant.

2.1.3.1.4 Coherency strengthening

Coherent precipitates are surrounded by an elastic stress field as a result of the lattice misfit between precipitate phase and matrix phase. Coherency strengthening results from the interaction of the precipitate with this stress field. According to [18,38], the corresponding strengthening effect in Al-(Mg)-Sc alloys can be described by:

$$\sigma_c = M\alpha_\varepsilon(G\varepsilon)^{3/2}\left(\frac{rf_V}{0.18Gb^2}\right)^{1/2}. \tag{2.8}$$

Here, α_ε is a constant and ε is the linear misfit strain calculated as [18,38]:

$$\varepsilon \approx \frac{2}{3}\frac{|a_p - a_m|}{a_m}, \tag{2.9}$$

with the lattice constants of precipitate a_p and matrix a_m, respectively.

2.1.3.1.5 Order strengthening

Order strengthening occurs when a dislocation shears a coherent ordered precipitate and creates an antiphase boundary. In Al-Sc alloys, the strengthening Al_3Sc precipitates are

of ordered nature, as explained in detail in 2.3.4, hence this mechanism applies. The resulting strengthening effect is proportional to the antiphase boundary energy γ_{apb} and is expressed by [18,21]:

$$\sigma_o = M \frac{\gamma_{apb}}{2b} \left(\frac{3\pi^2 f_V r}{16 G b^2} \right)^{1/2}. \tag{2.10}$$

2.1.3.1.6 General formulation of the shear strength

When considering Eqs. 2.7, 2.8, and 2.10, the mathematical formulation of the strengthening effect of shearable precipitates is summarized by [16,39]:

$$\sigma_{shear} = C_1 \, f_V^{1/a} \, r^{1/b}, \tag{2.11}$$

with a constant C_1, the precipitate volume fraction f_V, the precipitate radius r, and the factors a and b. According to [16], the factors a and b are approximately equal to a value of 2, setting the basis for the square-root shearing law illustrated in Fig. 2.6:

$$\sigma_{shear} = C_1 \sqrt{f_V \cdot r}. \tag{2.12}$$

The strengthening effect due to shearing of coherent precipitates increases with increasing volume fraction and precipitate radius but, for a given volume fraction, is limited by the transition radius r_t.

2.1.3.2 Orowan mechanism

Unlike small coherent particles, that are sheared by a moving dislocation, incoherent precipitates or any precipitates with radii larger than r_t interact with dislocations in a way referred to as Orowan looping. A schematic illustration of the Orowan mechanism is given in Fig. 2.7. A dislocation bows around precipitates until impingement before it can move on, leaving a dislocation loop around the particles. The passing-by requires higher stress than dislocation glide in a precipitate-free grain, thus increasing the strength of the material. The basic formulation of the Orowan strength is given by [16,40]:

$$\sigma_{or} = a \, G \, b \frac{1}{\lambda}, \tag{2.13}$$

where G and b have their common meanings, a is a constant, and λ is the average inter-particle spacing. According to Eq. 2.13, a high strengthening effect is achievable

with a small spacing between the precipitates. This correlation is rather easy to imagine when considering Fig. 2.7. The inter-particle spacing λ relates to the number density of precipitates in the slip plane n_s by [21]:

$$\lambda = n_s^{-1/2}. \tag{2.14}$$

Since:

$$\sqrt{n_s} \propto \frac{\sqrt{f_V}}{r}, \tag{2.15}$$

a basic formulation of the Orowan strength as a function of the precipitate volume fraction f_V and the radius r is found by [16]:

$$\sigma_{or} = \tilde{a}\, G\, b \frac{\sqrt{f_V}}{r}, \tag{2.16}$$

with another constant $\tilde{a}$. For a given precipitate volume fraction f_V, therefore, high strength translates into a large number of particles with a small radius r, as illustrated by the r^{-1} slope in Fig. 2.7 [16,40].

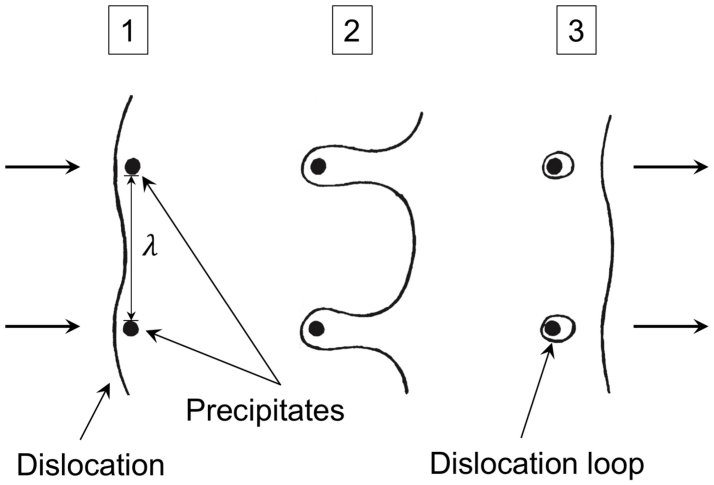

Fig. 2.7: Interaction between a dislocation and precipitates with the inter-particle spacing λ in case of Orowan mechanism. The dislocation bows around precipitates (1-2) until impingement (2-3) before it can move on, leaving a dislocation loop around the particles (3) [40].

Seidman, Marquis *et al.* [18,38] calculated the Orowan strength of Al-(Mg)-Sc alloys based on a formulation of Ardell [21]:

$$\sigma_{or} = M\frac{0.4Gb}{\pi\sqrt{1-\nu}}\frac{\ln(\frac{2r}{b})}{\lambda}. \tag{2.17}$$

Here, ν is the matrix Poisson's ratio and the other factors have their common meanings. The corresponding inter-particle spacing was calculated using Eq. 2.18 [38]:

$$\lambda = \left[\left(\frac{3\pi}{4f_v}\right)^{1/2} - 1.64\right]r. \tag{2.18}$$

2.1.3.3 Evolution of precipitates

The strengthening effect of precipitates depends on their size, structure, amount, and distribution, as discussed above. These characteristics, and thus the strength of an age hardened alloy, strongly depend on the evolution of the strengthening particles as a function of ageing temperature and time. The evolution of a population of precipitates is commonly categorized in three stages that occur during the ageing treatment (Fig. 2.5): nucleation, growth, and coarsening [35].

2.1.3.3.1 Nucleation

Nucleation refers to the initial formation of precipitates. The nucleation process is of stochastic nature and describes the probability of the creation of nuclei with supercritical size, i.e. thermodynamically stable nuclei. In that context, nuclei with a radius larger than the critical size r^* will grow further, while smaller ones dissolve. The steady state nucleation rate is expressed by [35]:

$$J_{ss} = Z\beta^* N_c \exp\left(-\frac{\Delta G^*}{kT}\right). \tag{2.19}$$

Here, Z is the dimensionless Zeldovich factor denoting the probability that a nucleus with critical size grows further rather than dissolves. β^* represents the atomic attachment rate depending on the diffusion coefficient and mole fraction of solute atoms. N_c is the number of potential nucleation sites, ΔG^* is the critical nucleation energy, k is the Boltzmann constant, and T is the temperature. The most essential factor in Eq. 2.19 is the critical nucleation energy that has to be overcome in order to form stable nuclei with a radius

r^*. The mathematical formulation based on [35] is calculated for spherical nuclei by:

$$\Delta G^* = \frac{16\pi}{3}\frac{\gamma^3}{G_{vol}^2}, \tag{2.20}$$

with the interfacial energy between precipitate and matrix γ and the free energy change due to nucleus formation G_{vol}. The free energy change represents the driving force for precipitation and depends on the degree of supersaturation of the precipitate forming element in the matrix as well as the elastic strain energy per volume of precipitate. More specific, G_{vol} is large in case of a high degree of supersaturation and low elastic strain caused by the formation of precipitates. Summarizing Eqs. 2.19 and 2.20, the nucleation rate increases with increasing temperature, increasing driving force, and decreasing interfacial energy. In general, the interfacial energy γ is low for coherent and comparably high for incoherent precipitates, and may depend on the precipitate radius and ageing temperature [41,42]. Nucleation events may occur homogeneously at random lattice positions in the matrix or heterogeneously at positions such as dislocations or grain boundaries [35,43].

2.1.3.3.2 Precipitate growth

The growth process is described by a diffusional flux of the precipitate forming elements present in supersaturated solid solution towards the already formed nuclei. The total precipitate volume increases by reducing the degree of supersaturation in the matrix. Precipitate growth is mathematically expressed by [35]:

$$r(t) = \sqrt{r_0^2 + S^2 D t}, \tag{2.21}$$

with the precipitate radius r, the initial radius r_0, the supersaturation parameter S, the diffusion constant D, and the time t. The supersaturation parameter is given by:

$$S = \frac{C_0 - C_e}{C_p - C_e}. \tag{2.22}$$

C_0 is the concentration in the matrix, C_e is the equilibrium concentration in the matrix, and C_p is the concentration in the precipitates. The diffusion constant D depends on the ageing temperature T by (e.g. [13]):

$$D = D_0 \exp\left(-\frac{Q}{RT}\right), \tag{2.23}$$

with a temperature-independent preexponent D_0, the activation energy Q, and the gas constant R. Accordingly, the growth rate (Eq. 2.21) increases with increasing annealing temperature and supersaturation.

2.1.3.3.3 Coarsening

The final stage in the evolution of a precipitate population is coarsening, also termed Ostwald ripening. This stage usually occurs when a phase equilibrium is already reached, i.e. the degree of supersaturation is reduced to a value of 0. During the coarsening process, larger particles continue to grow at the expense of smaller ones, reducing the total number of particles at a constant precipitate volume fraction. The driving force for precipitate coarsening is the minimization of the total interfacial area between matrix and precipitates. By minimizing the interfacial area, the energy of a constant volume of precipitates is reduced. Coarsening is faster at higher annealing temperature [35,43].

2.1.3.3.4 Influence of ageing parameters on the age hardening effect

The correlation between ageing temperature, time, and achievable strength is exemplarily illustrated in the heat treatment curves of an Al-Mg-Si alloy in Fig. 2.8. The typical shape of an age hardening curve, for example the gray one at 204°C, can be described by a rather flat incubation time (0.1 h) followed by a steep increment to the maximum strength ($\sim$ 1 h) and a subsequent strength reduction. When comparing the individual age hardening curves, a strong dependency on the ageing temperature is observed [15].

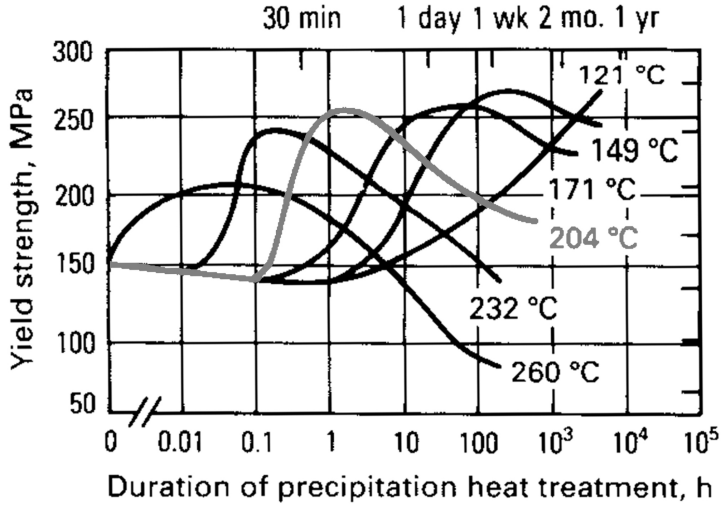

Fig. 2.8: Precipitation heat treatment curves for 6061 Al-alloy showing the influence of the annealing temperature on the yield strength [15].

A lower temperature leads to a prolonged incubation time resulting from a reduced nucleation rate (Eq. 2.19). In addition, the peak strength is reached after longer ageing times due to slower precipitate growth (Eq. 2.21). The nucleation and growth stages may partially overlap depending on the complex, alloy-dependent interplay between the two processes. If the nucleation rate is rather constant along the growth stage, both nucleation and growth occur simultaneously until peak ageing is reached. If the nucleation rate is reduced to 0 as soon as precipitate growth is initiated, the nucleation and growth stages are completely separated. The latter case is often referred to as nucleation site saturation [35,43].

The maximum precipitate hardening effect depends on the ageing temperature, as shown by the different peak strengths in Fig. 2.8. The highest strength is achieved for the sample annealed at the lowest investigated temperature. High strength translates into a large number of precipitates, as derived in 2.1.3.2. Indeed, at lower temperature, a larger number of smaller precipitates is formed. However, the process requires longer ageing times due to reduced nucleation and growth rates [35,41,44]. It should be mentioned, that the ageing temperatures may vary strongly from one alloy to the other and a minimum temperature may be required to form the strengthening phases.

The loss in strength after reaching the peak age condition results from precipitate coarsening, where the precipitate number density is continuously reduced. Again, this process is more pronounced the higher the ageing temperature [15,35].

2.1.3.4 Johnson-Mehl-Avrami-Kolmogorov notation

The precipitation kinetics is often described by the Johnson-Mehl-Avrami-Kolmogorov (JMAK) notation. The JMAK formulation is a phenomenological model to quantitatively describe nucleation and growth processes [35,45]. The coarsening stage can not be modeled with this approach, however, for technical applications coarsening is avoided.

The JMAK equation considers the volumetric formation of new particles from a solid solution over time and is based on two major assumptions. First, the new phase nucleates or grows regardless of whether it involves regions of the parent phase or already transformed volume. All volume that is created by nucleation or growth is denoted as *extended volume*. Second, the probability that nucleation events occur in untransformed regions is related to the ratio between actual and extended volume [35]. During a time interval dt, the fraction of extended volume X_{ext} increases by an amount dX_{ext}. With the fraction of transformed volume X_{tf} it follows that the untransformed fraction equals

$1 - X_{tf}$. The increase of transformed volume fraction in the time interval dt reads [39]:

$$dX_{tf} = (1 - X_{tf})\, dX_{ext}. \tag{2.24}$$

After separation of variables and integration one obtains:

$$X_{ext} = -\ln(1 - X_{tf}), \tag{2.25}$$

or mathematically transformed:

$$X_{tf} = 1 - exp(-X_{ext}). \tag{2.26}$$

In the most simplified way, the fraction of extended volume can be written as [39]:

$$X_{ext} = \frac{\pi}{3}\, \dot{N}\, \dot{G}^3\, t^4, \tag{2.27}$$

with the nucleation rate $\dot{N}$, the growth rate $\dot{G}$, and the time t. Since Eq. 2.27 is based on several assumptions including a random distribution of spherical nuclei as well as constant nucleation and growth rates, the JMAK equation is often found in its more general form:

$$X_{tf} = 1 - exp(-k\, t^n). \tag{2.28}$$

Here, the value k is the JMAK constant and n represents the JMAK exponent. Fig. 2.9 shows the common shapes of several JMAK functions qualitatively reproducing the nucleation and growth stages of the ageing curves shown in Fig. 2.8. Since both n and k do not represent physical quantities, their interpretation is sometimes ambiguous. The exponent n is closely related to the transformation mechanism and can be viewed as a measure for the relative importance of nucleation and growth mechanisms. The significance of n is illustrated in Fig. 2.9 (a). There, at constant k, the shape of the functions changes considerably when varying n between 1 and 4. Values between 1 and 2 are often observed when nucleation rates are rather low and the transformation progress is controlled by growth. Higher exponents of 3 or 4 indicate higher nucleation rates and may occur in highly supersaturated systems. The coefficient k contains the nucleation rate $\dot{N}$ and the growth rate $\dot{G}$ and is, therefore, a function of temperature and thermokinetic boundary conditions of the transformation. The variation of k at constant n is given in Fig. 2.9 (b). An increasing coefficient k shifts the curves to shorter times, while the

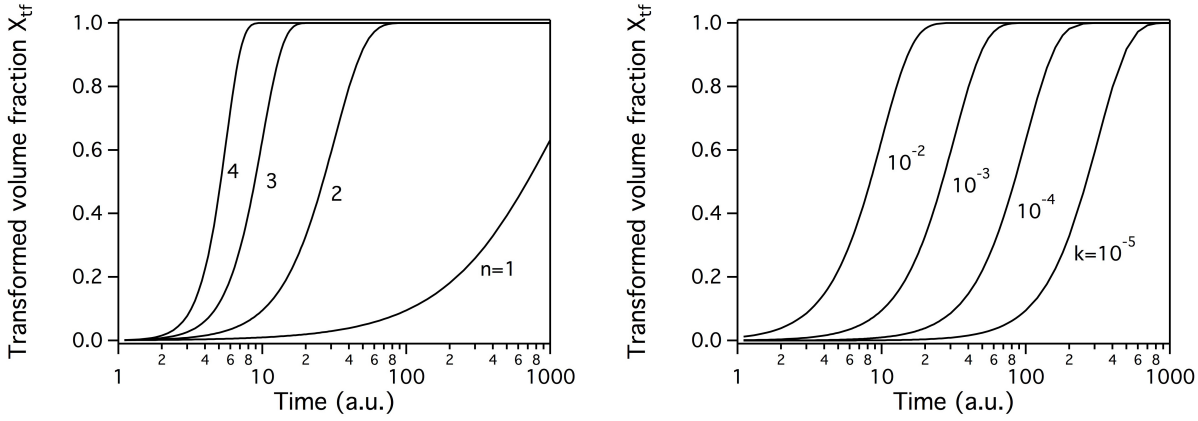

(a) Different exponents n, with $k = 0.001$

(b) Different coefficients k, with $n = 2$

Fig. 2.9: JMAK functions showing the influence of the parameters n and k. Based on [35].

general shape of the curves is essentially unaffected. Since the coefficient k includes the cube of the growth rate, high values are typical for transformations with large growth rates [35].

The JMAK equation was similarly developed to describe the evolution of recrystallization, with $\dot{N}$ and $\dot{G}$ representing the nucleation and growth rates of recrystallized grains. For more detailed insight on the interpretation of JMAK parameters as well as the derivation of the JMAK equation itself, the reader is referred to [35,39,45].

2.1.3.5 Precipitation hardening of Al-alloys

Precipitation hardening is the most significant strengthening mechanism for a large variety of Al-alloys [46]. Considerable strengthening was achieved for example in Al-Cu-(Mg) [47], Al-Mg-Si [48–50], Al-Zn-Mg [51,52], or Al-(Cu)-Li [53] alloys. On the other hand, the strength of binary Al-Mg alloys [19] is not increased by applying the precipitation hardening process shown in Fig. 2.5, despite the temperature dependent solubility of Mg in Al. Although precipitates of the type Al_3Mg_2 form during ageing, these incoherent particles are located at grain boundaries and hence do not affect the dislocation movement [37]. If the strength of Al-Mg alloys should be increased by precipitation hardening, the addition of further elements such as scandium is required [54]. The precipitation hardening behavior of Al-Mg-Sc alloys is described in detail in section 2.3.

2.1.4 Strain hardening

Strain hardening, or work hardening, describes a phenomenon whereby a metallic material becomes stronger as it is plastically deformed. This behavior is easily observable in conventional stress-strain curves, for example in Fig. 2.3. It is generally accepted, that the flow curve at temperatures below $0.3 - 0.4\,T_m$ (Fig. 2.10) is divided into 4 stages. Fig. 2.10 (a) shows a schematic flow curve, while Fig. 2.10 (b) shows the work hardening rate $\Theta = \frac{\partial \tau}{\partial \varepsilon}$ as a function of the shear stress. The classification into stages corresponds to the curves for T_1 [55–57]:

- Stage I, also called easy glide, corresponds to free movement of dislocations in monocrystals. This stage is not seen in polycrystals (Fig. 2.10).
- Stage II begins at the onset of deformation in fcc polycrystals and is characterized by an approximately linear increase in shear stress and a constant strain hardening rate. The slope is insensitive to temperature and strain rate. Due to dislocation movement and interaction with obstacles, additional dislocations are generated by a mechanism called Frank-Read source [37]. The more dislocations are present, the more likely they interfere with each other and the stronger the material becomes.
- Stage III exhibits a decreasing slope and is highly sensitive to temperature and strain rate. The presence of stage III limits the extent of stage II by rearranging dislocations in cells and finally subgrains. The occurrence of stage III strongly depends on the stacking fault energy γ_{sf} of the material. In alloys with very high γ_{sf}, stage III may be so pronounced that stage II is not observed at all [57].

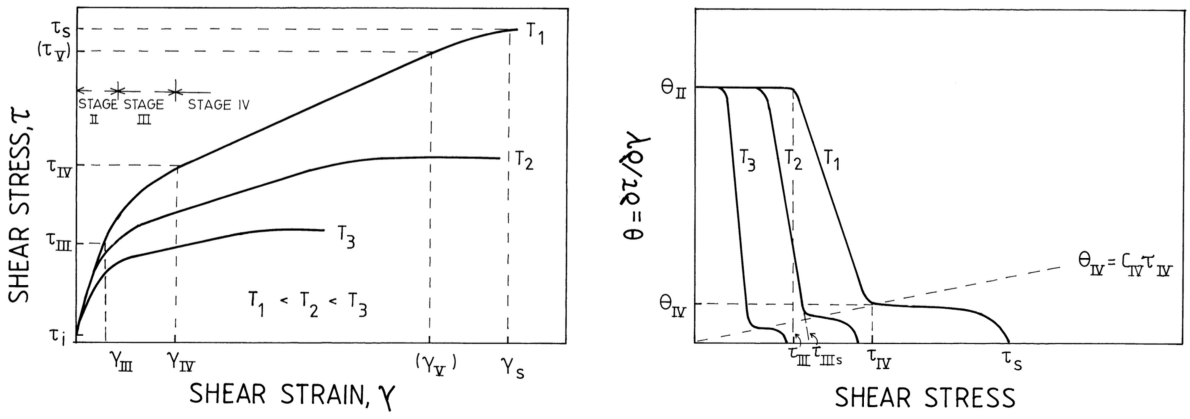

(a) Schematic flow curves

(b) Strain hardening vs. flow stress curves

Fig. 2.10: Illustration of the work hardening stages for fcc polycrystals in terms of stress-strain curves (a) and work hardening rate Θ vs. flow stress curves (b) [55].

- Stage IV shows a rather linear increase in shear stress at a much flatter slope compared to stage II. Stage IV occurs at large strains and finally ends up in saturation, where the storage of dislocations is balanced out by their rearrangement in subgrains. The stage of saturation is sometimes referred to as stage V [55].

In summary, the strain hardening effect of an alloy depends on the number of dislocations that are generated and preserved in the microstructure during plastic deformation. The strengthening effect due to dislocations can be expressed by [39]:

$$\sigma_{dis} = \alpha_1 G\, b \sqrt{\rho}, \tag{2.29}$$

where α_1 is a constant, G the shear modulus, b the Burgers vector, and ρ the dislocation density. Recrystallized aluminum at room temperature, with $G = 26\,\text{GPa}$, $b = 0.286\,\text{nm}$, and $\alpha_1 = 0.3$, has a dislocation density ρ of around $10^{10}\,\text{m}^{-2}$ which leads to a strength contribution of 0.2 MPa. For $\rho = 10^{15}\text{m}^{-2}$, as in heavily cold worked alloys, the strengthening contribution from dislocations σ_{dis} increases considerably to around 70 MPa [58]. The work hardening behavior in Al is significantly influenced by alloying elements, depending on whether these elements are present in solid solution or form second phase precipitates.

2.1.4.1 Influence of solute atoms

If solute atoms are present, work hardening is generally prolonged due to interactions of alloying elements and dislocations. Solute atoms tend to confine dislocations to slip planes which reduces the capability to climb or cross-slip, thus increases the impact of work hardening [58].

It was demonstrated [19,24], that the presence of Mg significantly affects the work hardening behavior of Al by extending stage II and retarding stage III (Fig. 2.10), thus increasing the strain hardening increment. High-purity Al has a high stacking-fault energy γ_{sf} allowing dislocations to climb and cross-slip even at room temperature. In consequence, stage II is almost entirely suppressed and dislocations are arranged in cell walls leading to a low dislocation density within the cells and low strength (Eq. 2.29). According to several authors [19,59,60], γ_{sf} is reduced linearly with increasing Mg content. For Al-alloys with Mg contents greater than 3 wt.% [19], dislocations were arranged in tangles rather than cells as a result of reduced capability to climb or cross-slip due to reduced γ_{sf}. The strain hardening increment increased with increasing Mg concentration.

2.1.4.2 Influence of second phase particles

The influence of second phase particles on the work hardening behavior strongly depends on the nature, volume fraction, size, and spacing of the preciptitates. In case of shearable particles, the work hardening rate is rather low. This is due to the fact that the dislocations, once they have cut through one precipitate, can cut through entire fields of particles at roughly the same stress level. In case of non-shearable precipitates, on the other hand, considerable work hardening is observed due to a significantly increasing dislocation density in the process of Orowan looping [58,61].

2.2 Softening of a deformed microstructure

Part of the work expended to plastically deform a metal or alloy remains as stored energy in the form of point defects and dislocations. This stored energy is progressively released upon annealing due to restoration processes occurring at elevated temperature, leading to softening of the material. Depending on several aspects such as the material type, degree of plastic deformation, and annealing temperature, recovery or recrystallization may be the dominant softening mechanism [62]. The softening processes of recovery or recrystallization may occur during deformation at elevated temperature. In this case, the phenomena are called dynamic recovery or dynamic recrystallization. In this section, however, the focus is put on static phenomena, i.e. softening occurs upon annealing after cold deformation. For further reading on dynamic restoration processes the reader is referred to [39] or [58].

2.2.1 Recovery

Recovery refers to changes in the microstructure and properties of a deformed material that occur during annealing prior to recrystallization, both in terms of temperature and temporal sequence. The two major mechanisms are the recovery of excess point defects and dislocation recovery. The recovery of point defects has only marginal influence on the mechanical properties of a material and is often neglected. The recovery of dislocations, on the other hand, significantly affects the strength of a material and is thus commonly considered in order to describe the recovery kinetics [39,62].

The process of dislocation recovery consists of several stages which are schematically shown in Fig. 2.11. The dislocation tangles present after cold deformation (a) form cell walls and annihilate within the formed cells. These two main submechanisms of recovery, illustrated in Fig. 2.11 (b) and (c), are achieved by glide, climb and cross-

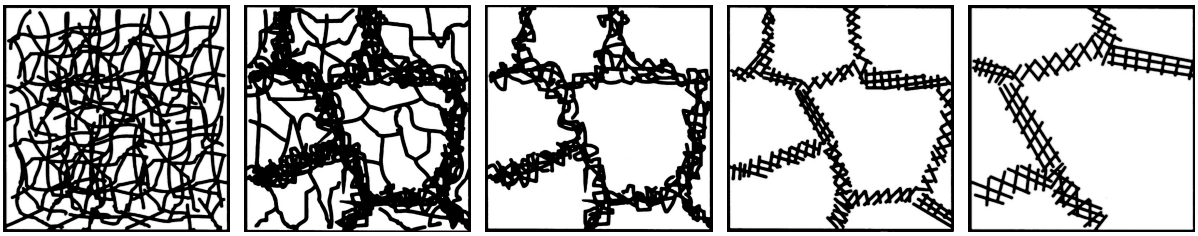

(a) Tangles (b) Cell formation (c) Annihilation (d) Subgrains (e) Growth

Fig. 2.11: Stages of recovery: Dislocation tangles form into cells or annihilate within the cells (a to c); Subgrains form (d) and grow (e) upon further annealing [39].

slip of dislocations. The driving force for cell formation is the energy release due to a reduction of dislocation density. The dislocations inside the cell walls then arrange geometrically to form low angle grain boundaries (LAGB). This process is driven by the formation of fewer, more highly misoriented boundaries. The so formed subgrains (d) grow upon further annealing (e), while reducing the total boundary area [39,62]. The presence of solute atoms and fine distributions of second phase particles may inhibit or retard recovery by pinning dislocations and subgrain boundaries [58].

The amount of recovery observed in a material strongly depends on the stacking fault energy γ_{sf} of the alloy. As explained previously, the stacking fault energy describes the extent to which dislocations dissociate and split up into partial dislocations. In other words, it determines the possibility of dislocation climb and cross-slip, the main recovery mechanisms [39]. Stainless steels with low γ_{sf} [63], for example, show only limited recovery. In contrast, recovery plays an important role in materials with high γ_{sf}, such as Al. The presence of Mg in Al reduces γ_{sf} linearly with Mg content, however, technical Al-Mg alloys still possess medium to high γ_{sf} values [59]. Mg is known to pin dislocations in Al and may partly inhibit recovery by segregating at dislocations [39].

2.2.2 Recrystallization

Recrystallization is a process, in which new grains are formed in a previously deformed microstructure. These new grains have a dislocation density of non-deformed material. During the transformation process, the new grains consume the deformed microstructure. In contrast to recovery, which occurs rather homogeneously in a sample volume, the microstructure during recrystallization is at any time divided into recrystallized and non-recrystallized regions. The recrystallization sequence shown in Fig. 2.12 illustrates the heterogeneity of the transformation. In a deformed (a) or partially recovered (b) mi-

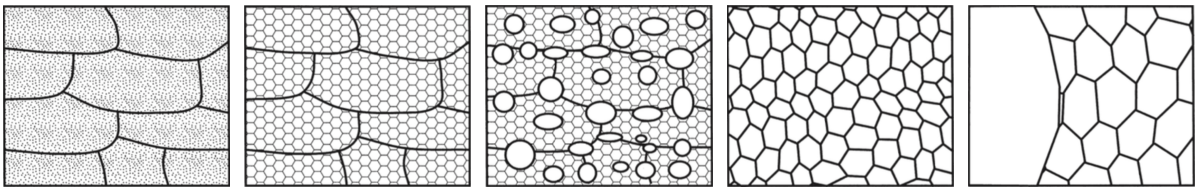

(a) Deformed (b) Partial RV (c) Partial RX (d) Full RX (e) Abnormal GG

Fig. 2.12: Stages of recrystallization: In a deformed (a) or partially recovered (RV) (b) microstructure, new grains nucleate (c) and grow until full recrystallization (RX) is reached (d). Abnormal grain growth (e) may occur on further annealing [39].

crostructure, new grains nucleate in highly distorted regions (c) and grow by movement of high angle grain boundaries (HAGB) until the microstructure is fully recrystallized (d). Thereafter, the grains may grow homogeneously or abnormal grain growth (e) may occur. Based on Fig. 2.12, the kinetics of recrystallization is often divided into nucleation and growth stages. While nucleation is related to the formation of dislocation-free regions, growth involves the movement of HAGB due to an existing driving pressure, as derived in the following section. A third stage, normal or abnormal grain growth, occurs in a fully recrystallized material. Recrystallization kinetics in single phase alloys is often described by the JMAK equation (Eq. 2.28), similar to the kinetics of precipitation [39,62,64].

In general, recrystallization requires higher degrees of plastic deformation and annealing temperature than recovery. Summarizing the correlations derived by Humphreys and Hatherly [39]: The higher the degree of plastic deformation, the lower is the temperature at wich recrystallization occurs and the smaller is the final recrystallized grain size.

2.2.2.1 Driving pressure for recrystallization

In general, a high angle grain boundary moves if the net pressure on the boundary is positive. In the context of recrystallization, two cases have to be differentiated. The first one refers to a situation where both recrystallized and non-recrystallized grains are present (Fig. 2.12 c) and full recrystallization has not been reached. The total net pressure P_1 that acts on a HAGB in such a situation can be expressed with [39]:

$$P_1 = P_D - P_C - P_Z, \tag{2.30}$$

where P_D is the driving pressure, P_C the boundary curvature pressure, and P_Z represents the Zener pinning pressure. The driving pressure for recrystallization P_D is provided by

the dislocation density and is mathematically formulated by [39]:

$$P_D = \alpha_2 \, \rho \, G \, b^2. \tag{2.31}$$

Here, α_2 is a constant of the order of 0.5 and ρ, G, and b have their common meanings. Since P_D increases linearly with the dislocation density, it depends significantly on the local degree of plastic deformation. The boundary curvature pressure P_C opposes the boundary movement in the given situation, because the grain boundary area increases as the recrystallized grain grows, thus increasing the total energy. However, P_C is only significant in the very early stages of recrystallization when the grains are in the range of around 1 µm [39].

The second case that needs to be considered is given when full recrystallization has already been reached (Fig. 2.12 d) and $P_D = 0$. The driving pressure for grain growth is then expressed by:

$$P_2 = P_C - P_Z. \tag{2.32}$$

In that case, P_C is the driving force for grain growth aiming to reduce the total grain boundary area. The driving pressure for grain growth P_2 is around two orders of magnitude smaller than that for primary recrystallization P_1, assuming constant P_Z [39].

2.2.2.2 Zener pinning pressure

The Zener pinning pressure P_Z describes the interaction of second-phase particles with boundaries. P_Z always opposes the driving pressures for boundary movement (Eq. 2.30 and 2.32). Precipitates exert a retarding pressure on moving LAGBs and HAGBs, thus have significant influence on recovery and recrystallization in multi-phase alloys [39].

According to Nes *et al.* [65], the mechanism of Zener pinning is based on a reduction of boundary area when a moving boundary intersects a particle. Lower boundary area results in lower energy of the system, thus boundaries are attracted to particles. They [65] found that the maximum restraining force F of a single spherical particle equaled:

$$F = \pi r \gamma, \tag{2.33}$$

with the particle radius r and the boundary energy γ. The restraining force can reach multiples of that of spherical particles by modifying the particle shape. It was proposed

by the same authors, that F increased with increasing ellipsoid eccentricity but depended on the interaction direction. Independent of the particle shape, the magnitude of the restraining force (Eq. 2.33) is based on the nature of the interphase between particle and boundary. If a HAGB moves past a coherent interface, in general, particle coherence will be lost. The energy of the new incoherent interface is higher than that of the original coherent interface, thus additional energy must be supplied by the moving boundary. Therefore, coherent particles are more efficient in pinning boundaries than incoherent ones. The restraining force of a coherent particle F_c is twice as large as of an incoherent particle (Eq. 2.33) [39,65]:

$$F_c = 2\pi r\gamma. \tag{2.34}$$

The Zener pinning pressure of a population of coherent precipitates, based on [39,65], is derived as follows. The number of spherical particles with radius r and volume fraction f_V per unit volume is given by:

$$N_v = \frac{3f_V}{4\pi r^3}. \tag{2.35}$$

The number of particles that intersect a planar boundary is:

$$N_p = 2rN_v = \frac{3f_V}{2\pi r^2}. \tag{2.36}$$

The pinning pressure of coherent particles on unit area of the boundary equals:

$$P_Z = N_p F_c. \tag{2.37}$$

Combining Eqs. 2.34, 2.36, and 2.37 leads to the formulation of the Zener pinning pressure of a population of spherical, coherent particles:

$$P_Z = \frac{6f_V\gamma}{2r}, \tag{2.38}$$

with the precipitate volume fraction f_V, the grain boundary energy γ, and the precipitate radius r. According to Eq. 2.38, P_Z has a high value for a large number of small precipitates. If P_Z exceeds $(P_D - P_C)$, the boundary movement, i.e. the recrystallization process, stops and full recrystallization is not reached (Eq. 2.30). If P_Z exceeds P_C in a fully recrystallized microstructure, further grain growth is inhibited (Eq. 2.32).

Knowledge about the precipitation and recrystallization processes can be used, for example, to control the grain size during annealing [66]. The significant impact of small precipitates on the recrystallization behavior of various Al-alloys was demonstrated in several studies [67–69].

2.2.2.3 Strain induced boundary migration

The nucleation process in the context of recrystallization differs from that of precipitation. According to Humphreys and Hatherley [39] as well as Doherty *et al.* [64], classical nucleation theory involving random atomic fluctuations leading to the formation of stable crystallites with HAGBs is very unlikely due to low driving force and large interfacial energy. Instead, nuclei from which recrystallized grains originate are small volumes which pre-exist in the deformed structure. This understanding serves as a basis for a mechanism referred to as strain induced boundary migration.

Strain induced boundary migration (SIBM) involves the bulging and movement of a part of a pre-existing boundary, leaving a dislocation-free region behind the migrating boundary. Characteristically, the new grains have similar orientation to the old grains from which they originate. The driving force for SIBM arises from a difference in dislocation density on opposite sides of the grain boundary. The boundary, or nucleus, grows towards the deformed grain aiming for an energy reduction [39].

Nucleation occurs at locations with high dislocation density and orientation gradient. Typical nucleation sites for recrystallization are grain boundaries, transition bands, shear bands, and highly misoriented zones around large particles [39,64]. The nucleation at large particles is explained in the following section.

2.2.2.4 Particle-stimulated nucleation

Particle-stimulated nucleation (PSN) refers to a phenomenon where nuclei of recrystallized grains are formed in the vicinity of large, non-deformable second phase particles. These particles are usually in the range of some microns. During the deformation of an alloy containing such non-deformable particles, the strain gradient enforced in the vicinity of the particles creates a region of high dislocation density and large orientation gradients. This deformation zone is an ideal site for the development of a recrystallization nucleus. The deformation zone extends to around one particle diameter from the particle surface. Accordingly, depending on the degree of plastic deformation, PSN is more effective with increasing particle size [64,70].

PSN may be used to control the recrystallization texture and grain size by introducing, for example, ceramic particles to Al-alloys. PSN was also observed in the vicinity of large second phase particles that were formed by conventional heat treatments prior to cold deformation and recrystallization annealing [39,70].

2.3 Alloying concept Al-Sc

Al-Mg-Sc-Zr alloys with technically relevant chemical compositions have less than 6 wt.% Mg, 1 wt.% Sc, and 0.5 wt.% Zr [54]. The concentration of Mg is the highest of all alloying elements, hence such alloys are in general considered as Al-Mg alloys modified with Sc and Zr. Despite the high Mg-content, however, the dominant metallurgical system for Al-Mg-Sc-Zr alloys is the Al-rich side of the binary system Al-Sc. Therefore, in this section, first the general basics of the Al-Sc system are introduced. Thereafter, these fundamentals are specifically adapted to Al-Sc alloys with additions of magnesium and zirconium.

2.3.1 Aluminum

Aluminum is the most heavily consumed non-ferrous metal and the second most plentiful metallic element on earth. Pure aluminum is usually electrolytically extracted from Al_2O_3 Al-oxide which itself is in most cases refined from Bauxite. Pure Al has a high electrical and thermal conductivity, is nonferromagnetic and is corrosion resistant over a wide range of pH-values. Aluminum presents a face-centered cubic (fcc) crystal structure over the whole temperature range up to the melting point at 933 K (660°C). The unit cell has a lattice constant of 4.0414 Å at room temperature and an atomic packing factor of 0.74. The closest distance between two neighboring atoms is 2.863 Å which gives an atomic radius of around 1.43 Å [71].

The success of Al as a material for structural components for lightweight design is based on two major properties: high specific strength and stiffness. Aluminum has a low density of 2.7 g/cm^3 compared to steel with 7.85 g/cm^3 or titanium with 4.54 g/cm^3. Even though pure Al having an ultimate tensile strength of around 50 MPa is a rather soft material, its alloys may reach tensile strenghts up to several hundred MPa. The consequence of low density and relatively high strength is a high specific strength. The Young's modulus of Al and its alloys ($E_{Al} = 70$ GPa) is about three times smaller than that of steel and the ratio of Young's modulus to materials density is essentially the same for Al-alloys and steels. Accordingly, direct replacement of steels with Al-alloys

without modifying the geometry of a component does not increase its stiffness. On the other hand, when the thickness of a simple beam subjected to bending load, for example, is adapted to the materials properties, the use of Al instead of steel reduces the weight by about 50% while achieving the same stiffness of the component. The combination of high specific strength and stiffness with excellent corrosion resistance, makes Al-alloys attractive as structural materials for many industry branches, in particular for aircraft industries [15,72].

Aluminum alloys are categorized according to the major alloying elements contained and are classified as heat-treatable or non-heat-treatable. An overview of the series of wrought Al-alloys with their major alloying elements according to the International Alloy Designation System is listed below. Most of the alloys of the 2xxx, 6xxx, and 7xxx series are heat-treatable. In general, those alloys such as Al-Cu possess higher strength than non-heat-treatable ones such as Al-Mg. Since this study focuses on specific Al-Mg-Sc-Zr alloys, details on the metallurgy of pure aluminum and other alloys are omitted in this section. For further reading the author refers to handbooks, e.g. [15,73,74].

Series of wrought Al-alloys [15,40]

- 1xxx: pure Al
- 2xxx: Al-Cu
- 3xxx: Al-Mn
- 4xxx: Al-Si
- 5xxx: Al-Mg
- 6xxx: Al-Mg-Si
- 7xxx: Al-Zn
- 8xxx: Al-other elements

2.3.2 Scandium

Scandium is a light metal that occurs in more than 800 different mineral species with an average abundance in the Earth's crust of 25 ppm. Even though the occurrence of Sc exceeds that of Mo, Sn, W, Ag, and Au, scandium is considered a rather exotic element. This is mainly due to the fact that it is not concentrated in economically exploitable deposits but is dispersed in rock-forming minerals. Today, scandium is mainly produced as a subproduct during processing of various ores but undiscovered ressources are probably very large [10].

Scandium is a light metal with a density of $2.99\,g/cm^3$ at room temperature and a melting point of $1814\,K$ (1541°C). The crystal structure is hexagonal close packed (hcp) and the atomic radius equals 1.6 Å. Pure scandium has a Young's modulus of 79.3 GPa [75].

According to Røyset and Ryum [9] pure scandium has virtually no application at present due to its limited availability and high price. However, there are some fields were Sc is used as additive amongst which the most important one certainly is the function as an alloying element in aluminum alloys [10]. The reason for this is quite simple: when added to aluminum, scandium provides the highest increment of strengthening per atomic percent compared to any other alloying element.

2.3.3 The binary system Al-Sc

Figure 2.13 shows a complete Al-Sc phase diagram. The equilibrium phases are Al, Al_3Sc, Al_2Sc, AlSc, $AlSc_2$, and Sc. For structural applications only Al-alloys modified with small amounts of Sc are relevant, thus the Al-rich part of the phase diagram is of particular interest. This section is shown in detail in Figure 2.14 (a). Apparently, the only Sc-rich equilibrium phase present in an alloy with Sc-contents below 1 wt.% is Al_3Sc. When exceeding the eutectic composition of 0.55 wt.% Sc, Al_3Sc is formed as a primary phase upon solidification. The solidification of such an alloy is finished with the formation of eutectic α-Al+Al_3Sc at 660°C. Upon further cooling, secondary Al_3Sc phases precipitate from the α-Al matrix until room temperature is reached. The maximum solid solubility of Sc in Al is 0.4 wt.% at 660°C. This solid solubility, however, deacreases rapidly with temperature, as illustrated in Figure 2.14 (b), and is reduced to values close to 0 wt.% at room temperature. The exact compositions and temperatures in the phase diagrams are still under discussion [9].

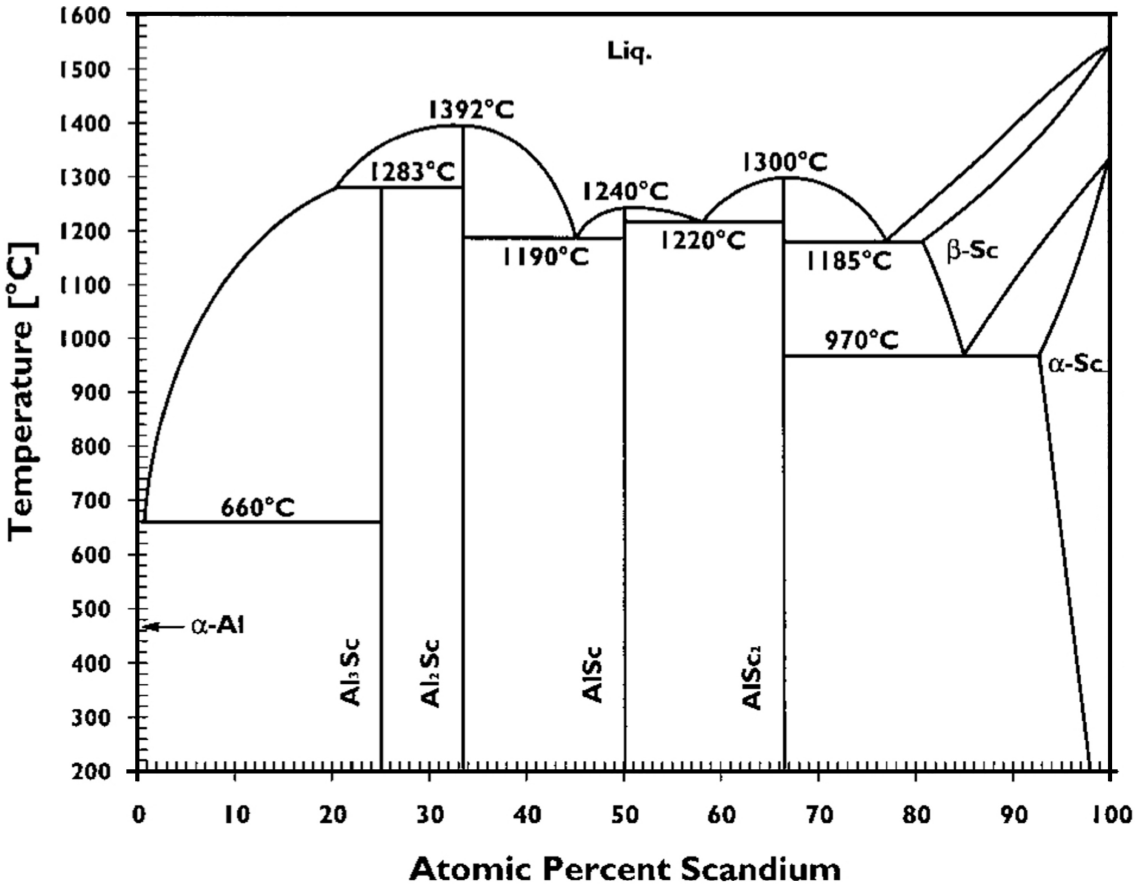

Fig. 2.13: Binary Al-Sc phase diagram [76].

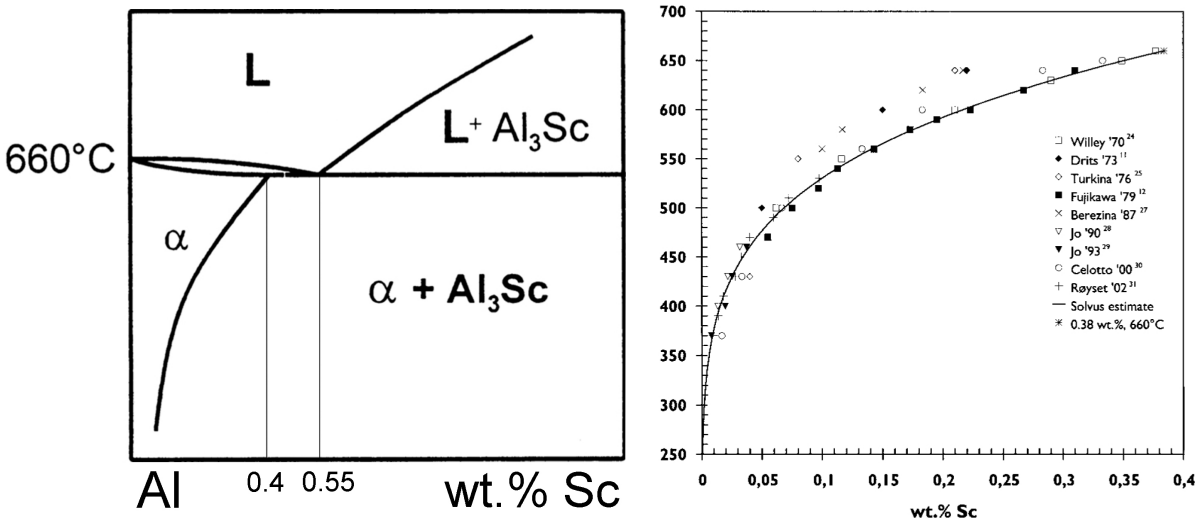

(a) Al-rich region of Al-Sc phase diagram [77]

(b) Solubility of Sc in solid Al [9]

Fig. 2.14: Al-rich region of the binary Al-Sc phase diagram (a) and solubility of Sc in Al as a function of temperature (b) [9,77].

2.3.4 Al_3Sc phase

The properties of alloys that follow the Al-Sc system strongly depend on the presence and nature of the equilibrium phase Al_3Sc. Therefore, the formation of this phase and the resulting properties are discussed more in detail.

Al_3Sc phase has the $L1_2$ type cubic unit cell with a lattice parameter of 4.1 Å. As illustrated in Figure 2.15, Al atoms are located at the cube faces while Sc atoms are found at the corners. In equilibrium, Al_3Sc may form in three ways depending on the chemical composition [9,42]:

1. Al_3Sc is the first solid phase to form upon solidification in case of a hypereutectic alloy with > 0.55 wt.% Sc.
2. The solidification of alloys with Sc-content > 0.4 wt.% finishes with the formation of eutectic α-Al+Al_3Sc.
3. Secondary Al_3Sc phases precipitate from the α-Al matrix during cooling.

For non-equilibrium solidification and cooling, the formation of both primary and secondary Al_3Sc phases may be suppressed. In that case, an α-Al matrix supersaturated in Sc is formed, facilitating the formation of secondary Al_3Sc precipitates in an annealing treatment. The effect of Al_3Sc phases on the microstructure and properties of Al-Sc alloys is discussed in the following sections.

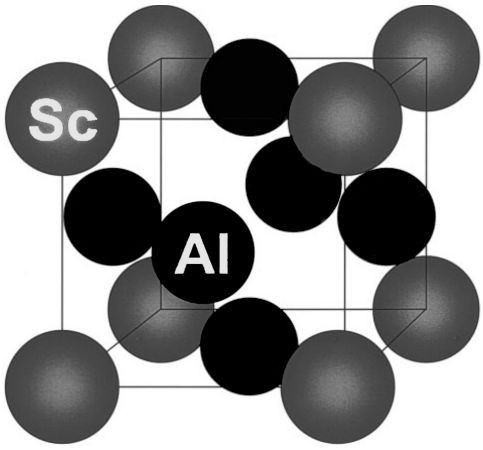

Fig. 2.15: $L1_2$ unit cell of Al_3Sc phase having Al atoms located at the cube faces and Sc atoms at the corners [9].

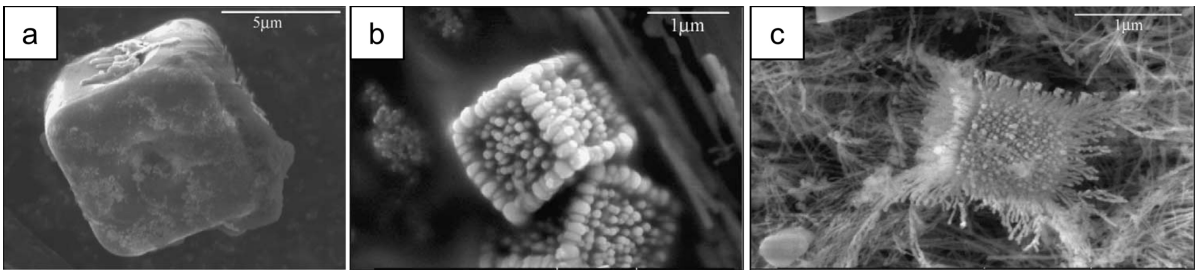

Fig. 2.16: Morphology of primary Al_3Sc phases with different cooling rates; (a) $1\,Ks^{-1}$, (b) $100\,Ks^{-1}$, (c) $1000\,Ks^{-1}$ [78].

2.3.4.1 Primary Al_3Sc

The nucleation behavior and morphology of primary Al_3Sc was studied in detail by Hyde *et al.* [78]. It was shown that the shape of Al_3Sc phases was in general cubic, whereas the morphology was slightly modified with increasing cooling rate, as illustrated in Figure 2.16. Higher cooling rates led to the formation of an internal substructure, while the overall morphology of the primary Al_3Sc phases was still cubic. The substructure resulted from interconnected dendritic arms growing with direction-dependent velocities. In good agreement to this fundamental study, other researchers e.g. [79,80] also reported of primary Al_3Sc phases with cubic or similar regular shapes.

2.3.4.2 Eutectic α-Al+Al_3Sc

The eutectic α-Al+Al_3Sc was only vaguely described in the existing literature as it has no particular influence on the microstructure and properties of Al-Sc alloys [9]. It was, however, shown [78] that eutectic α-Al+Al_3Sc was found at grain boundaries in an Al-Sc0.7 alloy. Little additional information about the eutectic is provided in [9].

2.3.4.3 Secondary Al_3Sc

In equilibrium, secondary Al_3Sc phases form during cooling as the solubility of Sc in α-Al is reduced with decreasing temperature (Fig. 2.14). The more important formation mechanism with respect to the mechanical properties of the alloy, however, is the targeted precipitation from a supersaturated solid solution, as explained in section 2.1.3. If an Al-alloy supersaturated in Sc is annealed, secondary Al_3Sc precipitates are formed either by discontinuous or continuous precipitation [9]. Discontinuous precipitation refers to a mechanism, where a supersaturated solid solution decomposes to a less supersaturated solution and Al_3Sc particles behind a moving grain boundary. Continuous precipitation is described by classical nucleation and growth theory. Discontinuous precipitation in

Al-Sc alloys was only observed in two cases: first, after quenching of alloys with high Sc-content (0.7 wt.%) [79]; second, after direct quenching from homogenization temperature (600°C) to various annealing temperatures in an alloy with a Sc-content of 0.2 wt.% [42]. As the present study focuses on neither of these cases, the phenomena involved in discontinuous precipitation are not discussed in detail.

Continuous precipitation describes the formation of secondary Al_3Sc phases during ageing of a supersaturated solid solution of Sc in Al. The Al_3Sc precipitation kinetics is well described with the JMAK relationship and depends strongly on the ageing temperature and degree of Sc-supersaturation [9]. Typical annealing temperatures for precipitation in Al-Sc alloys lie within 250°C and 500°C, whereas highest strength was achieved between 250°C and 350°C [77]. This temperature range is considerably higher than for most other age-hardening types of Al-alloys. Al-Cu and Al-Mg-Si are usually aged between 150°C and 200°C, while the annealing temperature for Al-Mg-Zn is even lower with around 100°C to 180°C [15].

Nucleation starts directly with the formation of the equilibrium $L1_2$ phase Al_3Sc as there is no indication of any metastable phases [9]. The nucleation of coherent precipitates occurs either homogeneously in the matrix or heterogeneously at dislocations, depending on the degree of Sc-supersaturation and the dislocation density [41,81]. Robson *et al.* [41] proposed a model to predict the dominant nucleation mechanism based on Sc-content and dislocation density, as shown in Fig. 2.17 (a). The lines represent multiples of a dislocation density of $1.5 \cdot 10^{11}\ m^{-2}$, and indicate a dominance of the homogeneous nucleation mechanism over a wide range of dislocation densities and Sc-concentrations. Heterogeneous nucleation is only significant when a combination of high temperature, low degree of supersaturation, and high dislocation density is given. In such a situation, the elastic strain fields surrounding the forming nuclei are relevant. Dislocations are then favored nucleation sites because the precipitates surrounded by compressive strain fields are attracted by the local tension close to dislocations. In agreement to the model, Jones *et al.* [82] showed that homogeneous nucleation dominated in deformed and non-deformed Al-0.25 Sc (wt.%). Further results by Novotny and Ardell [81] were also in qualitative agreement with the model of Robson *et al.* [41].

The Al_3Sc precipitation kinetics is faster at higher temperature and contents of solute Sc in α-Al. The time-temperature-transformation (TTT) curves in Fig. 2.17 (b) show faster Al_3Sc precipitation in case of higher Sc-content due to larger driving force for nucleation and growth. Faster transformation kinetics in case of increasing Sc-concentration was also reported by Zakharov [83]. The JMAK exponent n ranged from around 1.3 to 2 in-

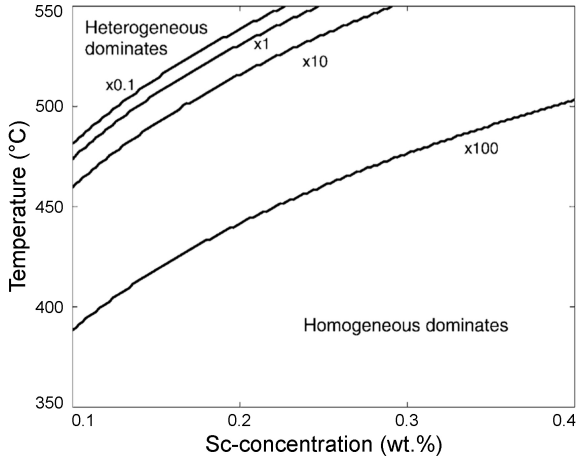

(a) Regions of dominant homogeneous and heterogenous nulceation as multiples of initial dislocation density $1.5 \cdot 10^{11}\,\mathrm{m}^{-2}$

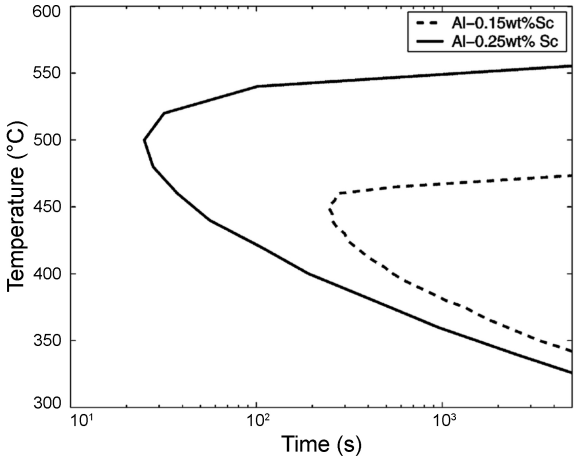

(b) Predicted TTT curves for Al_3Sc precipitation showing times to reach 90 % transformation of the equilibrium volume fraction

Fig. 2.17: Predictive model by Robson *et al.* [41] showing the dominating nucleation mechanism (a) as well as the time and temperature dependent transformation (TTT) for different Sc-contents (b).

dicating nucleation site saturation, i.e. that all the particles nucleated in a short period of time, rather than at a constant nucleation rate [9,42]. As expected (Eq. 2.21), the precipitate growth rate increased with increasing ageing temperature [42]. The coarsening stage of Al_3Sc occurs after longer ageing times compared to most other precipitates in Al-alloys [9]. Iwamura and Miura [84] attributed this behavior to the low diffusivity of Sc and the coherent interface between particle and matrix that is maintained for long times. They observed an increasing coarsening rate when the coherency of Al_3Sc precipitates was lost at sizes between 15 and 40 nm.

The shape of secondary Al_3Sc precipitates was reported to be spherical in most cases, e.g. [42,81,82,85,86]. Other shapes, in addition, were only found after days [86] or even weeks [81] of ageing and will not be discussed here in detail since these treatments are irrelevant for any practical application.

2.3.5 Addition of further elements

The transformation temperatures and chemical compositions of the individual phases of the Al-Sc system are influenced by any other alloying element added to the system. Zakharov [83] demonstrated the influence of several elements including Mg, Zr, Zn, Fe, and Si on the precipitation kinetics of the Al_3Sc phase. Other studies described, for

example, the influence of Cu additions [87], the behavior of Mn-alloyed materials [88] or alloys including Mn and Cr [89]. This section focuses on the influence of the addition of Mg and Zr on the Al-Sc system.

2.3.5.1 Magnesium

While Mg and Sc mutually reduce the solubility of each other in Al, no ternary AlMgSc phases could be found in the Al-rich corner of the Al-Mg-Sc system [9]. The reduced solubility of Sc in Al-Mg compared to that of Sc in Al shifts the eutectic Sc-concentration to lower values. In a binary Al-Sc alloy, a minimum of 0.55 wt.% Sc is required to form primary Al_3Sc phases (Fig. 2.14 a). In an Al-Mg-Sc alloy, however, it was shown [42,90] that as little as 0.2 wt.% Sc may be sufficient to produce primary Al_3Sc phases. The formation of secondary Al_3Sc precipitates was in general unaltered by the presence of Mg [18,83,91]. However, Zakharov [83] suggested that the precipitation kinetics was slightly faster in the presence of Mg than in binary Al-Sc alloys as a result of the reduced solid solubility.

The precipitate radius r_t, at which the transition from particle shearing to Orowan looping occurs (Fig. 2.6), equaled 2.1 nm for a binary Al-Sc alloy [38] and increased to 2.4 nm by adding 2 wt.% Mg [18] for a constant precipitate volume fraction. This increase of r_t resulted of a reduced lattice mismatch between particle and matrix due to the addition of Mg leading to a reduction of the coherency strengthening term (Eqs. 2.8 and 2.9).

2.3.5.2 Zirconium

The addition of Zr to Al-Sc may lead to the formation of the additional phase Al_3Zr [9]. The metastable variant of the Al_3Zr phase having $L1_2$ crystal structure is an effective dispersoid strengthener in several Al-alloys [67,92–94]. These dispersoids are usually formed during homogenization of cast billets and inhibit recrystallization in the following thermo-mechanical treatments. In the context of precipitation hardening of Al-Sc-Zr alloys, however, the individual formation of both Al_3Sc and Al_3Zr is not desired [9].

If scandium and zirconium are added in a weight ratio of around 2:1, full solubility of Zr in Al_3(Sc,Zr) can be achieved [95]. The formation of precipitates of the type Al_3(Sc,Zr) is more favorable with respect to the mechanical properties than an individual appearance of both Al_3Sc and Al_3Zr [96–98]. While the nucleation and growth stages of Al_3(Sc,Zr) are very similar to that of Al_3Sc, the coarsening stage is significantly retarded for the ternary phase as a result of its complex composition [44,95,99–103]. It was demonstrated, e.g.

[44,95], that $Al_3(Sc,Zr)$ precipitates have a distinct heterogeneous composition revealing a Sc-rich core and a Zr-rich shell. Amongst others, Deschamps *et al.* [44] attributed this core-shell structure to the lower diffusion coefficient of Zr compared to Sc in Al. As a consequence of the heterogeneous composition, the precipitate coarsening stage is controlled by the movement of slowly diffusing Zr. Therefore, precipitate coarsening occurs significantly slower in ternary Al-Sc-Zr compared to binary Al-Sc alloys.

2.4 Al-Mg-Sc-Zr alloys

This section summarizes the metallurgical properties of Al-Mg-Sc-Zr alloys derived from the fundamental discussion of the literature. First, the strengthening mechanisms that apply to Al-Mg-Sc-Zr alloys are discussed regarding the chemical composition and thermo-mechanical processing history. Second, the resistance to recrystallization and grain growth due to $Al_3(Sc,Zr)$ precipitates is summarized. Third, the need for rapid solidification in order to produce high strength Al-Mg-Sc-Zr alloys is discussed. Finally, the most important open questions are highlighted, that need to be clarified in order to control the materials properties of a novel alloy produced on industrial equipment.

2.4.1 Strengthening

Grain size hardening is a very efficient way to increase the strength of a wide range of materials without necessarily modifying their chemical compositions, as introduced in section 2.1.2. Grain refinement in Al-(Mg)-Sc-(Zr) alloys is achieved by the formation of primary Al_3Sc or $Al_3(Sc,Zr)$ phases. Several studies [78–80,90,104,105] demonstrated that primary $Al_3(Sc,Zr)$ phases serve as nucleation sites for α-Al grains leading to considerable grain refinement. The addition of 0.55 wt.% Sc, for example, reduced the grain size by two orders of magnitude for an Al-alloy [79]. Costa *et al.* [80] presented a study on Al-Sc alloys with 0.5, 0.7, and 1 wt.% Sc, where they demonstrated that not only the grain size decreased with increasing Sc-content but also that the roundness of the single grains increased. The grain morphology changed from large columnar grains to more favorable small equiaxed grains with very limited dendritic substructure. For castings, Sc was found to be a more effective grain refiner than the usually used TiB_2 [90]. The lattice misfit between α-Al and Al_3Sc is very low, for example 1.33% at room temperature or 0.47% at the eutectic temperature. This low lattice misfit facilitates hetereogeneous nucleation of α-Al grains at primary Al_3Sc phases during solidification leading to grain refinement[106].

Despite the substantial grain refining effect of primary $Al_3(Sc,Zr)$ phases, no substantial grain size hardening was observed for the investigated alloys, e.g. [80,104]. The small grain sizes achieved using casting processes were still too big to affect the yield strength significantly. These results are in good agreement to the reported low Hall-Petch slopes (k_2 value in Eq. 2.6) for Al-alloys. In order to achieve high-strength Al-Mg-Sc-Zr alloys, therefore, the controlled formation of primary $Al_3(Sc,Zr)$ to produce fine α-Al grains is not a promising way.

High strength in Al-Mg-Sc-Zr alloys results of a combination of solid solution hardening due to Mg, precipitation hardening from secondary $Al_3(Sc,Zr)$ particles [18,77,91], and, if applied, strain hardening due to plastic deformation [17,107]. Fig. 2.18 illustrates the influence of Mg (a) and Zr (b) additions on the microhardness evolution of Al-Sc alloys. The binary Al-Sc alloy in Fig. 2.18 (a) shows a typical precipitation hardening curve. A rather constant offset to higher values is achieved by adding Mg resulting from the superposition of solid solution and precipitation strengthening. The comparison of the Al-0.2Sc alloy in Fig. 2.18 (a) and the Al-0.4Sc alloy in Fig. 2.18 (b) illustrates the influence of the Sc-content on the strength. A higher Sc-concentration considerably increases the maximum strength of the alloy. The positive impact of Zr addition on the hardness is demonstrated in Fig. 2.18 (b). While the binary Al-Sc alloy shows the typical hardness drop associated with precipitate coarsening, this effect is considerably retarded by adding appropriate amounts of Zr. The initial stages of precipitation and the maximum hardness, however, are not significantly affected by the presence of Zr.

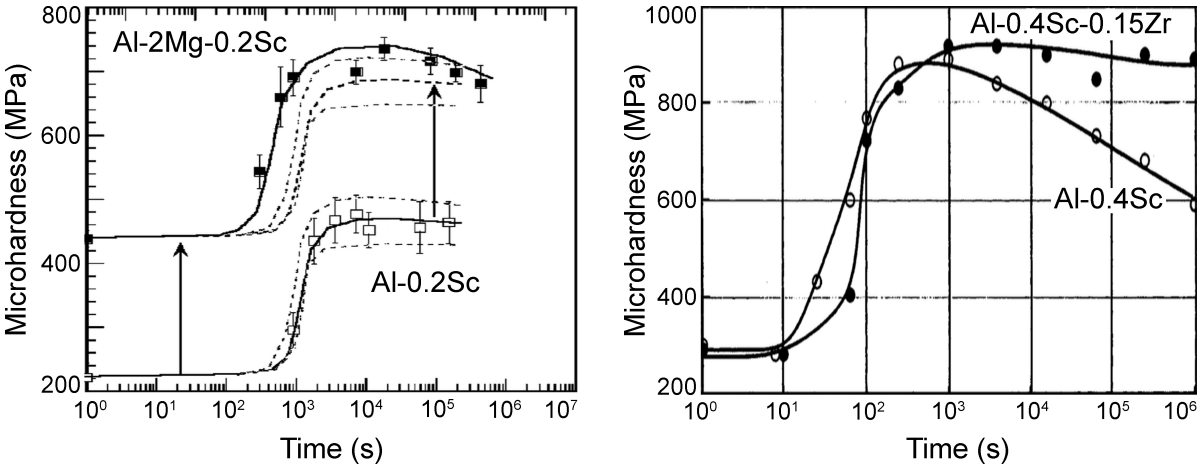

(a) Influence of Mg addition to Al-Sc [18]

(b) Influence of Zr addition to Al-Sc [77]

Fig. 2.18: Superposition of Mg solid solution and Al_3Sc precipitation strengthening (a) and retarded coarsening due to Zr addition (b) in Al-Sc during annealing at 350°C.

The strain hardening behavior of Al-Mg-Sc-Zr strongly depends on the presence and nature of Al_3(Sc,Zr) precipitates prior to deformation. It was shown [107] that the work-hardening rate was low for underaged material as the precipitates were sheared by dislocations. In overaged condition, on the other hand, more pronounced work hardening was observed due to interactions of dislocations with larger, non-shearable particles.

2.4.2 Recrystallization resistance

The strength of work hardened Al-Mg material is in general lost in a following heat treatment due to recrystallization and recovery. Conventional Al-Mg3 deformed to 0.8 strain showed full recrystallization after only 5 min of isothermal ageing at 360°C [108]. The presence of Al_3Sc or Al_3(Sc,Zr) in similar alloys, on the other hand, significantly limited both recovery [109] and recrystallization [82,88,108,110–112] processes due to Zener pinning. Ocenasek and Slamova [108], for example, showed that the addition of 0.25 wt.% Sc and 0.08 wt.% Zr to Al-Mg3 was sufficient to limit the fraction of recrystallized material to less than 3% even when annealed for 8 h at 520°C.

Grain growth is considerably impeded in fine grained Al-Mg-Sc and Al-Mg-Sc-Zr alloys. Various authors [96,113–120] reported on ultra-fine grained microstructures produced by equal-channel angular pressing (ECAP). Quaternary Al-Mg-Sc-Zr provided best stability of ultra-fine grains compared to ternary Al-Mg-Sc or Al-Mg-Zr alloys due to the formation of Al_3(Sc,Zr) precipitates [96]. Fine grains were also produced via friction stir processing (FSP) [121–125] or other severe plastic deformation methods [126–129]. In all cases, the grain structure could be maintained in the presence of Al_3(Sc,Zr) precipitates.

2.4.3 Rapid solidification

High strength and recrystallization resistance require the formation of secondary Al_3Sc or Al_3(Sc,Zr) precipitates. The precipitation of the phase, in turn, requires the presence of a solid solution supersaturated in Sc prior to ageing. For most Al-alloys, supersaturation in the main precipitate forming element(s) is achieved by a solution heat treatment followed by quenching (Fig. 2.5). Typical solution temperatures for 2xxx [47], 6xxx [48], or 7xxx alloys [130] lie within 480°C to 530°C. Similar procedures were carried out for Al-Sc alloys, e.g. [42,81,85,86], however, the employed solution temperatures were considerably higher ranging up to 650°C for a maximum Sc concentration of 0.3 wt.%. These high temperatures are a natural consequence of the limited solubility of Sc in α-Al, as shown in Fig. 2.14, and conventional solution temperatures of around 500°C would dissolve only as little as 0.07 wt.% Sc. All the studies on Al-Sc alloys mentioned before,

for example [42,81,85,86], were carried out to study microstructural features using small volume samples produced on laboratory scale. For applications on industrial scale, on the other hand, a solution heat treatment close to the melting temperature is not feasible, simply because heavier parts such as entire coils would severely plastically deform under their own weight at these temperatures.

Rapid solidification, i.e. quenching from liquid state, is used to cross phase boundaries fast enough to totally, or at least partially, prevent the formation of equilibrium phases. Such solidification is achieved by imposing a high cooling rate during solidification, which requires that the melt is in good contact with an effective heat sink. Non-equilibrium phases formed by rapid solidification include glasses, quasicrystalline phases, new crystalline phases, and equilibrium phases with extended composition range [131,132]. In the current context, the extension of the solid solubility beyond the equilibrium level is of particular interest.

Solid solutions with chemical compositions far beyond equilibrium can be produced by rapid solidification if the velocity of the solidification front is higher than the diffusive atomic motion of solute trying to escape [133]. As an example, by applying this principle, up to 15 wt.% Cu were dissolved in solid Ag, whereas the equilibrium solid solubility of Cu in Ag is around 9 wt.% at the eutectic temperature (~ 780°C) and is close to 0 wt.% at room temperature [134,135]. Apparently, not only the formation of secondary but also of primary Cu-rich phases was suppressed.

Rapid solidification processes seem to be ideal candidates to produce Al-Mg-Sc-Zr alloys with a high degree of Sc supersaturation, even with hypereutectic composition. According to [136], solidification and cooling rates of around 100 Ks^{-1} should be sufficient to form a supersaturated solid solution with 0.7 wt.% Sc. This hypothesis is somewhat contradictory to the observed small primary phases in an Al-0.4 wt.% Sc alloy solidified at 1000 Ks^{-1} [78]. However, a minimum required solidification rate was not tested in the available literature so far, and the applied methods [136–138] revealed cooling rates even higher than 1000 Ks^{-1}. Herding *et al.* [136] studied a spray formed Al-4.5Mg-0.7Sc-0.1Zr-0.5Mn alloy (wt.%) solidified with up to 10^5 Ks^{-1}. The entire alloy content was in solution after the initial production process and considerable precipitation hardening was achieved in a following thermo-mechanical treatment. In rolled and annealed condition, this material exceeded the mechanical properties of Al-Cu-Mg alloy 2024. However, to produce a large volume material in sheet metal condition, the proposed processing route based on spray forming is probably not suitable.

Selective laser melting (SLM) was applied to produce and characterize prototype parts made of Scalmalloy® Al-4.5Mg-0.66Sc-0.37Zr-0.51Mn (wt.%) [137]. SLM uses powder material that is molten and solidified layer by layer reaching solidification rates well in excess of $10^3\,\mathrm{Ks}^{-1}$. In the paper, no details on the microstructure or precipitate evolution are given, however, the strength levels after ageing reached values similar to [136], thus the suppression of primary and secondary Al_3(Sc,Zr) due to SLM can be assumed. In a similar study, Rometsch et al. [138] demonstrated that a large amount of Sc can be brought in solution using SLM, but that the Sc-concentration varied significantly from the bottom to the top of the manufactured part. They suggest to carefully control the thermal history of the component to avoid the formation of coarse Al_3(Sc,Zr) at the bottom, while building-up new layers on top. At present, SLM is a highly promising technique to produce complex parts with outstanding mechanical properties, but is not considered as a method to produce large volume components.

Only one recent study in the available literature deals with a rapidly solidified Al-Mg-Sc-Zr alloy that is produced as a precursor material for sheet metal parts. The study by Mousavi Anijdan *et al.* [139] characterizes the mechanical properties of a strip casted Al-Mg alloy containing 0.4 wt.% Sc and 0.15 wt.% Zr. After strip casting to 10 mm thickness, cold rolling (1 mm), and ageing for several hours at 300°C, a yield strength of around 400 MPa was reached. The results of the mechanical properties seem to be promising, however, the study reveals no details on the Sc-content in solution, the deformed and annealed microstructure, the precipitate evolution, or other fundamental aspects.

In summary, the production of high volume Al-Mg-Sc-Zr material requires rapid solidification if the entire Sc-content should be used for precipitation hardening. Additive manufacturing techniques providing exceptional solidification rates are capable to dissolve large amounts of Sc but are not suitable to produce precursor material for sheet metal parts. Strip casting, or similar processes, are promising candidates to produce large volume Al-Mg-Sc-Zr material. However, there exist neither fundamental studies describing the microstructure of such alloys, nor papers reporting on the metallurgical processes involved in deformation, annealing, or precipitation.

2.4.4 Open questions for alloy development

There exists a substantial amount of literature in the field of Al-Sc alloys, and a large part of which was discussed here. Most papers, however, focus on high-purity binary or ternary lab-scale alloys. Many of these studies, in fact, were carried out only to elaborate or validate mathematical models using Al-Sc as a model system. To the author's

knowledge, there are only two studies available [54,139] reporting on Al-Mg-Sc-Zr alloys produced on industrial equipment. In a paper by Filatov and coworkers [54] several Al-Mg-Sc-Zr alloys with varying chemical compositions are described. None of them reaches the desired strength level of Al-Cu-Mg alloys. A reasonable explanation is that the alloys investigated by the group were produced using conventional casting techniques. An efficient use of Sc as strengthening alloying element, however, requires direct chill casting processes with high solidification and cooling rates. As mentioned previously, there exists only one study reporting on a rapidly solidified alloy produced on strip casting equipment [139]. However, no basic microstructure characterization or details on the kinetics of precipitation or recrystallization are presented there. For example, the amount of Sc in solution after casting, one of the most essential characteristics for precipitation hardening, is not discussed. In other words, the quantitative correlation between microstructure evolution and mechanical properties is so far unknown for rapidly solidified alloys produced on industrial scale.

The most important aspects that need to be understood in order to develop a novel, rapidly solidified alloy are derived as follows:

- Amount of Sc in solution after the industrial processes.
- Precipitation hardening potential depending on the degree of Sc-supersaturation.
- Description of the Al_3(Sc,Zr) precipitation kinetics depending on the content of solute Sc.
- Microstructure evolution during deformation depending on the materials condition, temperature, strain, and strain rate.
- Softening behavior during annealing of a cold deformed alloy depending on the materials condition, ageing temperature, and degree of plastic deformation.
- Separation of the individual softening kinetics from that of precipitation hardening during annealing of cold deformed material.

3 Objectives and approach

The overall objective of this work is to analyze the behavior of a novel, rapidly solidified Al-Mg-Sc-Zr alloy during thermo-mechanical processing. This alloy was developed within the research project "OscAR" and was produced for the first time using an industry-scale belt caster. The alloy is intended to be used as a stringer material, however, the processing routine of the casted alloy is so far unknown. In any case, the casted belt has to be rolled to sheet metal condition in order to finally produce a stringer by roll forming. The processing of the alloy should be directed towards achieving high strength in the final product while having enough formability during materials processing.

The first objective of this study is to characterize the belt-casted material with regard to the microstructure, mechanical properties, and the amount of Sc in solution. In a second step, an alternative materials condition is produced using an electron beam process with highest solidification and cooling rates. The intention of this procedure is to achieve the highest possible degree of Sc-supersaturation and compare the materials properties to the as-cast material as a benchmark.

Based on the basic characterization, the second main objective is to systematically evaluate the materials behavior during different age hardening treatments of non-deformed material. This includes the hardening potential as a function of Sc-content in solution, temperature, and time, as well as a quantitative description of the precipitation kinetics. The mechanical properties need to be correlated to the microstructure evolution, in particular, to the strengthening Sc- and Zr-containing phases.

The third main objective is to analyze and describe the concurrent phenomena of hardening and softening occurring during annealing of a deformed Al-Mg-Sc-Zr alloy. It is aimed to separate the kinetics of precipitation hardening and softening due to recovery or recrystallization to quantitatively describe each phenomenon. Again, the microstructure evolution during ageing of deformed material needs to be correlated to the mechanical properties as a function of temperature, time, and degree of deformation.

4 Experimental

In this work, several aspects of a novel belt-casted Al-Mg-Sc-Zr alloy developed in the project "OscAR" were studied. In a first step, the belt-casted material was analyzed with respect to the presence of primary, eutectic, and secondary Al_3(Sc,Zr) phases to determine the content of Sc in solution. Parts of the material were re-melted and solidified with highest solidification and cooling rates using an electron beam process to study an additional materials condition with highest solute Sc-concentration. Thereafter, the Al_3(Sc,Zr) precipitation kinetics was studied for both materials conditions, i.e. as a function of the degree of Sc-supersaturation, temperature, and time. Finally, cold deformed samples were subjected to various investigations to separate the kinetics of precipitation hardening and softening due to recovery or recrystallization. In-situ methods were used to precisely study the temporal evolution of the processes.

4.1 Material

The investigated material was an Al-alloy with a nominal chemical compostition of 4 wt.% Mg, 0.4 wt.% Sc, and 0.12 wt.% Zr casted to an 8 mm thick, 280 mm wide, and 30 m long belt using a continuous belt-casting technology. The chemical composition is shown in Table 4.1. Three different materials conditions were studied in this work: as-cast (AC), pre-aged (PA), and electron-beam re-solidified (EBRS).

4.1.1 As-cast condition

For the given casting conditions, the solidification and cooling rates were estimated by the materials producer with around 30 Ks^{-1}. These rates are medium-high compared to different Al-casting processes ranging from 10^{-1} to 10^{2} Ks^{-1} [140].

Table 4.1: Chemical composition of the belt-casted Al-Mg-Sc-Zr alloy (wt.%)

Alloy	Al	Mg	Sc	Zr	Fe	Si	Cu	Mn	Zn	others
AlMg4Sc0.4Zr0.12	bal.	3.89	0.37	0.13	0.04	0.05	0.002	0.02	0.04	0.007

4.1.2 Pre-aged condition

A small portion of the as-cast (AC) material was aged at 325°C to promote the formation of Al_3(Sc,Zr) precipitates prior to further processing. This materials condition was called pre-aged (PA). The samples were inserted in a heated furnace and aged for 60 min.

4.1.3 Electron-beam re-solidified condition

Parts of the as-cast (AC) material were remelted and solidified using an electron-beam re-solidification (EBRS) process. The objective of this procedure was to generate an alloy subjected to a very high solidification rate of up to $10^5\,\mathrm{Ks}^{-1}$ [141]. EBRS was performed using an EBG 45-150 K14 electron beam welding machine (pro-beam). The main processing parameters were an acceleration voltage of 150 kV, a beam current of 10 mA, and a processing speed of $10\,\mathrm{mms}^{-1}$. The focus of the electron beam was set slightly below the surface of the casted belt to avoid pores in the re-solidified material.

4.2 Methods

Several methods and procedures were used to modify the conditions of sample material and test the resulting mechanical properties. The property modifying methods included cold deformation and various heat treatments. The material's response to these treatments was measured by hardness testing.

4.2.1 Plane-strain deformation

Specimens of AC and PA material were compressed at room temperature in plane-strain condition using a Gleeble® 3800 Hydrawedge system (DSI). Plane-strain deformation was used to simulate an industrial rolling process [142]. The deformation procedure is schematically illustrated in Fig. 4.1 (a) and (b). The 20 mm long, 10 mm wide, and 4 mm thick specimens were machined from the center of the casted belt and compressed to final equivalent strains of 0.5 and 1.5 with a strain rate of $1\,\mathrm{s}^{-1}$. For all microstructure images of deformed samples, deformation occurred in vertical direction.

4.2.2 Heat treatments

Two different kinds of heat treatment procedures were used depending on the desired heating rate and temperature cycle. Furnace annealing was used for slow heating rates, while dilatometer annealing was carried out for higher heating rates, as follows.

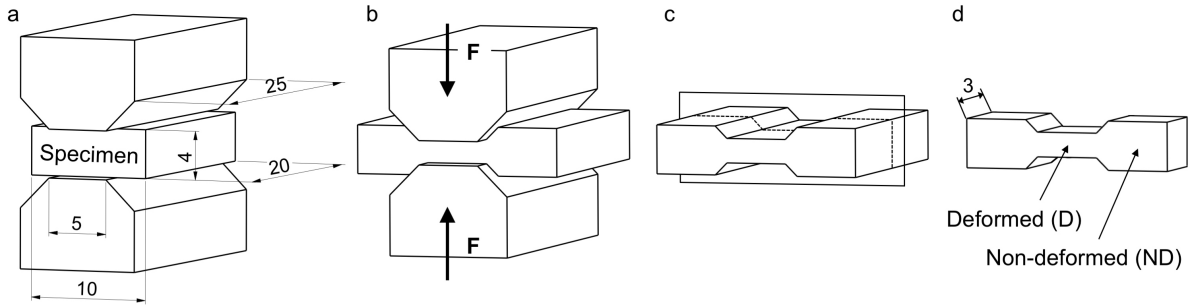

Fig. 4.1: Specimen and anvils before (a) and after (b) plane strain deformation in a Gleeble® 3800 Hydrawedge system (dimensions in mm). Deformed specimen and cutting plane to machine dilatometer samples (c). Dilatometer samples with a thickness of 3 mm indicating deformed (D) and non-deformed (ND) sample positions (d).

4.2.2.1 Furnace annealing

Samples in non-deformed AC and EBRS conditions were heated in a furnace to 250°C, 325°C, and 400°C with a heating rate of $1\,°Cs^{-1}$. A total of 12 samples per condition was aged at each temperature to study the $Al_3(Sc,Zr)$ precipitation kinetics. The individual samples were annealed in the furnace for different durations ranging from 0.1 to 180 min prior to air cooling. Finally, the hardness was measured in every sample after the ageing treatment.

4.2.2.2 Dilatometer annealing

Dilatometer annealing was performed for AC and PA samples after cold deformation to equivalent strains of 0.5 and 1.5 to study the recrystallization behavior of the material. Individual samples with a thickness of around 3 mm were cut out of the deformed specimens, as shown in Fig. 4.1 (c) and (d). Consequently, the dilatometer samples revealed a distinct heterogeneity with a deformed center (D) and non-deformed (ND) edges (Fig. 4.1 d). These samples were annealed in a DIL 805A/D dilatometer (Baehr). They were mounted between rods made of quartz and were held with a force just large enough to prevent the loss of the samples. Thus, the thermal expansion was not inhibited. A K-type thermocouple was welded on the surface of each sample to control the temperature.

Table 4.2 gives an overview of the dilatometer annealing experiments including the initial plastic strain, the ageing temperatures and times, as well as the total amount of samples used per materials condition. The heat treatments were carried out at 325°C, 400°C, and 500°C for the AC condition, while in case of PA condition annealing was done at 400°C only. The controlled heat-up occurred within 1 min from room temperature to the

Table 4.2: Overview of the dilatometer annealing experiments and total number of samples used per materials conditions.

	Strain ( )	Temperature (°C)	Time (min)	Samples
As-cast (AC)	0.5 and 1.5	325 and 400 and 500	0.1 to 60	84
Pre-aged (PA)	0.5 and 1.5	- and 400 and -	0.1 to 60	28

respective target temperature by induction heating. This corresponds to heating rates between 5 and 8°Cs^{-1}. A total of 14 samples was annealed per temperature and strain with ageing times ranging from 0.1 to 60 min. More specific, the ageing times were 0.1, 0.5, 1, 2, 3, 4, 5, 7, 10, 15, 20, 30, 45, and 60 min. After annealing, the samples were cooled down to room temperature in a He-gas flow within seconds. The hardness was measured in every sample after dilatometer annealing.

4.2.3 Hardness testing

Hardness testing was done to study and compare the mechanical properties in various sample conditions, and after different processing routes and thermo-mechanical treatments. The used hardness measurement method was HV0.1 Vickers hardness with a load of 0.981 N. An automatic M1C010 hardness tester (EMCO-TEST) was used. A minimum of 15 individual measurements was carried out per sample condition in order to ensure statistical significance.

4.3 Microstructure analyses

A large variety of techniques was used to study the microstructure in different materials conditions. In-situ investigation methods were carried out to study the temporal evolution of time and temperature dependent phenomena. Several scanning and transmission electron microscopy techniques were used to characterize micro- and nanostructures to finally correlate the findings to the in-situ investigations.

Some microscopy figures consist of several subfigures. If the scale is the same for all subfigures of a figure, the length of the scale bar on the right bottom subfigure applies to all other subfigures.

4.3.1 In-situ synchrotron X-ray diffraction

Diffraction occurs when a wave encounters regularly spaced objects with spacings comparable to the wavelength. Diffraction measurements in crystals, in general, are based on Bragg's law [143,144]:

$$n\lambda = 2d \cdot \sin\Theta. \tag{4.1}$$

In Eq. 4.1, n is the order of reflection (usually 1), λ is the wavelength of the incident beam, d is the interplanar spacing, and Θ represents the scattering angle. This relationship, schematically shown in Fig. 4.2, determines that constructive interference occurs at an angle Θ only if the path length difference between the deflected rays $1'$ and $2'$ equals a whole number of wavelengths λ. X-ray diffraction (XRD) measurements are commonly used to determine the crystal structure or the interplanar spacing of a crystalline material, or for phase identification in alloys. In the latter case, the interplanar spacings of various lattice planes of the respective phases need to be known in order to identify the measured signals. The majority of XRD measurements is carried out ex-situ, i.e. the materials condition does not change during the measurement. In that case, laboratory XRD measurement devices with acquisition times in the range of hours can be used. If fast transformations should be studied in-situ, on the other hand, the signal acquisition time in laboratory devices is too long as a result of a lack of brilliance of the X-ray beam. To study the precipitation kinetics at elevated temperature, for example, a highly brilliant Synchrotron X-ray beam needs to be used. For further information on Synchrotron light sources and their application in materials science, the reader is referred to [145,146].

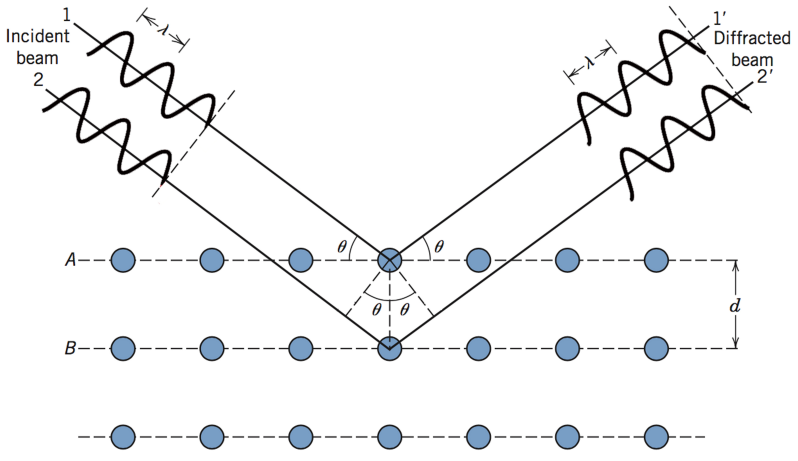

Fig. 4.2: Diffraction of X-rays by planes of atoms, where constructive interference occurs only if Bragg's law is satisfied [13].

To analyze the presence, formation or dissolution of different phases during annealing, in-situ synchrotron X-ray diffraction (XRD) measurements were carried out at the Austrian SAXS beamline at Elettra Sincrotrone Trieste [147]. The beamline was set-up to use monochromatic X-rays with a wavelength of 0.154 nm. X-ray patterns were recorded with a Pilatus 100k pixel detector (Dectris). The angular scale of the patterns spanned the range between 30° and 53° and was calibrated with LaB_6 powder. AC and EBRS specimens were cut to 70 to 100 µm thick samples which were placed in a custom made sample support for transmission measurements mounted on a DHS 1100 heating stage (Anton Paar). This arrangement allowed to capture XRD patterns every 10 seconds while subjecting the samples to a heat treatment. For both AC and EBRS samples, the same temperature cycle as for the furnace annealing at 400°C was carried out, i.e. a heat-up stage with a heating rate of $1°Cs^{-1}$ followed by isothermal ageing for 180 min and air cooling. The temperature during the heat treatment was measured using a K-type thermocouple mounted on the heating stage. To evaluate the intensity of the XRD peaks, the Al_3(Sc,Zr) peak height was determined by fitting a Lorentzian peak with a linear background to the data for the given time step.

4.3.2 In-situ confocal laser scanning microscopy

Confocal laser scanning microscopy (CLSM) is a technique primarily used for high-resolution imaging of molecules in biomedical sciences [148]. In addition, in-situ CLSM was successfully applied to study various temperature dependent microstructural phenomena in metals. These include both solid-liquid [149–151] and solid-solid [152–156] phase transformations. The latter investigations show the suitability of CLSM to observe the formation and migration of boundaries.

In-situ CLSM was never used to study the recrystallization behavior of alloys. However, in this work it was considered as a very suitable approach due to its capability to visualize boundary migrations and to determine the local and temporal evolution of these transformations. CLSM was carried out using a 1LM15 (Lasertec) microscope to study the recrystallization behavior of AC and PA samples in-situ during annealing after cold deformation. The samples were prepared as follows: First, plane strain compression to final equivalent strains of 0.5 and 1.5 was carried out, as explained in 4.2.1. Second, specimens were prepared in the same way as for dilatometer annealing (Fig. 4.1 d). The final sample preparation step is illustrated in Fig. 4.3 (a). CLSM samples with a width of 3 mm were cut out of the center of the deformed specimens and polished manually. The centers of the small samples were investigated by in-situ CLSM and electron backscat-

ter diffraction (EBSD). Fig. 4.3 (b) shows the simulated strain distribution in a sample that was cold deformed to a total equivalent strain of 0.8 under plane strain condition. Despite the heterogeneous strain distribution typical for the process [157–159], it can be observed that the strain in the center of the sample corresponds roughly to the global strain of the sample. It was, therefore, assumed that the strain in the centers of the samples deformed to 0.5 and 1.5 strain also corresponded to the respective global strain.

The annealing treatments in the CLSM were done analogous to those in the dilatometer. Heat treatments were carried out inside the CLSM at 325°C, 400°C, and 500°C for the AC condition, and at 400°C in case of PA condition. The samples were heated by infrared rays within 1 min in an Ar-3%H_2 atmosphere, held for 60 min at the target temperature, and subsequently cooled down to room temperature. During annealing, an area of 300 x 220 µm was scanned at a rate of 30 frames per second while an image was captured every second.

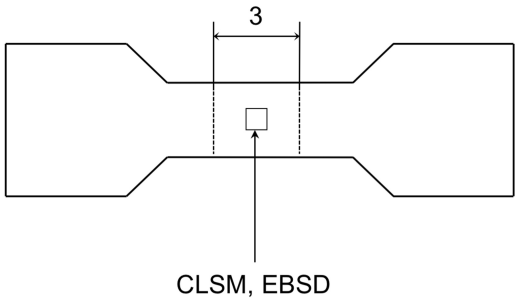

(a) Schematic illustration of a 3 mm wide CLSM sample cut out of a deformed specimen. Sample center investigated by CLSM and EBSD.

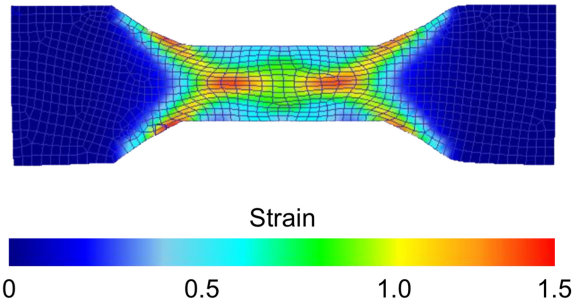

(b) Simulation of the strain distribution in a sample cold deformed to a final equivalent strain of 0.8 (Courtesy of Martina Dikovits)

Fig. 4.3: Illustration of a 3 mm wide sample used for annealing in a CLSM (a). The center of the sample was investigated by in-situ CLSM and electron backscatter diffraction (EBSD). Simulation of the strain distribution in a sample after cold deformation under plane strain condition to a total equivalent strain of 0.8 (b). Despite the heterogeneous distribution, the center of the sample revealed a strain of 0.8, identical to the global deformation of the sample.

4.3.3 Scanning electron microscopy

Scanning electron microscopy (SEM) is used to image and analyze bulk specimens. Electrons are accelerated through a voltage difference towards the specimen where they interact with the sample volume. These interactions can be measured with appropriate detectors. The most important signals in metals and alloys are detected from secondary electrons (SE), backscattered electrons (BSE), Auger electrons (AE), and X-rays [160].

4.3.3.1 Electron backscatter diffraction

Electron backscatter diffraction (EBSD) is a technique that is universally used for characterizing the local crystallography of materials. As an add-on package to SEM, EBSD gives information about the phase structure, grain structure, local misorientation, texture, and other aspects of bulk specimens [161].

In this work, EBSD measurements were carried out mainly to study the local misorientation of the AC and PA samples before and after the CLSM procedure. To acquire proper data, the thin oxide layer that formed on the sample surface during the CLSM procedure was removed by Ar-etching for 300 s prior to analyzing the samples. A JSM7001F (JEOL) field-emission SEM was used at an acceleration voltage of 15 kV with a step size of 0.25 µm. Boundaries with misorientation greater than 12° were defined as high angle grain boundaries (HAGB) while those having lower misorientations were considered as low angle grain boundaries (LAGB). Areas with a confidence index (CI) lower 0.1 after normalization were colored in black.

Recrystallized grains were distinguished from deformed or recovered ones by calculating grain orientation spread (GOS) maps. The grain orientation spread is the average deviation in orientation between each point in a grain and the average orientation of the grain and is a useful technique to identify recrystallized grains [162]. In this work, the GOS limit for recrystallized grains was set to 1.5°, i.e. the difference in orientation between each point in a recrystallized grain and the average orientation of this particular grain was less than 1.5°, similar to [163].

To compare the microstructure obtained on the surface of CLSM samples with that inside the bulk, a 100 µm thick layer was removed by Ar-ion milling after analyzing the surface. This procedure was done only for the AC samples annealed at 400°C in the CLSM. The bulk microstructure was analyzed using the same EBSD procedure as explained above.

4.3.3.2 Energy-dispersive X-ray spectroscopy

Energy-dispersive X-ray spectroscopy (EDS) is capable to give element-sensitive images of a SEM-sample. When the electron beam interacts with a sample volume, X-rays are emitted with element-specific energy, thus identifying the local chemical composition. EDS measurements were carried out using a LEO 1450VP (ZEISS) scanning electron microscope.

In this work, EDS was used to identify microstructural features in micrometer range regarding their chemical composition. In particular, Sc- and Zr-rich phases in non-deformed condition as well as in recrystallized material were investigated. The identification of recrystallized grains was based primarily on the EBSD data, as explained above. However, Al_3(Sc,Zr) have the same lattice structure as α-Al which allows no differentiation based on EBSD data. Therefore, the results of the GOS analysis were further refined using EDS maps of Sc to allow a differentation between recrystallized grains and large Al_3(Sc,Zr) phases.

4.3.4 Transmission electron microscopy

Unlike SEM characterization, where bulk samples are studied, transmission electron microscopy (TEM) uses thin foil samples that are transmitted by an electron beam causing various interactions with the sample volume. The resolution of a modern TEM may reach to the range of a single atom depending on the instrumentation, the mode of operation, the sample condition, and other factors [164]. Consequently, TEM is a suitable technique to study precipitates in the nanometer range, such as Al_3(Sc,Zr) precipitates.

The preparation of TEM samples included the following steps: A thin foil with a thickness of about 500 µm and a diameter of 3 mm was cut from the bulk sample using a diamond wire saw and an ultrasonic disk cutter. After dimpling and polishing the sample, an Ar-ion milling step under 4 kV at an angle of 4° at the top and 6° at the bottom was carried out until a hole with electron transparent edges appeared. The investigations were carried out at specimen thicknesses of about 0.5 times the inelastic mean free path.

4.3.4.1 High-resolution scanning TEM

High-resolution scanning TEM (HR-STEM) provides atomic resolution by scanning a convergent beam along very small specimen areas. Investigations were carried out on a Cs-probe corrected Titan^3 $60-300$ kV (FEI) equipped with a Super-X EDX detector (FEI) and a GIF Quantum energy filter (Gatan), operated at 300 kV. High-angle annular

dark-field (HAADF) images were acquired showing the heavier Sc and Zr brighter than the Al matrix. To verify whether the elements in question were present, simultaneous X-ray and electron energy-loss spectroscopy (EELS) acquisitions were performed.

In this work, HR-STEM was carried out to study the presence and nature of Al_3(Sc,Zr) precipitates in AC and EBRS conditions after the in-situ XRD measurements.

4.3.4.2 Energy-filtered TEM

Energy-filtered TEM (EFTEM) is capable of acquiring filtered images with optimized contrast at a resolution in nanometer range. A Tecnai F20 (FEI) operated at 200 kV equipped with a Tridiem post column imaging filter (Gatan) was used to study the precipitate structure of AC and EBRS samples after 180 min of ageing at 325°C and 400°C. The samples annealed at 250°C could not be analyzed quantitatively due to the very small precipitate size.

The filtering energy was set such to deliver highest contrast between Al_3(Sc,Zr) precipitates and matrix. This was reached at an energy of 40 eV with a slit width of 10 eV, generating bright precipitates in a dark matrix. Using this light-dark contrast, the precipitates could be identified in order to quantify the precipitate radius, volume fraction, and number density for the different sample conditions. For identification of the precipitates and analysis of the sample thickness, the software DigitalMicrograph (Gatan) was used. The precipitate radius was calculated from the images assuming spherical particles. Based on the radius of every single precipitate, the total precipitate volume was calculated for every individual measurement. The corresponding total measurement volume was calculated from the sample thickness and the measuring area. The ratio of precipitate volume and total measurement volume was used to determine the precipitate volume fraction for every measurement. The precipitate number density was finally evaluated by dividing the number of precipitates by the respective measuring volume.

EFTEM measurements were also used to study the interactions of precipitates and high-angle grain boundaries in recrystallized material. An AC sample was analyzed that was deformed to 0.5 strain and annealed at 400°C for 1 h in a CLSM. In that case, the characterization was carried out on a Cs-probe corrected Titan^3 $60-300$ kV (FEI) operated at 300 kV using a GIF Quantum energy filter (Gatan).

4.4 Experimental summary

Fig. 4.4 summarizes all experimental investigations. The hardness evolutions of AC and EBRS material due to furnace annealing were combined with in-situ XRD as well as HR-STEM and EFTEM investigations to study the $Al_3(Sc,Zr)$ precipitation kinetics. Cold deformed AC and PA samples were subjected to dilatometer annealing followed by hardness measurements, on the one hand, and in-situ CLSM as well as EBSD, EDS, and EFTEM investigations, on the other hand, to investigate the kinetics of recrystallization.

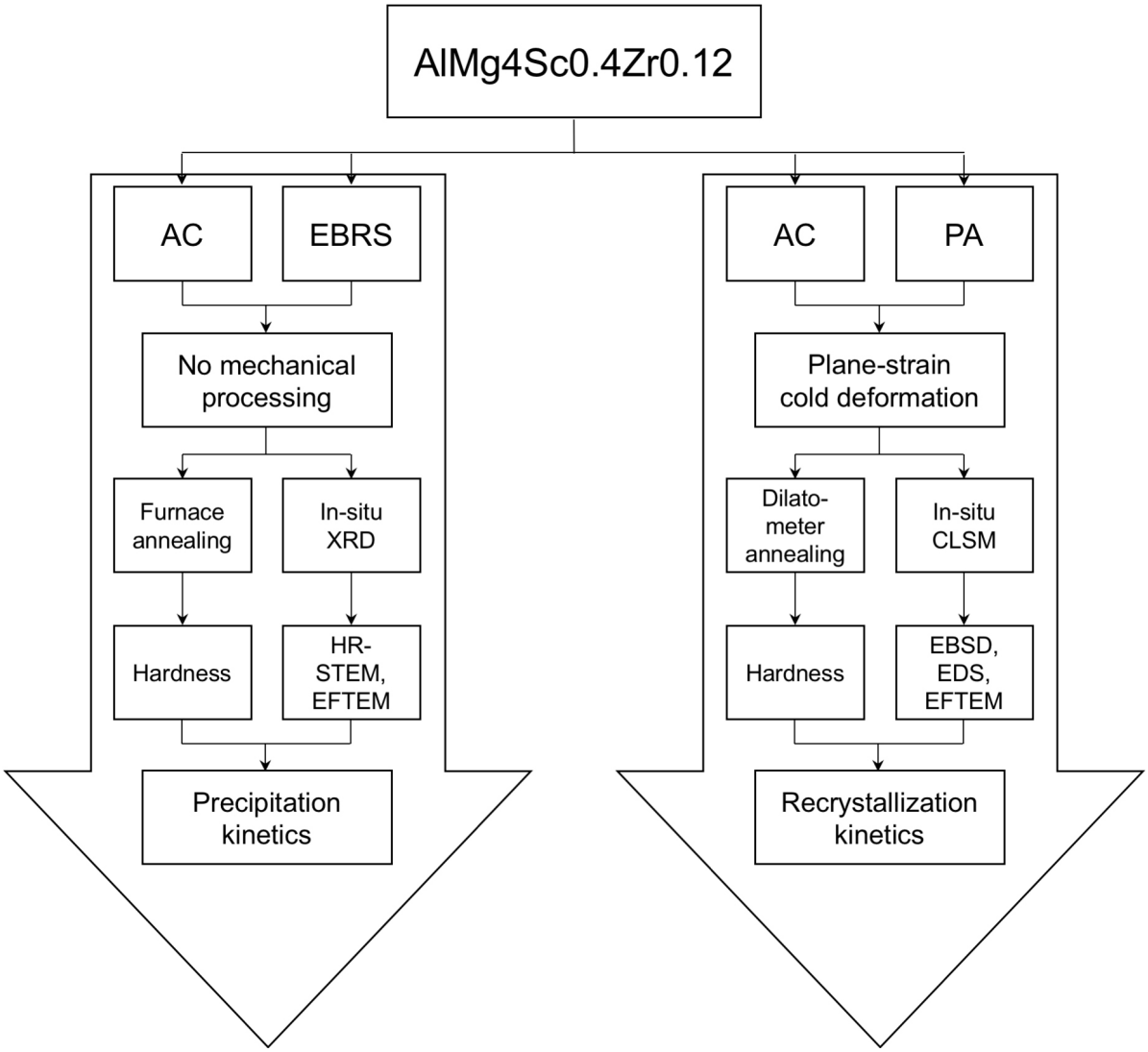

Fig. 4.4: Summary of materials conditions and experimental methods used to determine the precipitation and recrystallization kinetics of the belt-casted AlMg4Sc0.4Zr0.12 alloy.

5 Results and analyses

This section shows the results obtained in this work and is subdivided into three main parts. The first one shows the characterization of the material in AC, PA and EBRS conditions. The second part deals with the precipitation kinetics in different sample conditions, while the third part is related to the kinetics of softening, in particular recrystallization.

5.1 Materials characterization

The three different initial sample conditions as-cast (AC), electron-beam re-solidified (EBRS), and pre-aged (PA) were analyzed regarding grain structure, hardness, presence and nature of Al_3(Sc,Zr) phases, and degree of Sc-supersaturation. The grain structure in AC condition was equiaxed rather than columnar with an average grain size of around 30 µm, as shown in the electron-backscatter diffraction (EBSD) image in Fig. 5.1 (a). The samples in AC condition revealed a hardness value of 66 ± 2.5HV0.1. The grain size and morphology in PA condition was very similar to that in AC, however, the hardness in case of PA condition was considerably higher with values of 94 ± 3.2HV0.1. This hardness increase was attributed to the presence of secondary Al_3(Sc,Zr) precipitates that formed during pre-ageing at 325°C for 60 min, as discussed in detail in the following sections. The grain size for PA condition was similar to that of AC material and was not investigated quantitatively.

The grain size in EBRS condition was significantly smaller than for AC and PA with around 5 µm, as demonstrated in Fig 5.1 (b). This reduction in grain size resulted from the exceptionally high solidification rates associated with the EBRS process. The EBRS samples revealed a hardness of 65 ± 2.8HV0.1. The considerable reduction in grain size compared to AC condition (Fig. 5.1) had no influence on the hardness. The values for grain size and hardness investigations are summarized in Table 5.1.

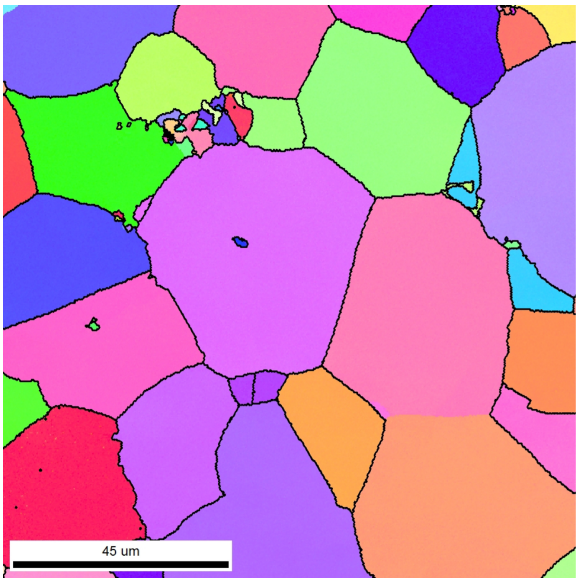

(a) As-cast (AC)

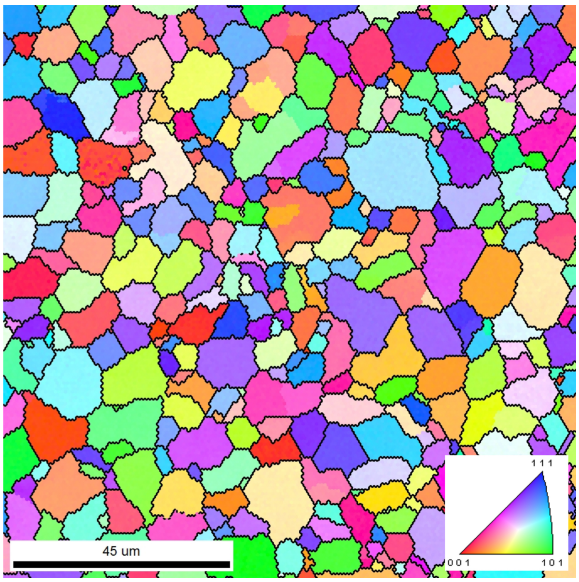

(b) Electron-beam re-solidified (EBRS)

Fig. 5.1: EBSD orientation maps of as-cast (a) and electron-beam re-solidfied (b) material revealing significant differences in grain size due to different solidification rates. (HAGB in black, colours correspond to crystal orientation according to reference triangle.)

Table 5.1: Summary of hardness and grain size for different initial sample conditions. The grain size in PA condition was similar to AC material and was not analyzed in detail.

Condition	Hardness (HV0.1)	Grain size (µm)
AC	66 ± 2.5	30 ± 6
PA	94 ± 3.2	-
EBRS	65 ± 2.8	5 ± 2

Fig. 5.2 shows non-etched light-optical microscopy (LOM) images of AC (a), PA (b), and EBRS (c) samples. In all images, dark gray microstructural features highlighted with arrows were detected. In case of AC and PA conditions, a large amount of these features was present with similar distribution, either as individual regular shapes (black arrows) or as clusters of smaller entities (white arrows). In case of EBRS condition, on the other hand, the number of those features was significantly reduced, as shown in Fig. 5.2 (c). During the EBRS process, most of these microstructural entities were dissolved and their formation was supressed due to the high solidification rates.

The features highlighted in Fig. 5.2 were further investigated using SEM and EDS techniques. The results of these analyses on AC samples are shown in Figs. 5.3 and 5.4.

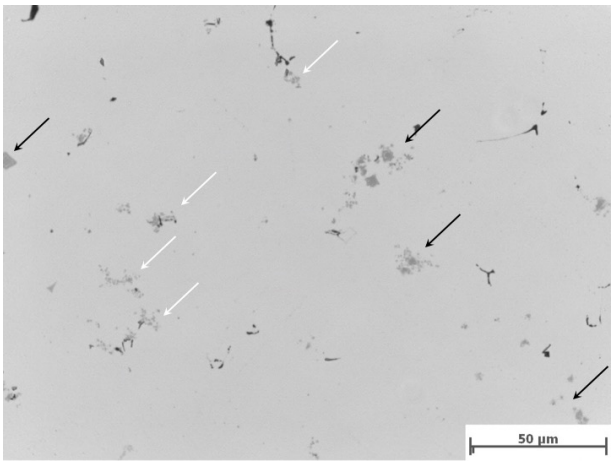

(a) As-cast (AC) condition

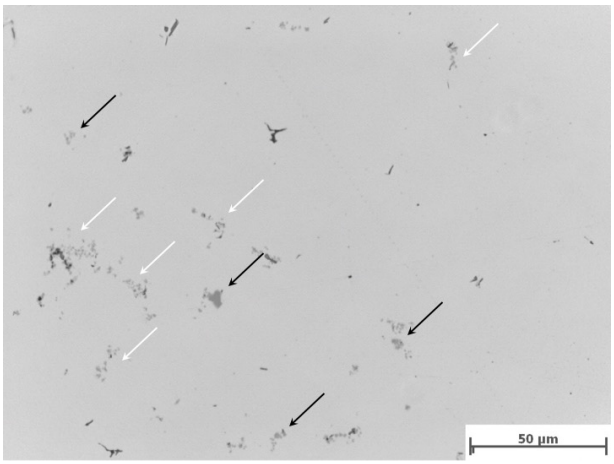

(b) Pre-aged (PA) condition

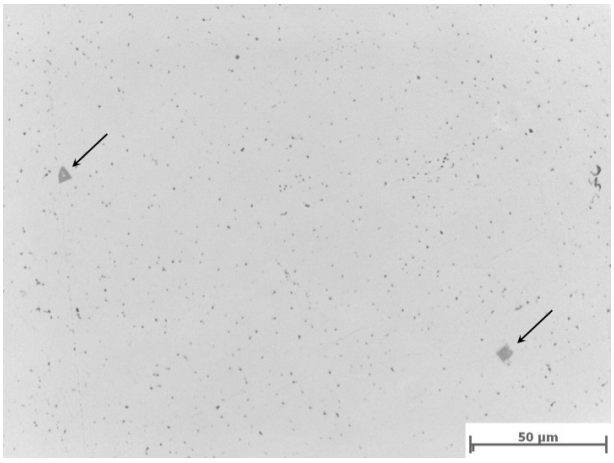

(c) Electron-beam re-solidified (EBRS) condition

Fig. 5.2: LOM images of AC (a), PA (b), and EBRS (c) conditions. Black arrows indicate individual features with regular shape, white arrows indicate features in clusters.

Fig. 5.3 (a) shows a SEM image taken from one of the regular shaped entities indicated with black arrows in Fig. 5.2. The phase with a size of roughly 20 µm was found to be rich in Sc and Zr using EDS analysis (Fig 5.3 b). From the chemical composition and the regular shape, the phase was identified as primary Al_3(Sc,Zr). This primary phase was located in the center of an α-Al grain with grain boundaries enriched in Mg. In good agreement with previous studies [78,80], it is shown from Fig. 5.3 that the primary Al_3(Sc,Zr) phase served as nucleation site for the α-Al grain that grew in all directions while segregating the lower melting Mg-rich liquid phase.

Similar SEM and EDS analyses were carried out for the clusters highlighted with white arrows in Fig. 5.2, as shown in Fig. 5.4. Again, the phases were identified as Sc- and Zr-rich. However, in contrast to the large primary phase shown in Fig. 5.3, the phases were smaller, less regular in shape, and located at α-Al grain boundaries rather than the grain centers. It is assumed that these Al_3(Sc,Zr) phases represent primary phases with less regular shape as a result of rapid solidification [78] and eutectic α-Al+Al_3(Sc,Zr).

The main target of the characterization of the initial conditions was the quantification of the Sc-content in solution that might contribute to precipitation strengthening in a further age hardening process. Two different approaches were followed to study the degree of Sc-supersaturation in AC and EBRS conditions. In PA condition, the content of solute Sc was assumed to be negligible, i.e. close to 0, as a result of progressed Al_3(Sc,Zr) precipitation during pre-ageing at 325°C for 60 min. Arguments supporting this assumption are discussed in section 6.2.

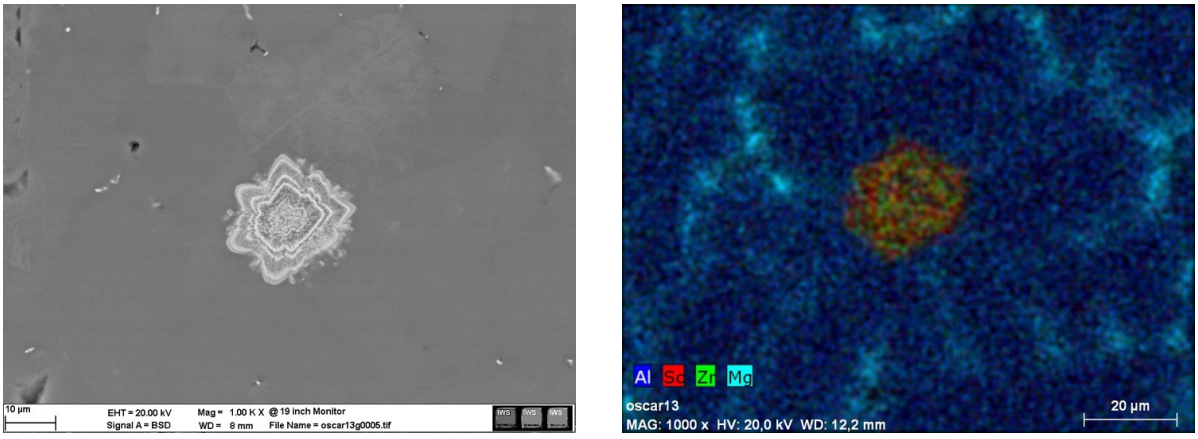

(a) SEM image (b) EDS map

Fig. 5.3: SEM (a) and EDS (b) images showing a large primary Al_3(Sc,Zr) phase located in the center of an Al-grain with Mg-segregations at the grain boundaries.

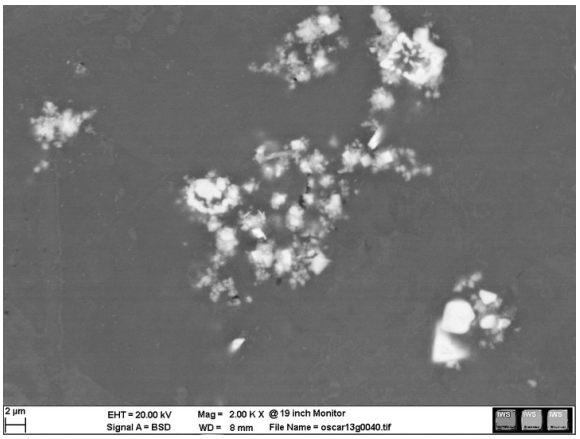

(a) SEM image

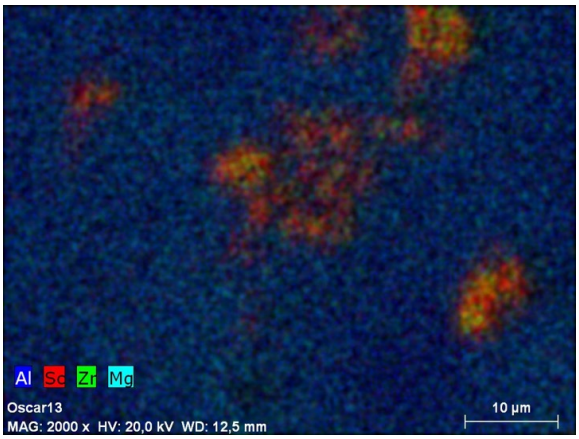

(b) EDS map

Fig. 5.4: SEM (a) and EDS (b) images showing clusters of primary or eutectic $Al_3(Sc,Zr)$.

The first approach to study the degree of Sc supersaturation was a simple image analysis based on the LOM images shown in Fig. 5.2. The estimation neglecting the presence of Zr and Mg was conducted as follows: First, the area fraction of $Al_3(Sc,Zr)$ was determined for AC and EBRS samples by analyzing the LOM images in Fig. 5.2. Using a graphical analysis tool (ZEISS KS400), the area fractions were quantified based on the contrast between the light matrix and the darker $Al_3(Sc,Zr)$ phases. It was assumed that the area fractions corresponded to the volume fractions. From the area or volume fractions, the $Al_3(Sc,Zr)$ weight fractions were calculated by taking into account the different weights of the unit cells of α-Al (107.928 u) and $Al_3(Sc,Zr)$ (125.902 u). The conversion factor between $Al_3(Sc,Zr)$ volume fraction and weight fraction equalled 1.167. The weight fraction was used to determine the amount of Sc that was bound in $Al_3(Sc,Zr)$ phases. The estimation of the Sc-content in $Al_3(Sc,Zr)$ phases was based on a binary Al-Sc phase diagram (Fig. 2.13) where the α-Al+Al_3Sc phase field ranged from 0 to 35.7 wt.% Sc at room temperature. Finally, the content of solute Sc was determined as the difference between the nominal Sc-content (0.4 wt.%) and the content of Sc bound in $Al_3(Sc,Zr)$ phases. The individual values of this graphical estimation are shown in Table 5.2. The amount of Sc in solution was quantified with 0.12 wt.% in AC condition and 0.39 wt.% in EBRS condition.

The second approach to analyze the content of solute Sc was based on quantitative HR-TEM EDS measurements of the precipitate-free matrix in AC and EBRS samples. These analyses revealed degrees of Sc-supersaturation of 0.15 wt.% in AC condition and 0.35 wt.% in EBRS condition. The average values of the two investigation approaches,

graphical analysis and HR-TEM, were used for further analyses in this work. A summary of the values aquired with the two approaches as well as the average values are given in Table 5.3. For further investigations, the average values of the two analyses were used equalling 0.13 ± 0.02 wt.% in AC and 0.37 ± 0.03 wt.% in EBRS conditions.

Table 5.2: Estimation of solute Sc-content in different materials conditions: Al_3(Sc,Zr) area (volume) fraction and weight fraction based on graphical analysis of micrographs, Sc content in Al_3(Sc,Zr) and solid solution calculated from Al-Sc phase diagram.

	Al_3(Sc,Zr) proportion (%)		Sc (wt.%) proportion in	
Condition	Area/Volume	Weight	Al_3(Sc,Zr)	Solid sol.
AC	0.674	0.786	0.281	0.119
EBRS	0.022	0.026	0.009	0.391

Table 5.3: Nominal Sc content and degree of Sc-supersaturation in different sample conditions derived from image analysis and HR-TEM EDS measurements (wt.%).

	Sc content	Sc in solid solution			
Condition	nominal	Image	HR-TEM	Average	Std. dev.
AC	0.4	0.12	0.15	0.13	0.02
EBRS	0.4	0.39	0.35	0.37	0.03

5.2 Precipitation kinetics

The precipitation kinetics of samples in AC and EBRS conditions was studied focusing on the influence of the degree of scandium supersaturation prior to ageing. First, the hardness evolution was determined by hardness measurements after ageing at 250°C, 325°C, and 400°C for up to 180 min in a furnace. Second, in-situ synchrotron XRD measurements were carried out to analyze the phase transformations occurring during ageing. Third, the Al_3(Sc,Zr) precipitate state was characterized by HR-STEM and EFTEM in terms of mean radius, volume fraction, and number density.

5.2.1 Hardness evolution

Fig. 5.5 shows the hardness evolution for different degrees of Sc-supersaturation and ageing temperatures. As shown in the previous section, the hardness values for AC and EBRS conditions were almost identical prior to ageing. During the first stage of ageing,

the hardness remained at about the same level as in the initial condition for all temperatures. However, as the hardness increased, the EBRS samples showed clearly higher values than the AC samples for all temperatures with an offset of roughly 15 HV0.1. The period of time before the first hardness increase, the incubation time, depended on the ageing temperature. The incubation time decreased from 45 min at 250°C to around 2 min at 400°C, independent of the degree of Sc-supersaturation. From the shape of the curves, it could be denoted that the samples at 250°C did not reach the peak age condition within 180 min, that those annealed at 325°C showed peak ageing between 120 and 180 min, while the samples aged at 400°C presented a peak after around 20 min. After reaching the maximum hardness, the samples aged at 400°C showed a slight but continuous decrease of the average hardness values. At lower temperatures, no decrease in hardness was observed in the investigated time range. The hardness values after 180 min of furnace annealing of AC and EBRS samples are summarized in Table 5.4.

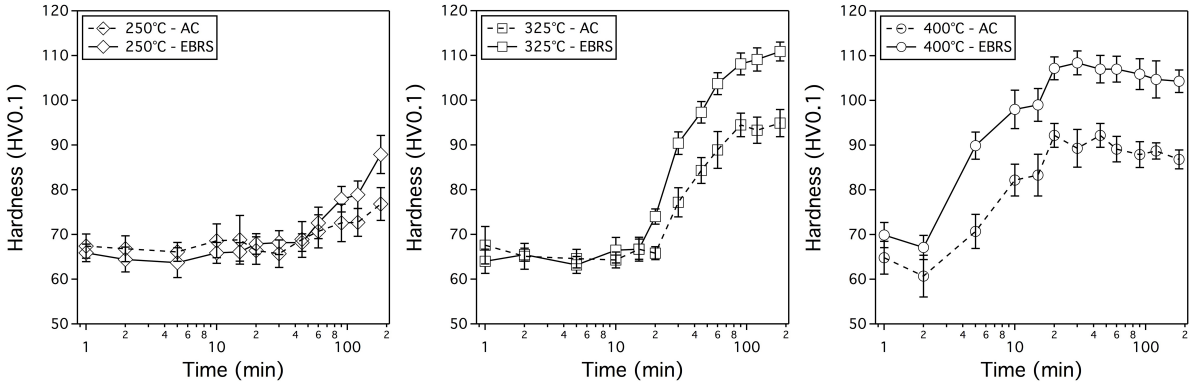

(a) Ageing at 250°C (b) Ageing at 325°C (c) Ageing at 400°C

Fig. 5.5: Hardness evolution as a function of Sc-supersaturation and ageing time at 250°C (a), 325°C (b), and 400°C (c) revealing significant influence of both the amount of Sc in solution prior to ageing as well as the ageing temperature.

Table 5.4: Hardness values after 180 min of furnace annealing of AC and EBRS samples.

	Hardness (HV0.1)	
Temperature (°C)	0.13 wt.% Sc (AC)	0.37 wt.% Sc (EBRS)
250	77 ± 3.7	88 ± 4.3
325	95 ± 3.0	111 ± 2.1
400	87 ± 2.1	104 ± 2.5

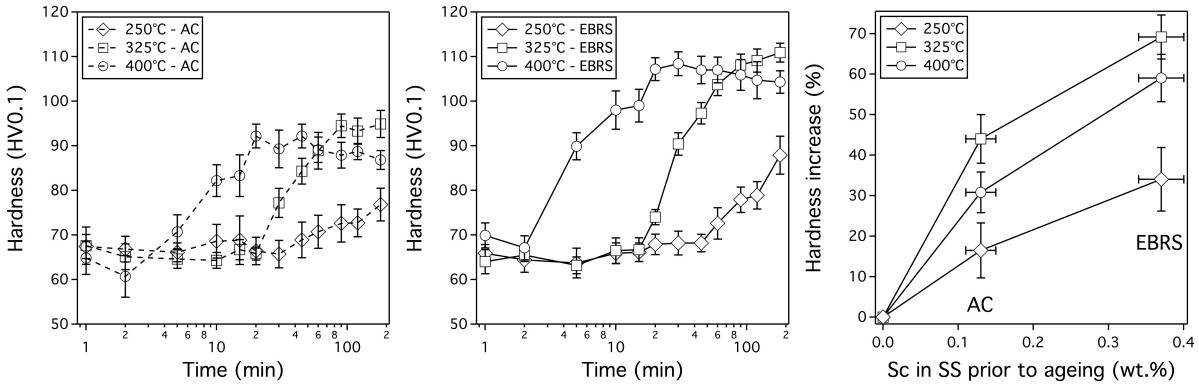

(a) 0.13 wt.% Sc (AC) (b) 0.37 wt.% Sc (EBRS) (c) Hardness increment

Fig. 5.6: Hardness evolution as a function of temperature and ageing time for 0.13 wt.% (AC) (a) and 0.37 wt.% (EBRS) (b) Sc in solution; Hardness increment after ageing for 180 min as a function of initial Sc-content in solid solution (SS) and temperature (c).

In Fig. 5.6, the hardness evolution is summarized for Sc-supersaturations of 0.13 wt.% in AC condition (a) and 0.37 wt.% in EBRS condition (b) for the investigated temperatures. A quantitative comparison of the maximal hardness achieved within 180 min of ageing as a function of Sc-supersaturation and ageing temperature is given in Fig. 5.6 (c). The maximum hardness increment of almost 70% was achieved for the EBRS sample aged at 325°C.

5.2.2 In-situ X-ray diffraction

In-situ XRD experiments were carried out during ageing at 400°C in order to characterize the evolution of the phases responsible for the observed hardness increments. The diffraction profiles in the relevant 2Θ regime are presented in Fig. 5.7 (a) for an AC and an EBRS sample aged for 0 and 180 min. The relevant peaks were identified as Al and Al_3(Sc,Zr) and are comparable to [80]. While the Al-peaks remained unchanged from the beginning to the end of the experiment, modifications of the Al_3(Sc,Zr) peak were observed, as illustrated in the close-up of this peak in Fig. 5.7 (b).

When considering Al_3(Sc,Zr) after 0 min of ageing, a small narrow peak was present in the AC sample that could not be detected in EBRS condition (Fig. 5.7 b). This observation corresponded to the fact that primary and eutectic Al_3(Sc,Zr) phases evidenced by this peak were only present in AC and not in EBRS condition. After ageing for 180 min at 400°C, the Al_3(Sc,Zr) peak in the AC sample was more pronounced, indicating the formation of further Al_3(Sc,Zr) phases. The Al_3(Sc,Zr) peak also became broader due to

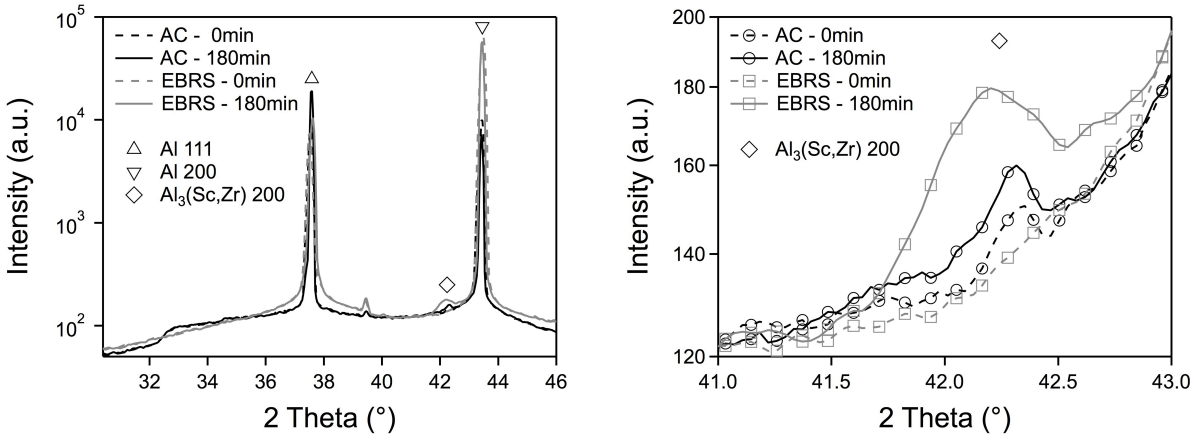

(a) Full XRD pattern

(b) Close-up of $Al_3(Sc,Zr)$ peak

Fig. 5.7: XRD profiles at 400°C after 0 and 180 min of ageing for AC and EBRS samples. The full range of relevant peaks (a) and the detailed illustration of the $Al_3(Sc,Zr)$ peak (b) demonstrate modifications of the $Al_3(Sc,Zr)$ peak over time.

the small size of the new crystallites and the elastic strain field produced by the coherent interfaces [143]. This broadening effect was even more pronounced for the EBRS sample, were a quite high but rather broad peak emerged, as shown in a more detailed temporal sequence of the $Al_3(Sc,Zr)$ peak formation in Fig. 5.8. The changing shape from flat and broad to more pronounced clearly indicates the formation and growth of precipitates.
The chronological sequence of the normalized $Al_3(Sc,Zr)$ peak intensity was correlated to the normalized hardness evolution. For both measurements, the normalization was done with respect to the maximum and minimum measured values:

$$\overline{V}_i = \frac{V_i - V_{min}}{V_{max} - V_{min}}, \tag{5.1}$$

where $\overline{V}_i$ is the normalized value of V_i, while V_{max} and V_{min} represent the maximum and minimum measured values. A slightly modified Johnson-Mehl-Avrami-Kolmogorov (JMAK) equation was used to describe the evolution of the normalized hardness and peak intensity values:

$$f(t) = Y_0 - A \cdot exp(-k\,t^n), \tag{5.2}$$

with the time t and the JMAK parameters k and n. The additional parameters Y_0 and A were introduced to account for strong oscillations in the peak intensity signal and ranged from 0.7 to 0.9. The outcome of this comparison for the AC sample aged at

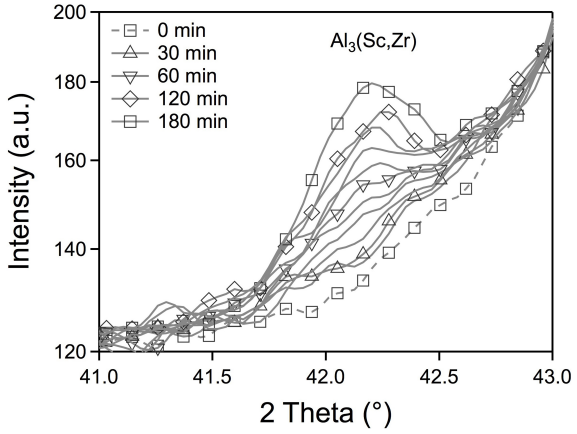

Fig. 5.8: $Al_3(Sc,Zr)$ peak of the EBRS-sample aged at 400°C showing the temporal sequence of the peak formation during ageing for 180 min.

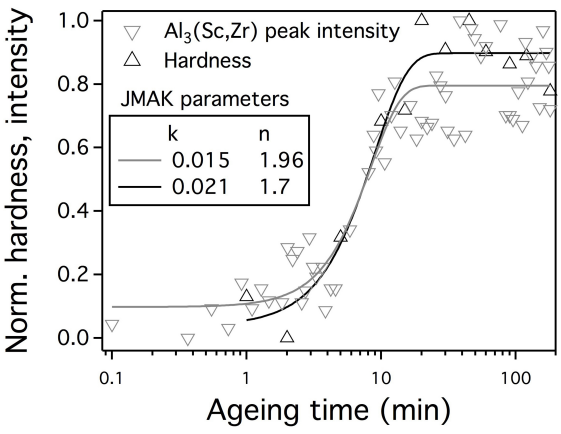

Fig. 5.9: Normalized hardness and $Al_3(Sc,Zr)$ XRD-peak intensity as a function of ageing time for the AC-sample annealed at 400°C.

400°C is shown in Fig. 5.9. The fitted curves for hardness and peak intensity showed very similar shapes, with JMAK coefficients of k=0.021 and 0.015, and of n=1.75 and 1.96, respectively. Here, the JMAK analysis was applied primarily to compare the evolutions of hardness and $Al_3(Sc,Zr)$ intensity. The parameters, however, indicate growth-dominated $Al_3(Sc,Zr)$ precipitation [9,35]. Details on the physical relevance of the JMAK parameters are discussed in 6.3.3. Since no other transformations than that of $Al_3(Sc,Zr)$ occurred and the temporal sequence of hardness and $Al_3(Sc,Zr)$ intensity correlated very well, the hardness increment upon ageing was attributed solely to the precipitation of this phase.

5.2.3 Quantitative precipitate characterization

High resolution STEM investigations were used to find and characterize the $Al_3(Sc,Zr)$ precipitates. High-angle annular dark field (HAADF) measurements presented in Fig. 5.10, as well as EELS and EDX measurements were used to identify the precipitates. Fig. 5.10 (a) gives an overview of an AC sample aged at 400°C revealing a large population of bright round particles. Electron energy loss spectra (EELS) of the particles and matrix clearly demonstrated the presence of Sc in the particles and depletion of Sc in the matrix. This consideration was not possible for Zr due to the low Zr-content and the resulting low measuring signal. Fig. 5.10 (b) shows a detailed image with highest resolution of such an $Al_3(Sc,Zr)$ particle revealing full coherency with the Al-matrix. Furthermore, the ordered $L1_2$ phase structure with alternating Al and (Sc,Zr) lattice planes could be recognized.

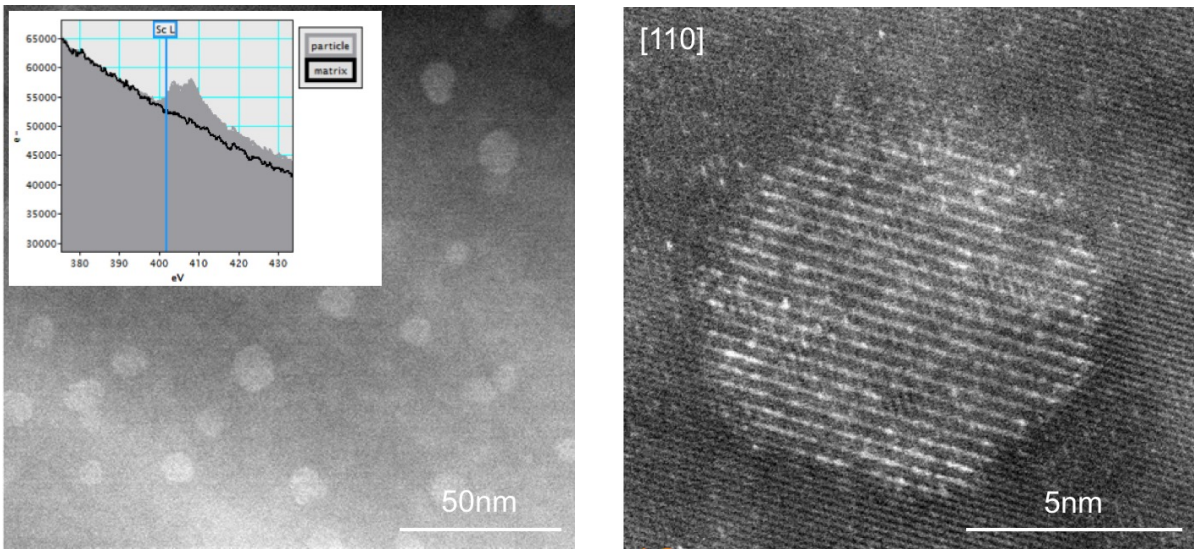

(a) Overview of several $Al_3(Sc,Zr)$ precipitates

(b) Single coherent $Al_3(Sc,Zr)$ precipitate

Fig. 5.10: HR-STEM HAADF images of precipitates in a sample aged at 400°C and EELS Sc-L-edge of particles and matrix (a) identify the observed particles as Sc-rich thus $Al_3(Sc,Zr)$. The detailed image of an $Al_3(Sc,Zr)$ precipitate (b) illustrates full coherency as well as the ordered $L1_2$ phase structure.

To quantify the precipitate population as a function of Sc-supersaturation and ageing temperature, various EFTEM images with strong element contrast were taken at several sample positions. An example of such an analysis for a sample aged at 400°C is illustrated in Fig. 5.11. The initial measurement with the bright $Al_3(Sc,Zr)$ precipitates and the dark matrix is given in Fig. 5.11 (a), the evaluation of the precipitates is shown in Fig. 5.11 (b). Based on the analysis of an average of around 450 precipitates per sample condition, the precipitate radius, $Al_3(Sc,Zr)$ volume fraction, and number density were calculated assuming spherical particles.

Fig. 5.12 illustrates the precipitate size distributions of the AC and EBRS samples aged at 325°C and 400°C for 180 min, shown as histograms of normalized counts versus precipitate radius. Independent of the degree of Sc-supersaturation, the mean radius was larger for the respective sample aged at higher temperature. The variation of the degree of Sc-supersaturation at a given temperature, however, did not influence the precipitate size distribution significantly. In case of the samples aged at 325°C for 180 min, the mean radius was 3.8 ± 2.0 nm for AC and 3.4 ± 1.8 nm for EBRS conditions. The samples aged at 400°C for 180 min showed mean radii of 5.2 ± 1.8 nm for AC and 5.1 ± 1.7 nm for EBRS conditions.

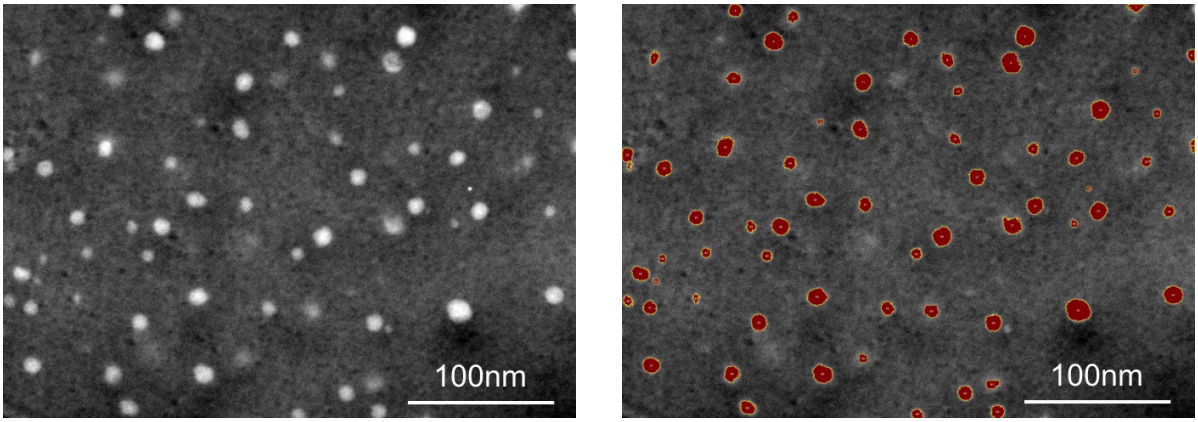

(a) Raw image as measured (b) Precipitates identified by contrast difference

Fig. 5.11: Precipitate analysis for a sample aged at 400°C: EFTEM image obtained using a 10 eV slit at an energy loss of 40 eV (a); Precipitate identification using light-dark contrast (b) to isolate the precipitates from the matrix for further calculations.

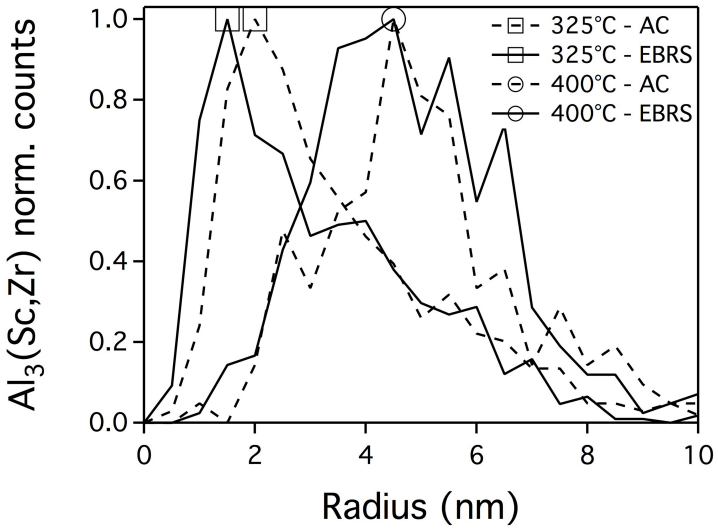

Fig. 5.12: Normalized $Al_3(Sc,Zr)$ size distribution as a function of the degree of Sc-supersaturation for AC and EBRS samples aged at 325°C and 400°C for 180 min; The size distributions are similar for a given temperature and are shifted to larger radii with increasing temperature.

The Al_3(Sc,Zr) precipitate volume fraction was calculated for the samples aged at 325°C and 400°C. Fig. 5.13 (a) shows the volume fraction versus the amount of Sc in solution prior to ageing for a total of three Sc-concentrations: 0 wt.%, 0.13 wt.% (AC), and 0.37 wt.% (EBRS). The virtual measurement point at 0 wt.% Sc, logically, gives a volume fraction of 0. The dashed line represents the theoretical limit calculated for room temperature from the Al-Sc phase diagram (Fig. 2.13) neglecting the Zr content by:

$$f_V = \frac{f_{W,0} - f_{W,\alpha}}{f_{W,Al_3Sc} - f_{W,\alpha}} \cdot 0.867. \tag{5.3}$$

$f_{W,0}$ is the weight percentage of Sc in the entire alloy, $f_{W,\alpha}$ is the Sc weight percentage in α-Al, f_{W,Al_3Sc} is the Sc content in Al_3Sc, and the value 0.867 is the conversion factor between Al_3Sc weight and volume fraction. At room temperature, $f_{W,\alpha} = 0\%$ and $f_{W,Al_3Sc} = 35.7\%$. The solubility of Sc in α-Al, $f_{W,\alpha}$, increases slightly with increasing temperature, as shown in Fig. 2.14 (b). In numbers, $f_{W,\alpha}$ equals about 0.01 wt.% at 325°C, and 0.02 wt.% at 400°C. Consequently, the difference in solubility up to 400°C is so small, that the error introduced by approximating the theoretical volume fraction with that of room temperature is considered as negligible.

The measured precipitate volume fractions after 180 min of ageing in Fig. 5.13 (a) showed a monotonous increase with increasing degree of Sc-supersaturation (0 to 0.37 wt.% Sc) for both ageing temperatures. Following the theoretical limit, the volume fractions showed a nearly linear dependency with the amount of Sc in solution prior to ageing. The curves were almost identical for the different ageing temperatures, indicating that an equilibrium state has already been reached in all cases. The references appended to Fig. 5.13 (a) will be discussed in detail in section 6.3.4.2.

Fig. 5.13 (b) presents the influence of ageing temperature and degree of Sc-supersaturation on the Al_3(Sc,Zr) number density. For both temperatures, the number density increased linearly with the Sc content in solution prior to ageing, with the slope at 325°C being 2.5 times that at 400°C. All the measured and calculated values of the TEM investigation are summarized in Table 5.5. The rather large standard deviations are not uncommon and result of the broad precipitate size distribution (Fig. 5.12 a), comparable to [41,86]. In addition, the thickness of the TEM samples may influence the results when considering very small precipitate sizes leading to larger standard deviations. However, similar standard deviations were observed for atom probe tomography studies [97,165]. The logical context of the values shown in Table 5.5 is verifiable within the standard deviations using a simple mathematical prove.

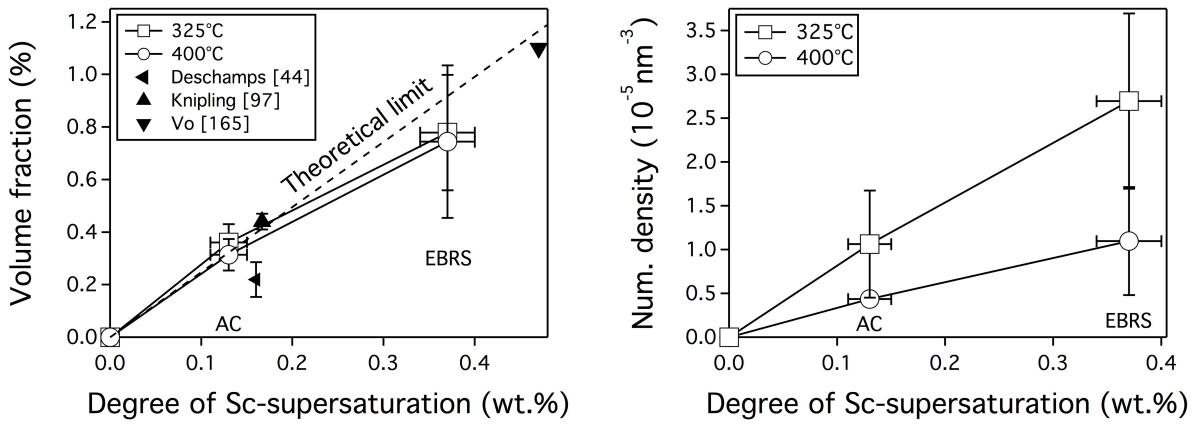

(a) Al_3(Sc,Zr) precipitate volume fraction

(b) Precipitate number density

Fig. 5.13: Al_3(Sc,Zr) precipitate volume fraction (a) and number density (b) for 0 wt.%, 0.13 wt.% (AC), and 0.37 wt.% Sc (EBRS) samples aged at 325°C and 400°C for 180 min in a furnace. The measuring point at 0 wt.% Sc represents a virtual measurement. The theoretical limit in (a) corresponds to the equilibrium Al_3Sc volume fraction in a binary Al-Sc phase diagram at room temperature. Precipitate volume fraction and number density increase with increasing degree of Sc-supersaturation.

Table 5.5: Summary of the precipitate characterization of AC and EBRS samples aged at 325°C and 400°C for 180 min in terms of mean radius, volume fraction, and number density. Average values and standard deviations.

		Mean radius (nm)		Vol. fraction (%)		Num. dens. (10^{-6} nm^{-3})	
Condition	Temp.	Avg.	Std. dev.	Avg.	Std. dev.	Avg.	Std. dev.
AC	325°C	3.8	2.03	0.36	0.07	10.6	6.1
	400°C	5.2	1.76	0.31	0.06	4.4	0.6
EBRS	325°C	3.4	1.83	0.78	0.22	26.9	9.9
	400°C	5.1	1.72	0.74	0.29	10.9	6.2

5.3 Recrystallization kinetics

The recrystallization kinetics of samples in as-cast (AC) and pre-aged (PA) conditions were studied focusing on the influence of the degree of cold deformation and ageing temperature. The hardness evolution in deformed (0.5 and 1.5 strain) an non-deformed (ND) materials (Fig. 4.1) was studied after ageing at 325°C, 400°C, and 500°C for up to 60 min in a dilatometer. The corresponding microstructure evolution was observed in-situ by CLSM, and characterized by EBSD and EFTEM. The in-situ CLSM approach is shown in detail for AC samples deformed to 0.5 and 1.5 strain aged at 400°C. For all other samples aged at different temperatures and having different inital conditions, only the main results are presented. The main part of this section deals with the AC materials condition, whereas only selected PA samples were used for comparison. Therefore, unless indicated differently, unspecified sample conditions refer to the as-cast (AC) state.

5.3.1 Deformed material

Fig. 5.14 (a) shows an EBSD boundary map of a sample in non-deformed (ND) AC condition revealing no local misorientations inside the grains. An increasing local misorientation was observed after cold deformation to strains of 0.5 (Fig. 5.14 b) and 1.5 (Fig. 5.14 c), whereas the degree of misorientation was more pronounced for the sample deformed to 1.5 strain. The grains became flatter the higher the plastic strain, and large black areas with low confidence index (CI) resulting from high local strains appeared (Fig. 5.14 c). The lowest hardness of 69 ± 2.9 HV0.1 was measured for the ND-material, in agreement with Table 5.1. The material deformed to 0.5 strain revealed a hardness value of 99 ± 4.5 HV0.1 and that deformed to 1.5 strain a value of 111 ± 5.1 HV0.1.

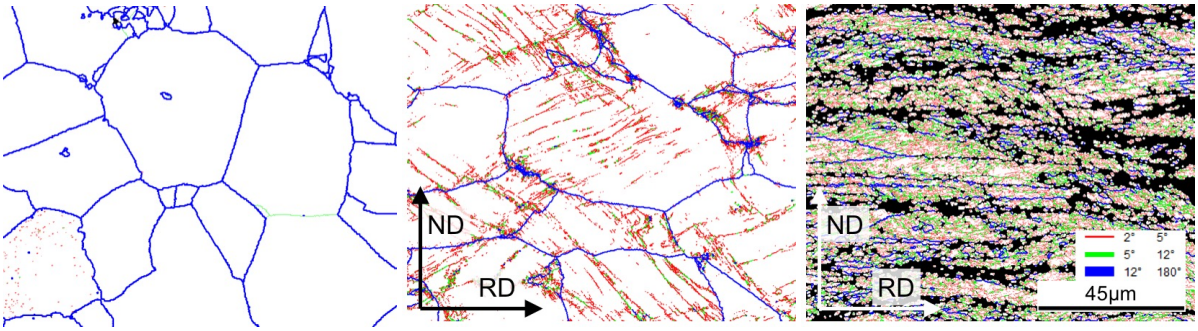

(a) Non-deformed AC material (b) Deformed to 0.5 strain (c) Deformed to 1.5 strain

Fig. 5.14: EBSD boundary maps of non-deformed AC material (a) and AC samples deformed to 0.5 (b) and 1.5 (c) strain showing increasing misorientation with increasing strain. Deformation occurred in vertical direction, as for all microstructure images.

5.3.2 Hardness evolution

Fig. 5.15 shows the hardness evolution in deformed (D) and non-deformed (ND) sample positions of AC material after ageing for different times at 325°C (a), 400°C (b), and 500°C (c). The end of the 1 min heat-up stage from room temperature to the respective target temperature is indicated with a vertical dashed line. The initial values represent the hardness at room temperature prior to ageing for the different materials conditions. In Fig. 5.15, error bars representing the standard deviations are only presented for selected measurements to improve the readability of the figures. The sizes of the plotted error bars are representative for all other error bars.

At 325°C, the hardness in ND condition remained at the initial level for 1 min of isothermal ageing followed by a steep increase up to the maximum hardness after around 20 min (Fig. 5.15 a). The hardness values of the deformed samples decreased during the heating stage, then remained at the reduced hardness level for about 1 min before increasing to a constant plateau which was reached after the same time as the maximum for ND condition. The hardness values of the sample deformed to 1.5 strain were always higher than that of the sample deformed to 0.5 strain.

The shapes of the hardness evolution curves obtained at 400°C were similar to that of ageing at 325°C, as shown in Fig. 5.15 (b). In ND condition, the hardness started to increase immediately after heat-up and the maximum hardness was reached already after around 5 min. The hardness maximum at 400°C was lower than that at 325°C. The deformed samples showed a hardness reduction during heating, followed by an immediate hardness increase to a constant plateau. This plateau was again reached after the same period of time as for the ND sample.

For the samples aged at 500°C (Fig. 5.15 c), the hardness evolution showed a different behavior. The hardening of the ND material occurred already during heat-up and the maximum hardness was reached after 30 s of isothermal ageing. In contrast to the ND material aged at 325°C and 400°C, the samples aged at 500°C revealed a considerable hardness drop after the peak hardness was reached. Similar behavior was observed for the deformed material, where the hardness decreased significantly during the heat-up stage, followed by a steady hardness decrement upon ageing. However, the hardness of the deformed material was still higher than that of the ND condition.

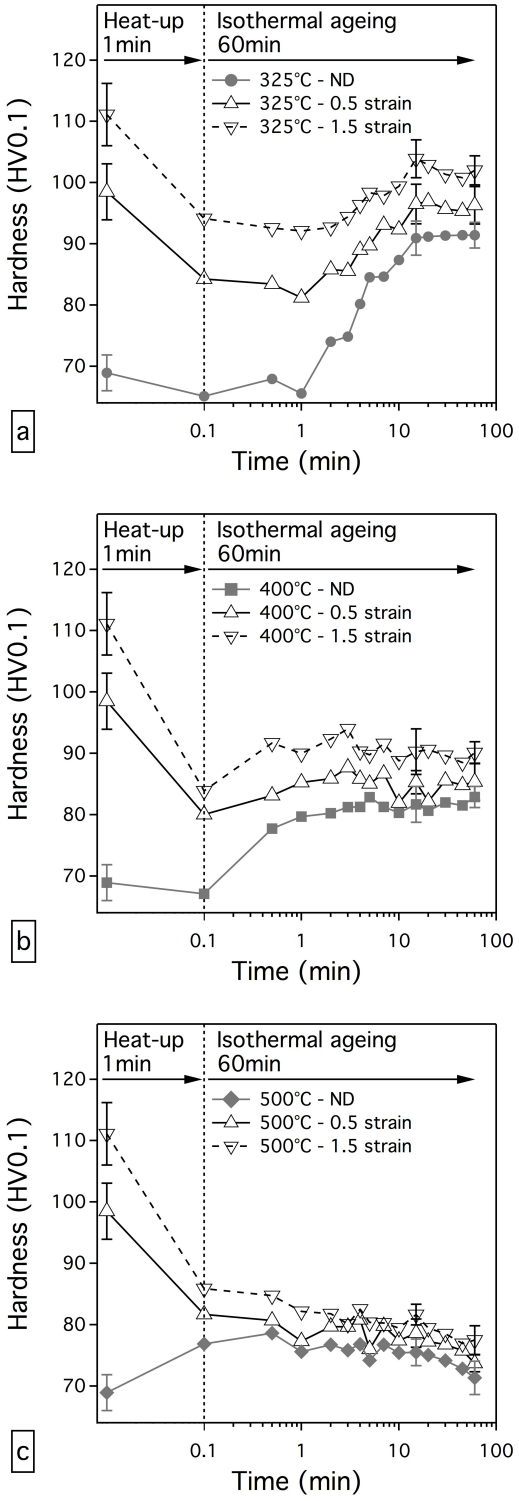

Fig. 5.15: Hardness evolution in deformed (0.5 and 1.5 strain) and non-deformed (ND) AC conditions over time during ageing at 325°C (a), 400°C (b), and 500°C (c). The vertical dashed lines represent the end of the 1 min heat-up stage from room temperature to the respective target temperature prior to isothermal ageing for 60 min.

5.3.3 In-situ CLSM

Samples cold deformed to 0.5 and 1.5 strain were annealed in a confocal laser scanning microscope using exactly the same temperature cycle as for the dilatometer annealing. The in-situ CLSM methodology is introduced using the AC samples aged at 400°C.

5.3.3.1 Microstructure prior to annealing

The basic principle to visualize grain boundaries in a CLSM is illustrated in Fig. 5.16. At room temperature before aging (Fig. 5.16 a) no grain boundaries were visible. The polished surface only revealed a large primary $Al_3(Sc,Zr)$ phase in the center as well as some small pores. While heating-up the sample, grain boundaries became visible due to thermal grooving [166], as shown in Fig. 5.16 (b). Some of the grain boundaries (HAGB) are indicated exemplarily in the image. After heating to 400°C, the CLSM image in Fig. 5.16 (b) corresponded quite well to the EBSD boundary map acquired at room temperature before ageing shown in Fig. 5.16 (c). For further analyses, therefore, CLSM images captured immediately after heating-up (e.g. Fig. 5.16 b) were considered as equivalent to the as-deformed microstructure.

5.3.3.2 Microstructure evolution during annealing

Microstructural changes during annealing were documented by capturing CLSM snapshots. For the AC sample deformed to 0.5 strain aged at 400°C, several of these images are presented in Fig. 5.17. The temporal range of snapshots covers the full annealing

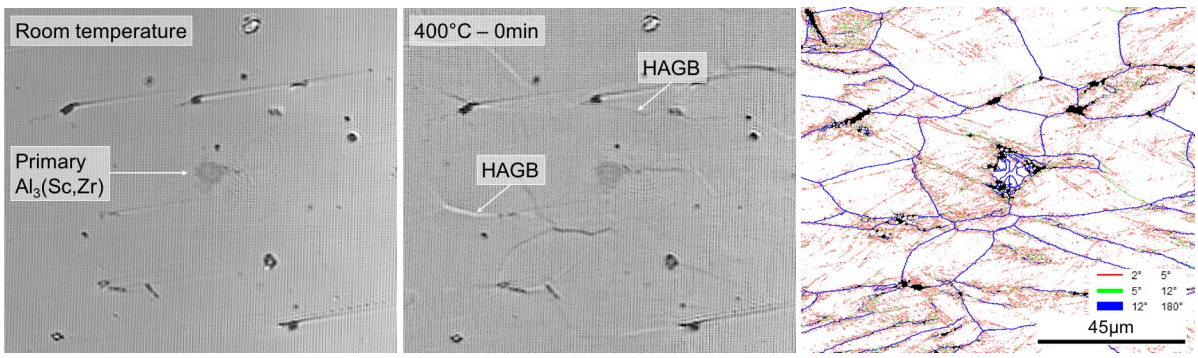

(a) Room temperature image (b) Image after heat-up to 400°C (c) EBSD boundary map

Fig. 5.16: CLSM images of a sample deformed to 0.5 equivalent strain at room temperature (a). After heat-up to 400°C (b) high angle grain boundaries (HAGB) become visible, as indicated exemplarily. Corresponding EBSD boundary map (c) acquired at room temperature.

timespan from 0 to 60 min. When comparing the figures, it can be observed that the microstructure at the surface transformed in several ways. On the one hand, stable boundaries became richer in contrast due to thermal grooving, for example the HAGB highlighted in black. On the other hand, the migration of existing and formation of new boundaries could be pursued, as indicated exemplarily with a white arrow. The local initiation of boundary movement at triple points occurred by a rapid migration within the first minute. Further boundary migrations became increasingly slower until the microstructure modifications ceased after around 5 min. Concerning the temporal sequence, no further modifications could be detected until the end of the in-situ experiment.

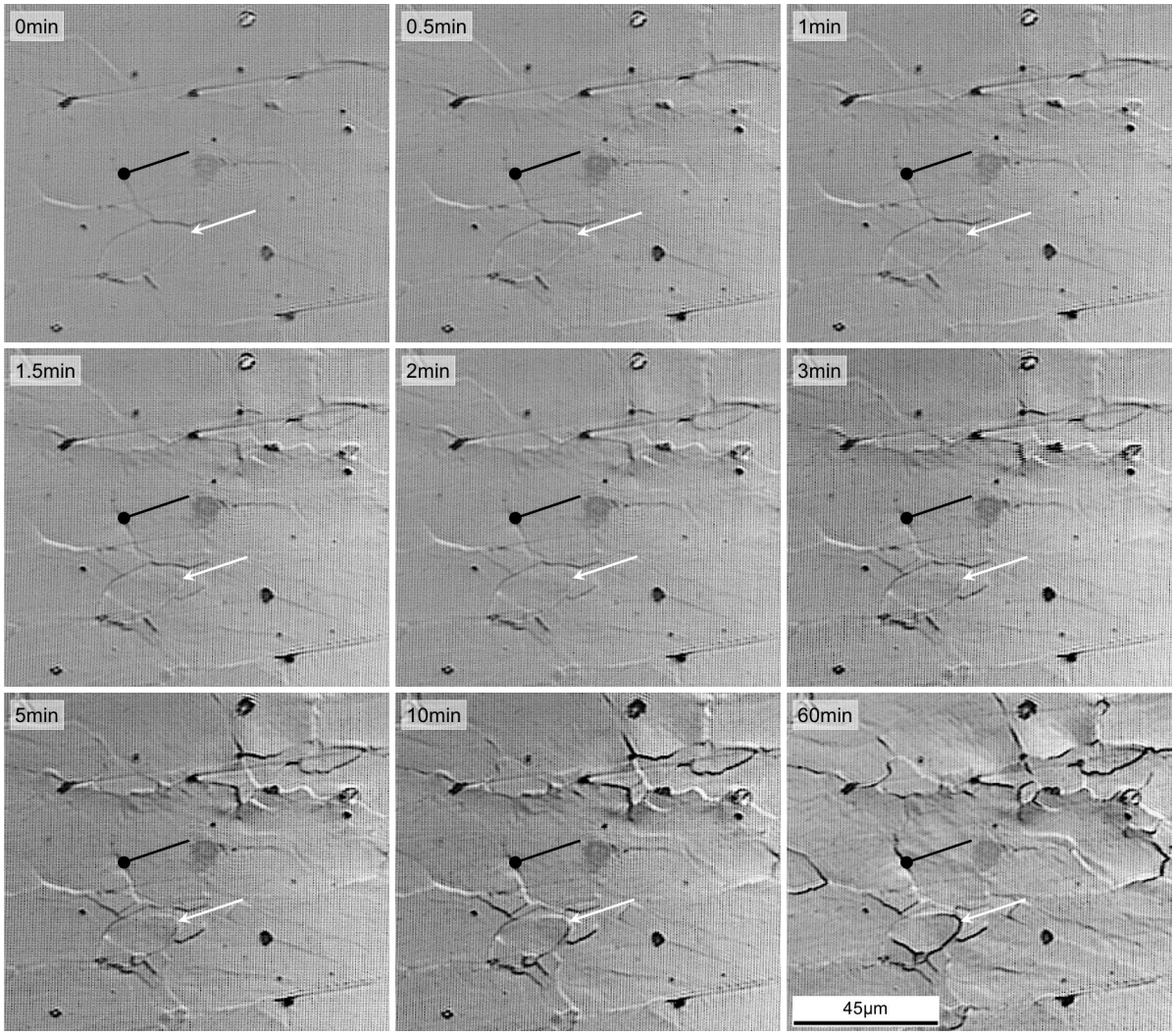

Fig. 5.17: Temporal sequence of CLSM images during annealing at 400°C of an AC sample deformed to 0.5 strain. Examples of stable boundaries (black) and moving boundaries (white) are highlighted.

5.3.4 Microstructure characterization

The grain structure after CLSM was characterized by EBSD to confirm and further analyze the in-situ observations. Precipitate-boundary interactions were investigated by EFTEM measurements.

5.3.4.1 Verification of CLSM using EBSD

Fig. 5.18 shows a comparison of CLSM images and EBSD maps obtained before and after the annealing procedure at 400°C of an AC sample deformed to 0.5 strain. In the as-deformed state (Fig. 5.18 a to c) most of the HAGB could be observed in CLSM whereas boundaries with misorientations smaller 12° could not be detected. The EBSD maps revealed a deformed microstructure recognizable by local deformation bands with misorientations between 2 and 5° inside the grains.

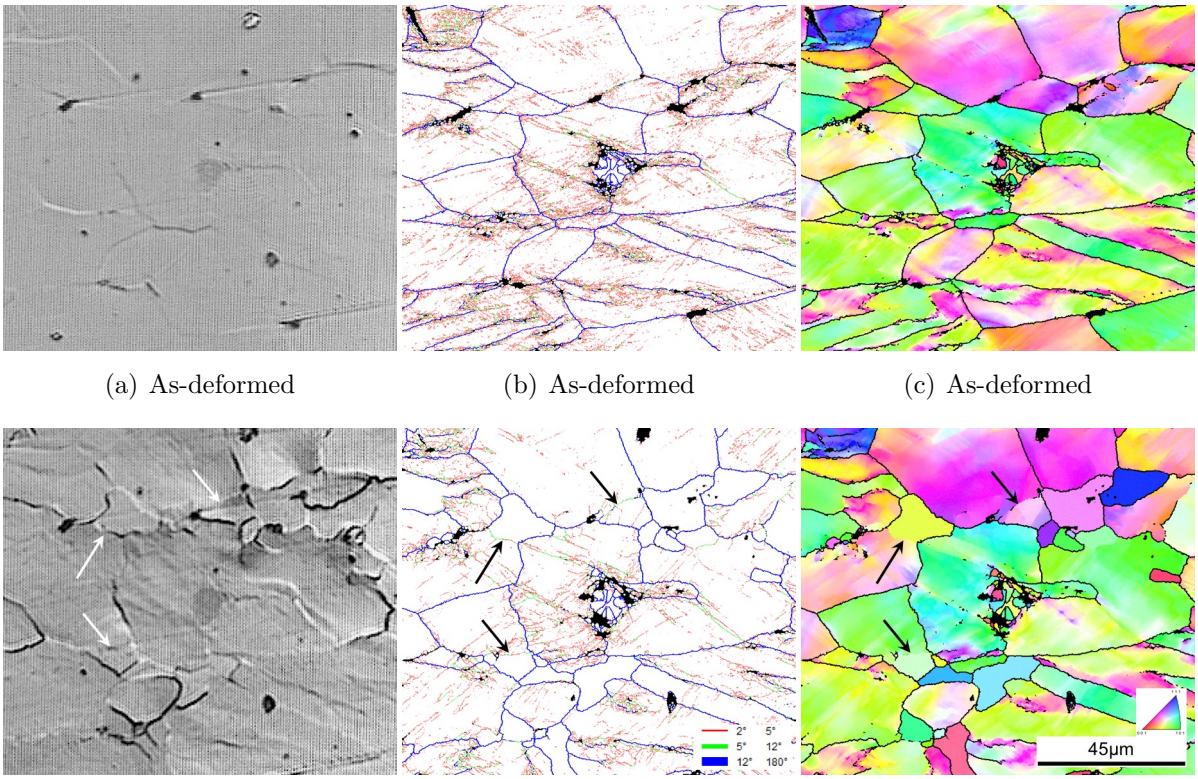

(a) As-deformed (b) As-deformed (c) As-deformed

(d) 400°C, 60 min (e) 400°C, 60 min (f) 400°C, 60 min

Fig. 5.18: Comparison of CLSM and EBSD data of a sample deformed to 0.5 strain: CLSM image (a), boundary map (b), and orientation map (c) of the as-deformed material; CLSM image (d), boundary map (e), and orientation map (f) of the same sample position after annealing at 400°C for 60 min.

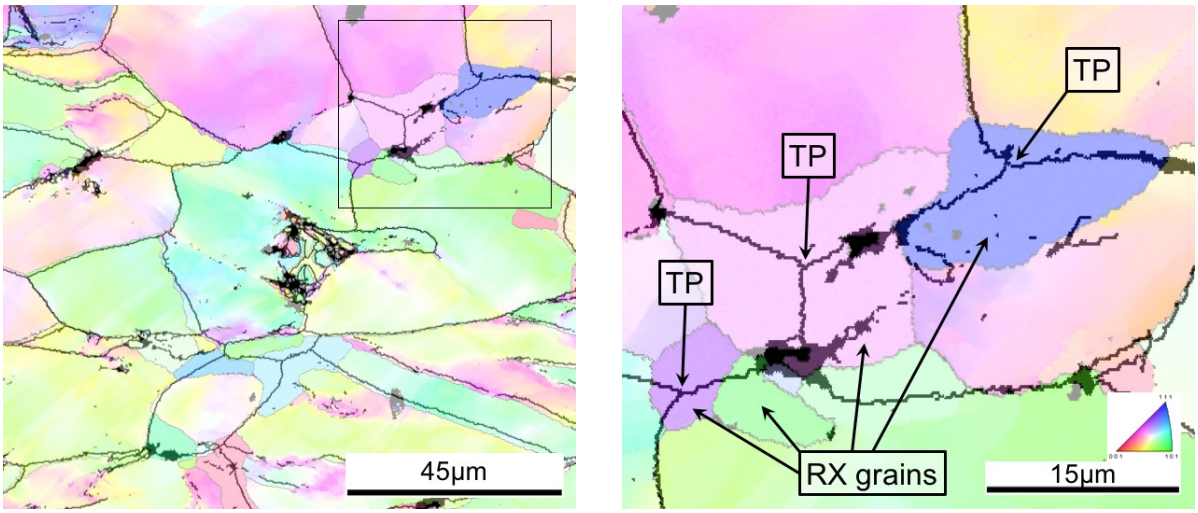

(a) Overview (b) Detail

Fig. 5.19: Superposition of an orientation map after annealing at 400°C for 60 min with a 12° boundary map of the same sample position before aging (bold lines); Arrows indicate that recrystallized (RX) grains nucleated at grain boundary triple points (TP); sample cold deformed to a strain of 0.5.

During CLSM at 400°C for 60 min (Fig. 5.18 d to f), the microstructure was modified and new boundaries formed. A very good correlation of the HAGB measured from EBSD with the visible boundaries in CLSM was found when comparing Fig. 5.18 (d to f). The newly formed grains were free of local misorientations and thus clearly recrystallized. In addition, large recovered subgrains with misorientations higher 7° were faintly visible in CLSM, as indicated by arrows in the images.

From the CLSM images in Fig. 5.17 it was stated that recrystallization initiated solely at grain boundary triple points. This observation was confirmed by a comparison of EBSD images of as-deformed and annealed states. Fig. 5.19 shows a superposition of HAGB of the as-deformed sample (bold line) on an orientation map of the same sample after annealing. The recrystallized (RX) grains were located at the former triple points (TP). At this point it should be mentioned, that the 2D-observation of a 3D-phenomenon such as recrystallization may lead to misinterpretation of some aspects of the observed process. A comparison between surface and bulk observations is given in 5.3.6.

5.3.4.2 Precipitate-boundary interactions

EFTEM investigations of HAGB between recrystallized and non-recrystallized grains were performed after annealing at 400°C for 60 min. Fig. 5.20 shows a zero-loss filtered

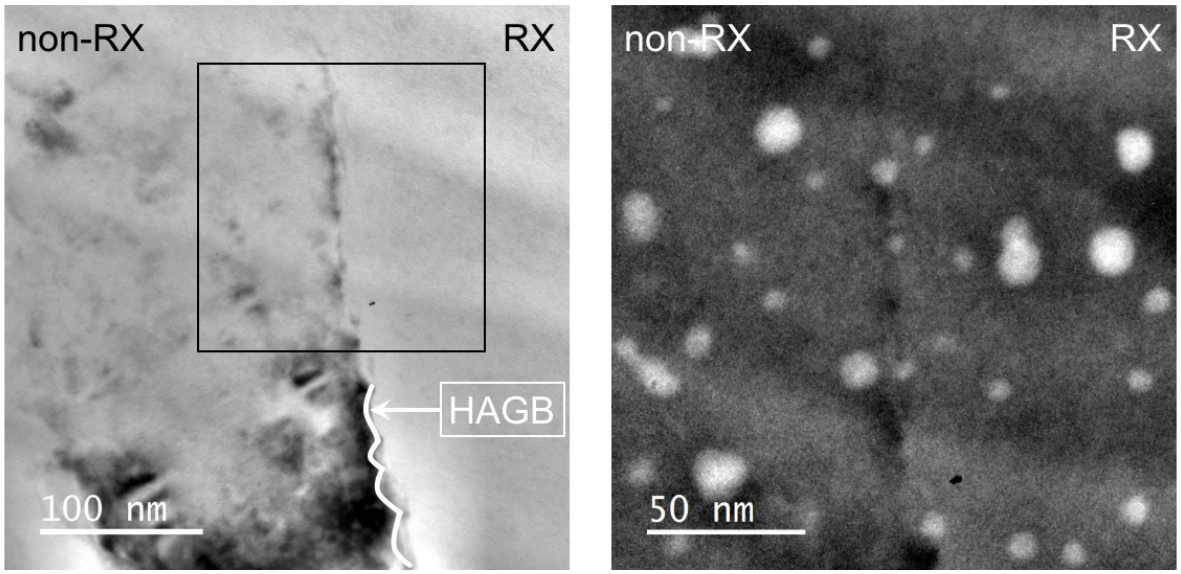

(a) Zero-loss overview image

(b) Energy-filtered detail image

Fig. 5.20: EFTEM images of a HAGB between a deformed (non-RX) and a recrystallized (RX) grain; zero-loss filtered (a) and filtered using a 10 eV slit at an energy loss of 40 eV (b). Sample deformed to 0.5 strain aged at 400°C for 60 min.

image (a) of such a boundary and the correlating image obtained at an energy loss of 40 eV (b). The right side of the images shows a recrystallized and the left side a non-recrystallized grain. The bright secondary $Al_3(Sc,Zr)$ precipitates in Fig. 5.20 (b) were homogeneously distributed in the matrix and no preferred nucleation at the HAGB was observed. The wavy shape of the HAGB, as highlighted in Fig. 5.20 (a), indicates that the boundary was moving from right to left (arrow) until it was pinned by the $Al_3(Sc,Zr)$ particles, that formed during annealing.

5.3.4.3 Characterization of highly deformed samples

The same CLSM and EBSD procedure as for the AC sample deformed to 0.5 strain was carried out for an AC sample deformed to 1.5 strain. Similar to the 400°C annealing of the sample deformed to 0.5 strain, the boundary migration was fast at the beginning of the in-situ CLSM experiment, whereas no further boundary migrations could be observed between around 5 and 60 min. Fig. 5.21 shows a comparison of CLSM and EBSD images before (a to c) and after (d to f) annealing at 400°C for 60 min. A correlation between CLSM and EBSD in the as-deformed state was given. Due to severe deformation resulting in a large amount of boundaries, however, the CLSM image was more diffuse compared to the sample deformed to 0.5 strain in Fig. 5.18 (a). The correlating EBSD maps in Fig.

5.21 (b) and (c) revealed a highly deformed microstructure with large areas of measured points with low CI values. When comparing the CLSM images before (a) and after annealing (d), several microstructure modifications were visible. However, in contrast to the less deformed sample (Fig. 5.18), not all of the new boundaries were clearly detectable in CLSM, as can be observed when comparing the CLSM and EBSD images after annealing (Fig. 5.21 d to f). In case of a large amount of small grains, therefore, CSLM alone gave only a rough estimation of the size of the recrystallized area. For the sample deformed to an equivalent strain of 1.5, recrystallization occurred at severely deformed sample positions and grain boundary triple points (Fig. 5.21 e and f).

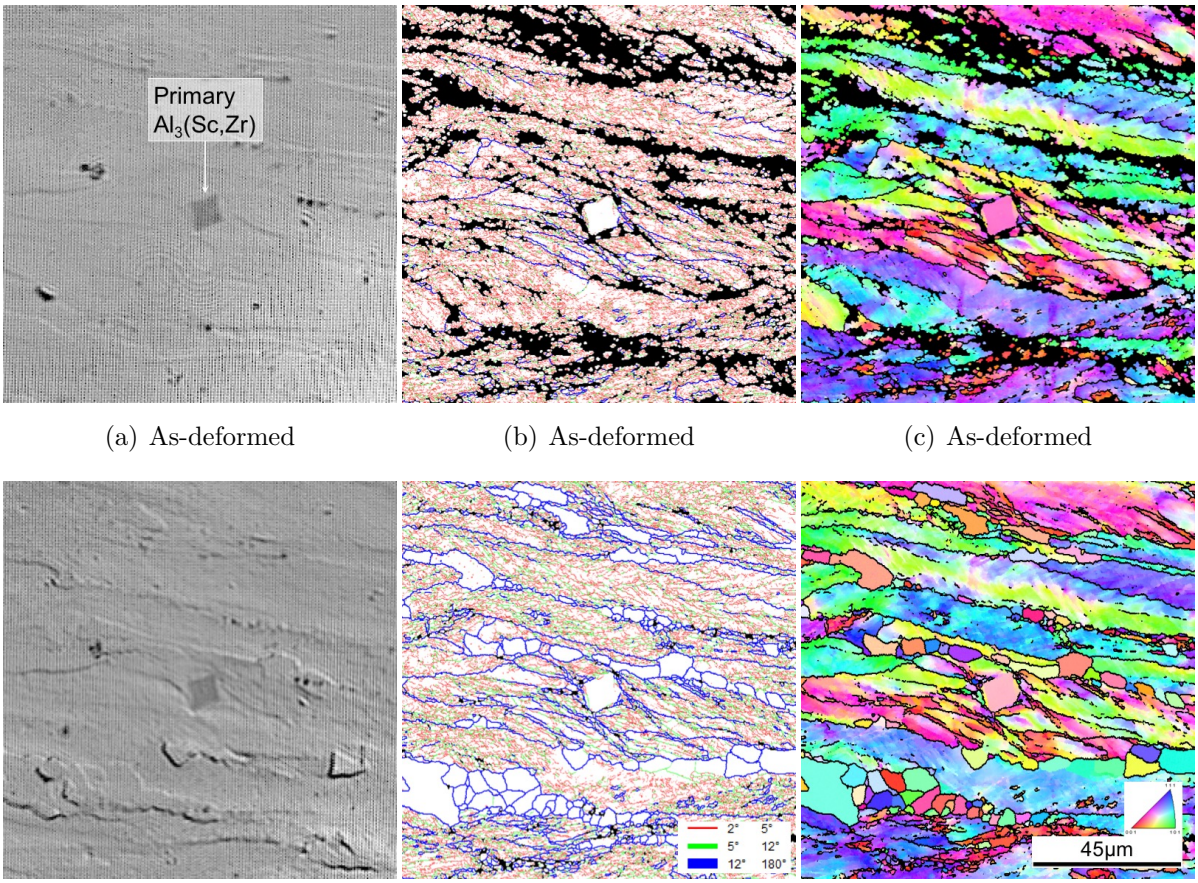

(a) As-deformed (b) As-deformed (c) As-deformed

(d) 400°C, 60 min (e) 400°C, 60 min (f) 400°C, 60 min

Fig. 5.21: Comparison of CLSM and EBSD data of a sample deformed to 1.5 strain: CLSM image (a), boundary map (b), and orientation map (c) of the as-deformed material; CLSM image (d), boundary map (e), and orientation map (f) of the same sample position after annealing at 400°C for 60 min.

5.3.5 Quantification of recrystallization

The quantification of recrystallization includes the isolation of recrystallized grains as well as the assessment of the fraction of recrystallized material and the temporal evolution, i.e. beginning and end of recrystallization processes, for all investigated samples.

5.3.5.1 Isolation of recrystallized grains

Fig. 5.22 illustrates the isolation of recrystallized grains based on EBSD and EDS data for AC samples after CLSM-annealing at 400°C for 60 min. Fig. 5.22 (a to c) shows the sample deformed to 0.5 strain, Fig. 5.22 (d to f) shows that deformed to a strain of 1.5. GOS and EDS Sc-maps were used to isolate the recrystallized grains from deformed grains and primary $Al_3(Sc,Zr)$ phases. The superpositions of CLSM images with the isolated recrystallized grains in Fig. 5.22 (c, f) showed very good correlation.

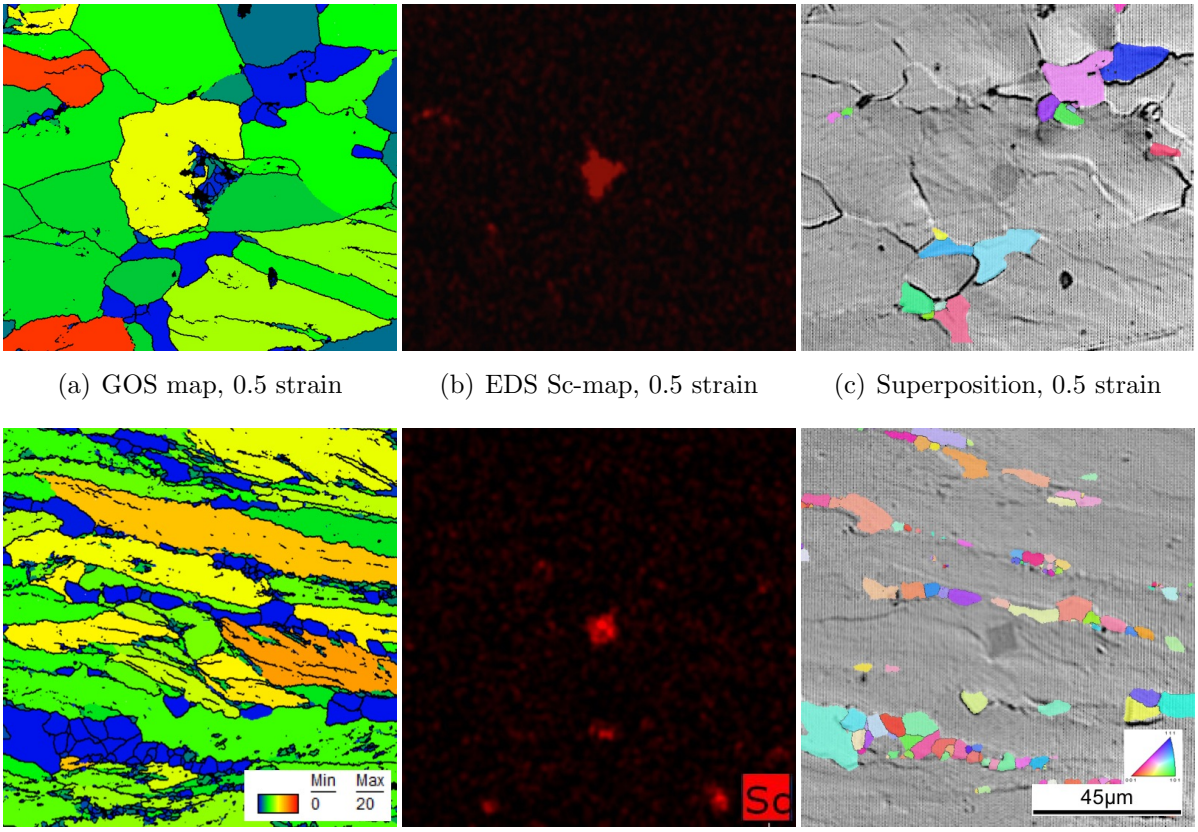

(a) GOS map, 0.5 strain (b) EDS Sc-map, 0.5 strain (c) Superposition, 0.5 strain

(d) GOS map, 1.5 strain (e) EDS Sc-map, 1.5 strain (f) Superposition, 1.5 strain

Fig. 5.22: Analysis of recrystallized area fraction for samples deformed to 0.5 (a to c) and 1.5 (d to f) strain. GOS maps (a, d), EDS Sc-maps (b, e), superpositions of recrystallized grains (orientation maps) with correlating CLSM images (c, f).

5.3.5.2 Evolution of recrystallization

Similar to the samples deformed to 0.5 and 1.5 strain aged at 400°C, the evolution of grain boundary migrations was assessed for all other AC samples. The outcome of these CLSM investigations is summarized in Fig. 5.23 for the AC samples deformed to 0.5 strain and in Fig. 5.24 for those deformed to 1.5 strain. For both Figs. 5.23 and 5.24, the images in the top row correspond to ageing at 325°C, the center row refers to annealing at 400°C, and the bottom row to 500°C. The left columns in the figures show CLSM snapshots taken at the respective critical time where boundary migrations ceased. In the center columns, the corresponsing EBSD boundary maps after 60 min of annealing are given. The CLSM snapshots at the critical time with the isolated recrystallized grains of the respective EBSD images after 60 min of ageing are shown in the right column.

No HAGB migrations could be observed in an AC sample deformed to 0.5 strain during annealing for 60 min at 325°C (Fig. 5.23 a). Accordingly, no recrystallized grains were detected by means of EBSD (Fig. 5.23 b) and no critical time was determined. During annealing at 400°C, it was observed that boundary migrations ceased after 5 min (Fig. 5.23 c). The corresponding EBSD boundary map after 60 min (Fig. 5.23 d) revealed several recrystallized grains. The excellent correlation of these recrystallized grains with the CLSM snapshot at 5 min shown in Fig. 5.23 (e) proved that no further boundary migrations occurred after this critical time. At 500°C similar behavior as at 400°C was observed, however, the critical time was reached already after 30 s. Again, the CLSM snapshot after 30 s showed good correlation to the recrystallized grains obtained from EBSD after 60 min, as illustrated in Fig. 5.22 (h).

The determination of the critical times where boundary migrations stopped was less precise for the samples deformed to 1.5 strain as a result of the smaller recrystallized grain sizes. During annealing at 325°C (Fig. 5.24 a to c), the sample deformed to 1.5 strain showed only minor modifications in the microstructure with respect to grain boundary movement. The EBSD boundary map after 60 min of annealing, shown in Fig. 5.24 (b), revealed fine recrystallized grains that could not be clearly identified in the CLSM. At 400°C (Fig. 5.24 d to f) the boundary migrations stopped after roughly 5 min. The EBSD boundary map showed a larger amount of recrystallized grains compared to the sample aged at 325°C. At 500°C (Fig. 5.24 g to i) the boundary migrations occurred quickly and stopped already after around 30 s. The superpositions of CLSM and EBSD images (Fig. 5.24 c, f, i) showed good correlation, however, small grains were not clearly detectable in the CLSM with the used optics. The area fraction of recrystallized grains increased with increasing temperature, while the grains were located in distinct bands in all cases.

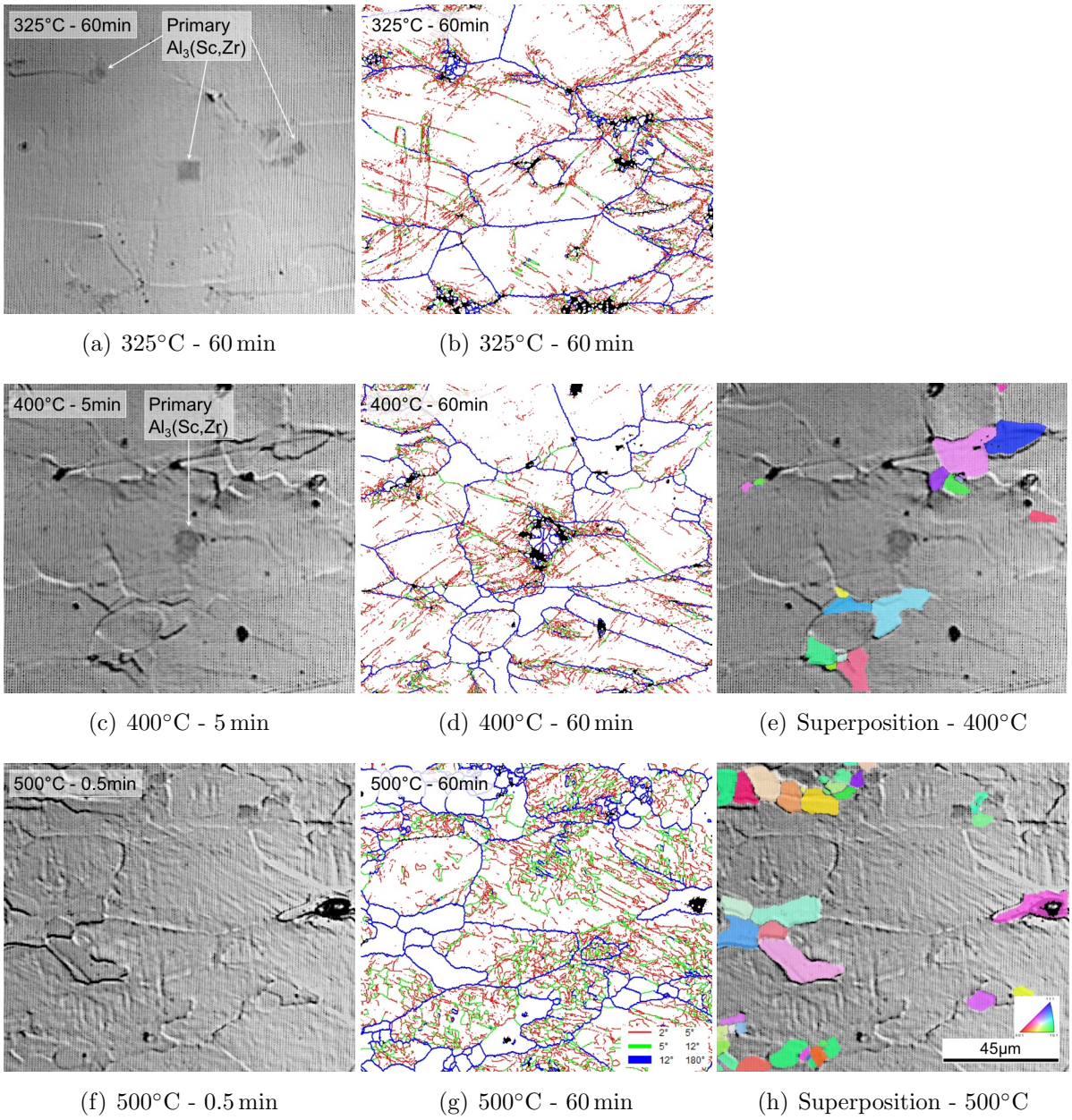

(a) 325°C - 60 min (b) 325°C - 60 min

(c) 400°C - 5 min (d) 400°C - 60 min (e) Superposition - 400°C

(f) 500°C - 0.5 min (g) 500°C - 60 min (h) Superposition - 500°C

Fig. 5.23: Microstructure characterization of AC samples deformed to 0.5 strain aged at 325°C (a, b), 400°C (c, d, e), and 500°C (f, g, h): In-situ CLSM snapshots (a, c, f) at the critical ageing time, where visible microstructural modifications stopped. EBSD boundary maps after ageing for 60 min (b, d, g) of the same sample position as in (a, c, f) where strain-free grains (white) represent recrystallized grains. Superposition (e, h) of the CLSM image with the isolated recrystallized grains represented as an orientation map.

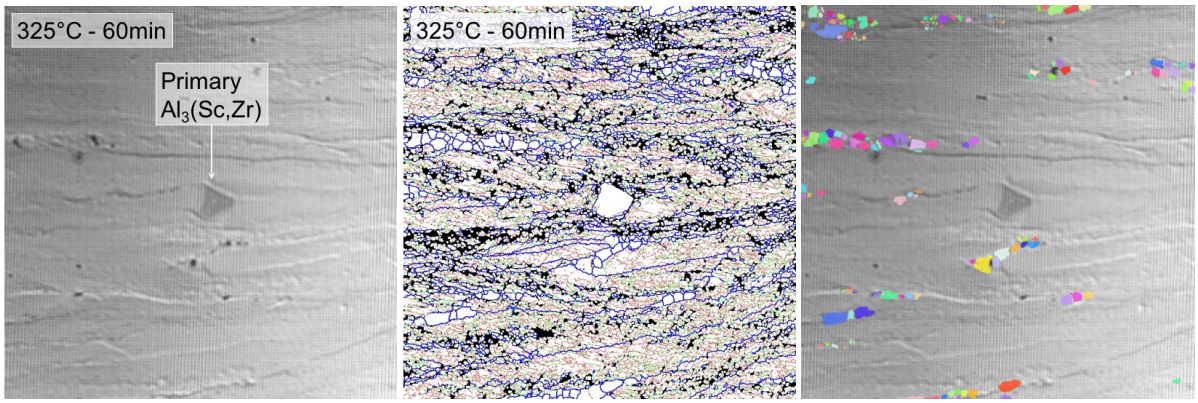

(a) 325°C - 60 min (b) 325°C - 60 min (c) Superposition 325°C

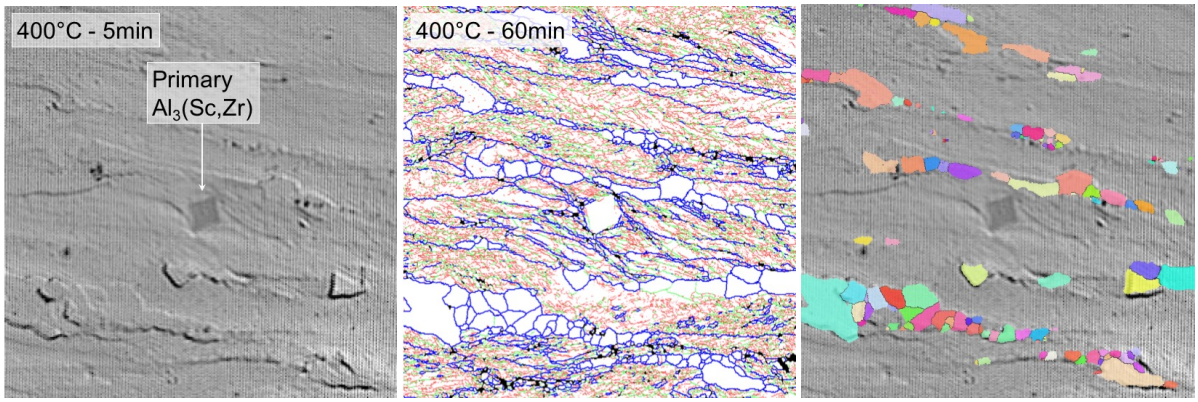

(d) 400°C - 5 min (e) 400°C - 60 min (f) Superposition - 400°C

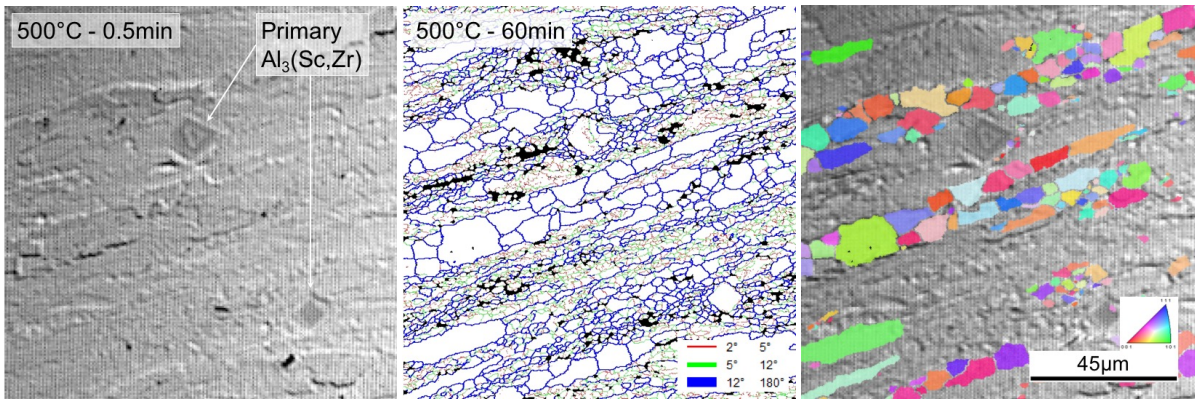

(g) 500°C - 0.5 min (h) 500°C - 60 min (i) Superposition - 500°C

Fig. 5.24: Microstructure characterization of AC samples deformed to 1.5 strain aged at 325°C (a, b, c), 400°C (d, e, f), and 500°C (g, h, i): In-situ CLSM snapshots (a, d, g) at the critical ageing time, where visible microstructural modifications stopped. EBSD boundary maps after ageing for 60 min (b, e, h) of the same sample position as in (a, d, g) where strain-free grains (white) represent recrystallized grains. Superposition (c, f, i) of the CLSM image with the isolated recrystallized grains.

5.3.5.3 Fraction of recrystallized material

Fig. 5.25 shows the quantification of the recrystallized area fraction as a function of initial strain and annealing temperature after ageing for 60 min. The values were determined from the EBSD images shown in Fig. 5.23 and Fig. 5.24. In accordance with state-of-the-art knowledge on recrystallization [39,64], the recrystallized area fraction increased with increasing annealing temperature and strain. Consequently, a maximum recrystallized area fraction of 27% was observed for the sample deformed to 1.5 strain aged at 500°C. The recrystallized grain size was rather constant over the ageing temperatures for a given strain and revealed values of around 6.5 µm for a strain of 0.5 and around 3 µm for a strain of 1.5, in good agreement with [39]. The quantification of the grain size should be considered as a very rough analysis as a result of the small amount of grains.

A summary of the temporal evolution, the recrystallized area fraction, and the size of recrystallized grains is given in Table 5.6. The critical times where boundary migrations stopped could be clearly identified for the samples deformed to 0.5 strain. At 325°C no HAGB migrations were observed, while boundary migrations ceased after 5 min at 400°C and after 0.5 min at 500°C. The determination of the critical time was less precise for the samples deformed to 1.5 strain as a result of the smaller grain size. Here, the HAGB migrations ceased before 60 min of ageing at 325°C. At 400°C and 500°C, the critical times were in a similar range than those determined for the respective samples deformed to 0.5 strain.

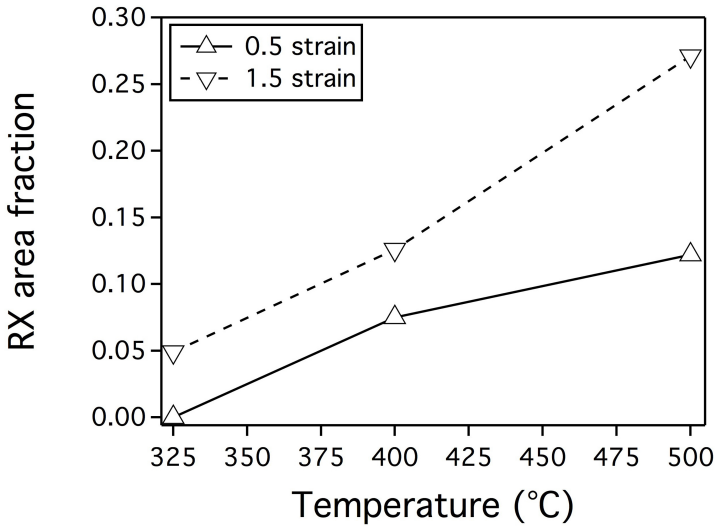

Fig. 5.25: Recrystallized (RX) area fraction at the surface after ageing for 60 min showing an approximately linear dependency with the ageing temperature for AC material.

Table 5.6: Summary of the results from recrystallization quantifications for AC samples.

Condition	Strain ( )	Temperature (°C)	Critical time (min)	RX area fraction (%)	RX grain size (µm)
AC	0.5	325	-	0	-
		400	5	7.5	7.44 ± 5.21
		500	0.5	12.2	5.76 ± 3.29
AC	1.5	325	< 60	4.9	1.97 ± 1.08
		400	~ 5	12.6	3.12 ± 2.45
		500	~ 0.5	27.1	3.29 ± 2.46

5.3.6 Correlation between surface and bulk material

The data points of the recrystallized area fraction shown in Fig. 5.25 were derived from individual measurements on the sample surface. Therefore, error bars are missing in the graphs as a meaningful estimation of the measurement error was not possible. In addition, it is known that diffusion controlled processes such as recrystallization or precipitation may show different behavior on surfaces than inside a sample volume. As a consequence, a fundamental aspect when considering in-situ observations on surfaces is the comparison of the observed surface phenomena to the behavior inside the bulk material. The analysis of the bulk material and the comparison to the observations on the sample surface were carried out for the AC samples annealed at 400°C only.

The microstructural features obtained from the bulk of samples deformed to 0.5 and 1.5 strain aged at 400°C for 60 min are presented in Fig. 5.26 and Fig. 5.27, respectively. The sample deformed to 0.5 strain revealed a recrystallized area fraction of 7.2% with an average grain size of 5.6 µm. The sample deformed to a strain of 1.5 showed a recrystallized area fraction of 18.5% with an average grain size of 3.9 µm. The recrystallized area fraction and grain size of the surface and bulk are summarized in Fig. 5.28. When considering the area fraction, a good correlation between surface and bulk could be observed. The surface and bulk values for a given strain were comparable and the trend of increasing area fraction with increasing strain was in good agreement with state-of-the-art research [39,64]. The recrystallized grains were located at grain boundary triple points, which is in good agreement with the observations at the surface. The picture was similar for the recrystallized grain sizes: The measured values for surface and bulk were in the same range and the decreasing grain size with increasing strain applied to the basics of recrystallization. For both recrystallized area fraction and grain size, the values of the surface lay within the standard deviations of the values inside the bulk material.

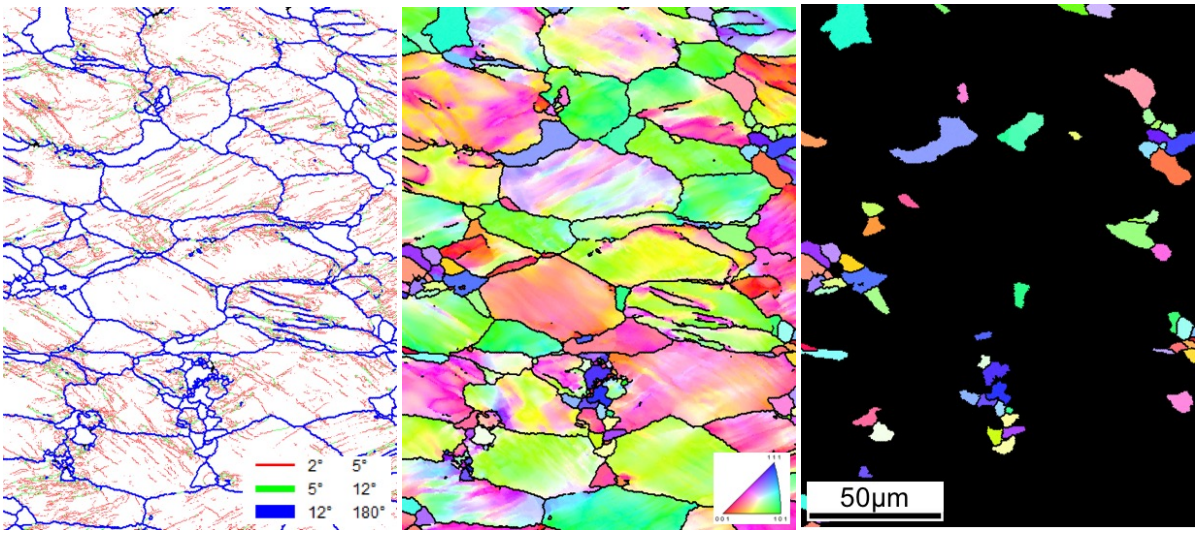

(a) Boundary map (b) Orientation map (c) Isolated recrystallized grains

Fig. 5.26: Boundary (a) and orientation map (b) of bulk material and isolated recrystallized grains (c). Sample deformed to 0.5 strain and annealed at 400°C for 60 min in a CLSM.

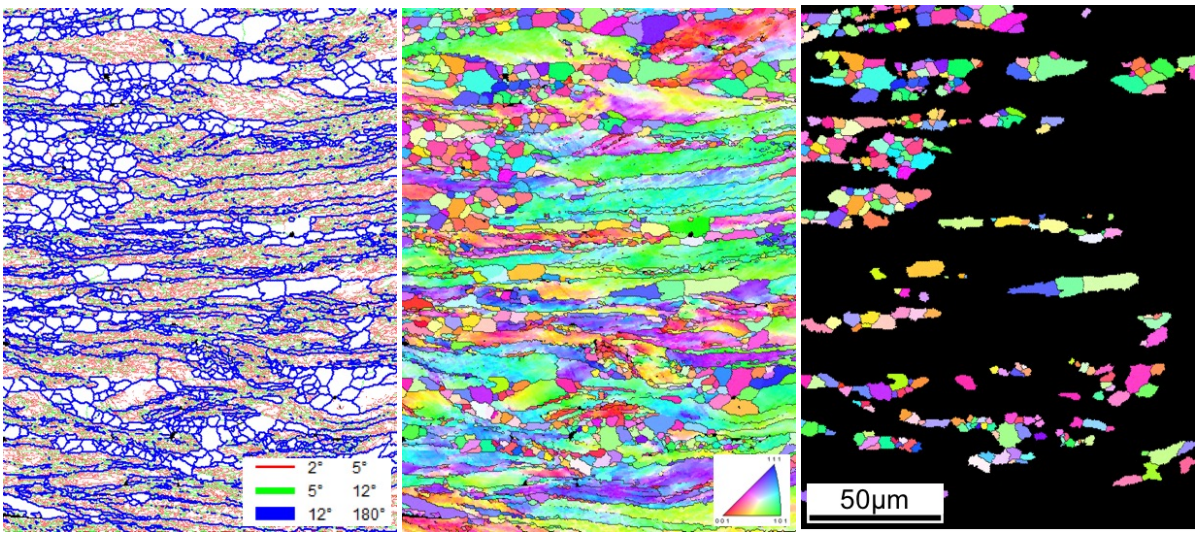

(a) Boundary map (b) Orientation map (c) Isolated recrystallized grains

Fig. 5.27: Boundary (a) and orientation map (b) of bulk material and isolated recrystallized grains (c). Sample deformed to 1.5 strain and annealed at 400°C for 60 min in a CLSM.

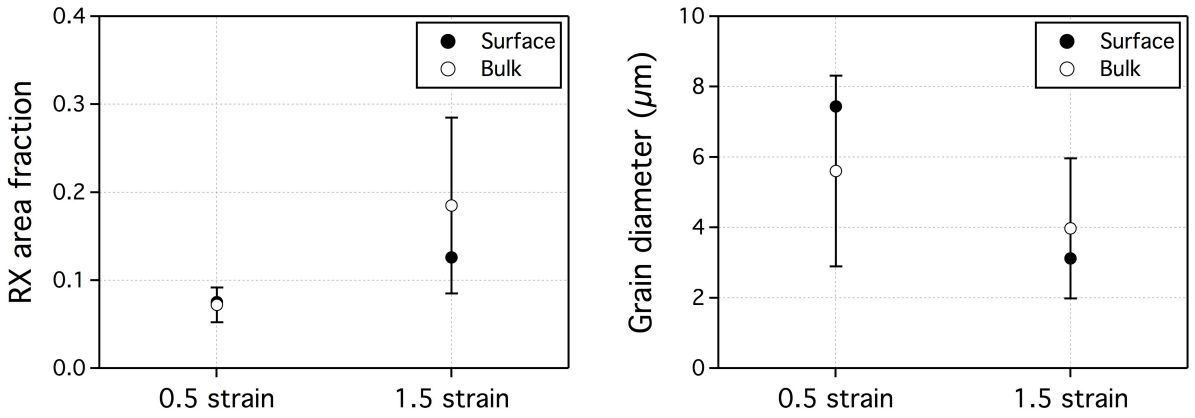

(a) RX area fraction

(b) Grain size of RX grains

Fig. 5.28: Recrystallized (RX) area fraction (a) and average grain size of the recrystallized grains (b) of surface and bulk material as a function of plastic deformation. Samples deformed to 0.5 and 1.5 strain prior to annealing at 400°C for 60 min. Error bars of bulk measurements represent the standard deviations calculated from average values of four individual EBSD measurements.

5.3.7 Pre-aged material

Pre-aged (PA) samples were analyzed during ageing at 400°C for 60 min in a dilatometer and inside the CLSM to investigate the influence of the initial precipitate state on the softening kinetics. In PA sample condition, Al_3(Sc,Zr) precipitates were already present prior to deformation. It was assumed that the precipitate volume fraction was close to equilibrium, i.e. $0.34 \pm 0.04\%$ (Table 5.5), as discussed in section 6.2.

5.3.7.1 Hardness evolution

The evolution of the hardness in non-deformed (ND) and deformed PA material is given in Fig. 5.29. As shown in Table 5.1, the initial hardness of the ND (PA) material was higher than that of the ND (AC) material. Due to pre-ageing at 325°C for 60 min, the initial hardness value of 94 ± 3.2 HV0.1 of the ND (PA) material was similar to the peak hardness of the ND (AC) sample aged at 325°C (Fig. 5.15 a). The deformed PA samples revealed initial hardness values of 113 ± 5.4 HV0.1 for 0.5 strain and 123 ± 6.1 HV0.1 for 1.5 strain.

The hardness of the ND (PA) material (Fig. 5.29) showed a minimal reduction during ageing at 400°C. As expected for an Al-(Mg)-Sc-Zr alloy, the hardness was reduced only gradually indicating slow coarsening of Al_3(Sc,Zr) precipitates. Precipitate coarsening,

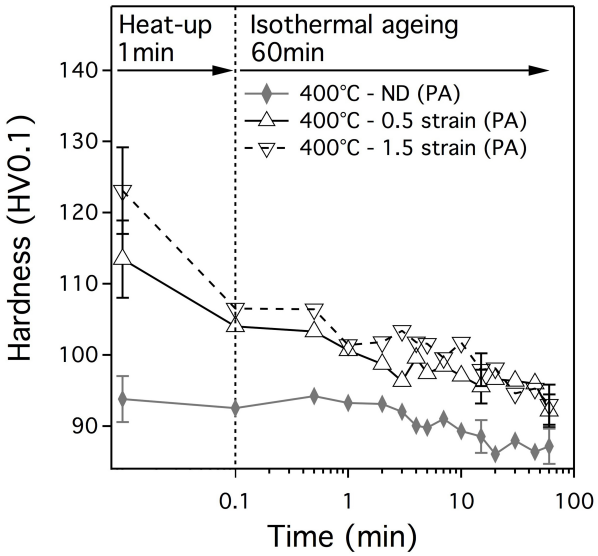

Fig. 5.29: Hardness evolution in non-deformed (ND) and deformed (0.5 and 1.5 strain) sample positions in PA material over time during ageing at 400°C. Vertical dashed line represents end of 1 min heating stage.

however, was not significant in the considered time range, as shown by the very limited reduction in hardness after 60 min of annealing. The deformed samples showed a decrease in hardness during the heat-up stage, followed by continuous but marginal softening until the end of the 60 min annealing procedure at 400°C. At any time, the hardness values of the deformed PA samples were slightly higher than that of the AC samples (Fig. 5.15) aged at the same temperature.

5.3.7.2 Microstructure characterization

Fig. 5.30 shows the outcome of the in-situ CLSM and EBSD study for the PA material deformed to 0.5 (a to c) and 1.5 strain (d to f) aged at 400°C in the CLSM. The CLSM snapshots at the critical time where visible boundary migrations stopped are given in Fig. 5.30 (a, d), the corresponding EBSD boundary maps after 60 min of ageing are given in Fig. 5.30 (b, e), while Fig. 5.30 (c, f) shows the superposition of the CLSM images with the isolated recrystallized grains.

For both strains, no grain boundary migrations could be observed after around 30 s of ageing at 400°C (Fig. 5.30 a, d). The EBSD boundary maps (Fig. 5.30 b, e) revealed strongly deformed microstructures with a small number of recrystallized grains. It was found that for both strains, the recrystallized area fraction in case of PA material was below 1% with average grain diameters of around 3.5 µm.

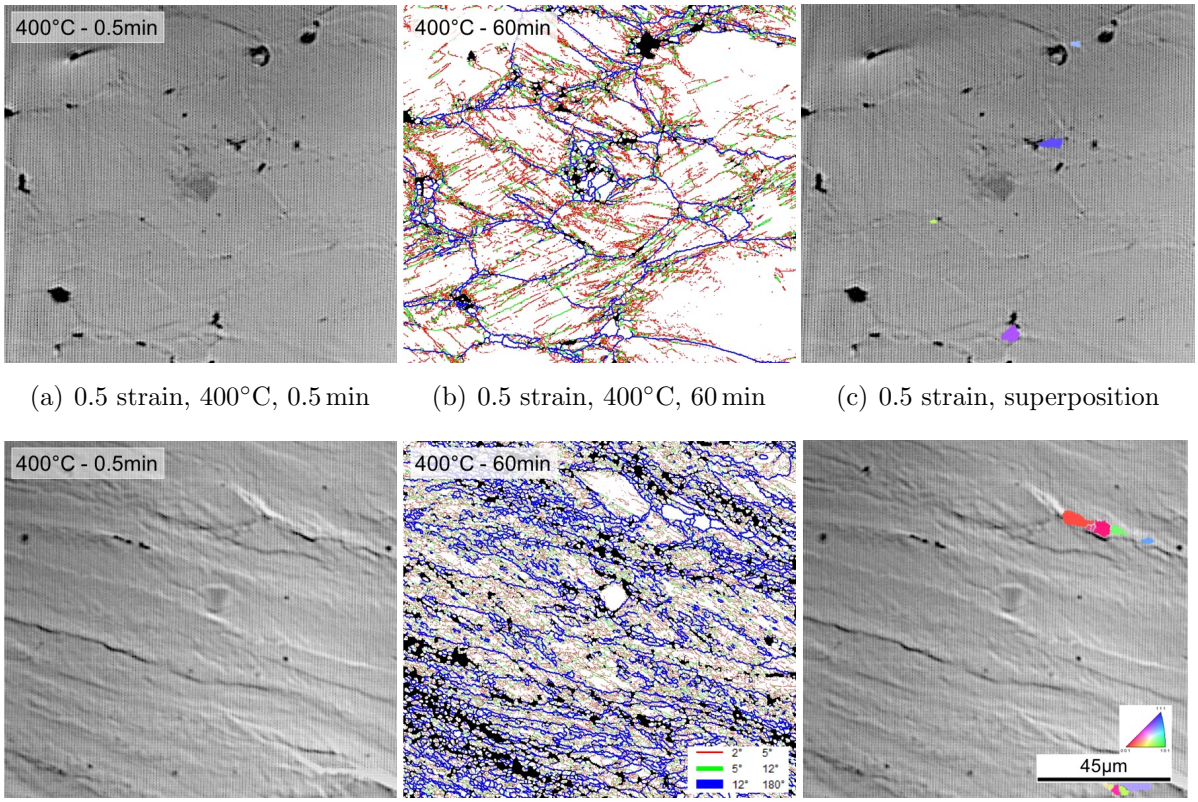

(a) 0.5 strain, 400°C, 0.5 min (b) 0.5 strain, 400°C, 60 min (c) 0.5 strain, superposition

(d) 1.5 strain, 400°C, 0.5 min (e) 1.5 strain, 400°C, 60 min (f) 1.5 strain, superposition

Fig. 5.30: Microstructure characterization of PA samples deformed to 0.5 (a, b, c) and 1.5 strain (d, e, f) aged at 400°C: In-situ CLSM snapshots (a, d) at the critical ageing time where visible microstructural modifications stopped. EBSD boundary maps after ageing for 400°C (b, e) of the same sample position as in (a, d) where strain-free grains (white) represent recrystallized grains. Superposition (c, f) of the CLSM image with the isolated recrystallized grains.

6 Discussion

The most important results of this study are discussed in this section. First, the strengthening mechanisms are summarized for the given Al-Mg-Sc-Zr alloy. Second, the different initial materials conditions are compared with respect to the presence and nature of the Al_3(Sc,Zr) phase and the degree of Sc-supersaturation. Third, the precipitation kinetics is derived regarding several process variables. Fourth, the in-situ CLSM methodology as well as the recrystallization kinetics are discussed in detail. Finally, recommendations for the production of a stringer made of belt-casted Al-Mg-Sc-Zr alloy are given based on the fundamental considerations of this study and additional literature sources.

6.1 Acting strengthening mechanisms

The relevant strengthening mechanisms for the given belt-casted Al-Mg4-Sc0.4-Zr0.12 alloy were solid solution, precipitation, and strain hardening. A grain size reduction did not influence the hardness of the material, as shown in Table 5.1. The influence of the Mg-content on the solid solution strengthening was not investigated as the concentration of Mg was not varied. The positive impact of Mg, however, was already demonstrated by Marquis *et al.* [18]. The most important strengthening contributions, precipitation and strain hardening, were both associated with the presence of secondary Al_3(Sc,Zr) phases. First, finely dispersed Al_3(Sc,Zr) precipitates oppose dislocation movement and significant precipitate strengthening was achieved, as demonstrated in section 5.2. Second, if present in a cold deformed microstructure, these phases inhibited recrystallization and recovery, thus maintaining the strain hardened microstructure to a certain extent (section 5.3). Third, if present before cold deformation, non-shearable particles increase the work hardening effect by generating dislocation loops and retarding dynamic recovery effects, as shown in [107]. However, a fundamental analysis of the effect of Al_3(Sc,Zr) precipitates on the strain hardening rate of Al-Mg-Sc-Zr alloys was not carried out in this work.

6.2 Degree of Sc-supersaturation

Three different materials conditions were considered in this study: as-cast (AC), electron-beam re-solidified (EBRS), and pre-aged (PA). As the grain size did not affect the materials properties, the most relevant differences were the presence and nature of Al_3(Sc,Zr) phases and the degree of Sc-supersaturation.

In AC condition, primary and eutectic Al_3(Sc,Zr) phases were present, while 0.13 wt.% of nominal 0.4 wt.% Sc was in solution. Accordingly, the solidification rate of the belt-caster used to produce AC material, i.e. around $30\,Ks^{-1}$, was not enough to prevent the formation of equilibrium Al_3(Sc,Zr) phases. This observation was in agreement with studies on rapid solidification of Al-Sc alloys, where solidification rates higher than $10^3\,Ks^{-1}$ were suggested to dissolve similar quantities of Sc [136–138]. In case of EBRS condition, only a marginal amount of primary Al_3(Sc,Zr) was detected leading to a much higher content of 0.37 wt.% Sc retained in solution. Apparently, the EBRS procedure with solidification rates of $10^4 - 10^5\,Ks^{-1}$ [141] was a suitable method to dissolve almost the entire nominal Sc-concentration of 0.4 wt.%, again in accordance with [136–138].

In PA condition, primary, eutectic, and secondary Al_3(Sc,Zr) were present. The secondary phases formed during pre-ageing at 325°C for 60 min. The presence of secondary Al_3(Sc,Zr) was not investigated using TEM, however, the higher hardness of PA (94 HV0.1) compared to AC (66 HV0.1) material confirmed the existence of strengthening phases. For PA material, it was assumed that the Sc-concentration retained in solution was negligible. The latter assumption was not confirmed with 100% certainty, but several observations in this study point in this direction. The precipitation hardening curve in Fig. 5.5 (b) showed that peak age condition was reached after around 120 min of ageing at 325°C. After 60 min of ageing, 95% of the maximal hardness were reached. However, the heating conditions for pre-ageing were not identical to that used for the detailed investigations on the hardening kinetics shown in Fig. 5.5 (b). For pre-ageing, the samples were put in the heated furnace having already reached 325°C, while for studying the precipitation kinetics, the furnace with the samples inside was heated to 325°C with $1°Cs^{-1}$. Consequently, the sample heating rate for pre-ageing was presumably higher than that leading to the hardening curves in Fig. 5.5. In section 6.3.3 it will be explained in detail, that higher heating rates result in faster precipitation kinetics. Possibly, the peak age condition was reached during pre-ageing at 325°C already after 60 min. After additional ageing at 400°C, no further hardening of PA samples was observed (Fig. 5.29). Accordingly, there was no solute Sc left for further precipitation, which supports the assumption that the solute Sc-concentration was negligible after pre-ageing.

6.3 Precipitation kinetics

A description of the precipitation kinetics is derived based on the results of hardness measurements, in-situ synchrotron XRD analyses, and the precipitate characterization. In addition, the precipitate radius r_t (Fig. 2.6) at which the transition from particle shearing to Orowan looping occurs, is estimated based on literature data.

6.3.1 Precipitate transition radius

The precipitate transition radius r_t is the relevant quantity to determine whether particle shearing or Orowan looping is the active precipitate-dislocation interaction mechanism. Since r_t is a function of the precipitate volume fraction f_V (Eqs. 2.7 to 2.18), it can be assumed that the value of r_t changes during the precipitation process and may also differ for AC and EBRS conditions. Therefore, the transition radii are estimated for a range of precipitate volume fractions considering an Al-Mg4 (wt.%) alloy with varying Sc-concentrations. The Zr-content is neglected due to an absence of proper data. The analysis follows an approach proposed by Seidman, Marquis *et al.* [18,38] for Al-(Mg)-Sc.

First, the precipitate strengthening effect of shearable particles is calculated as a function of the precipitate radius r for a range of volume fractions f_V considering modulus (Eq. 2.7), coherency (Eq. 2.8), and order strengthening (Eq. 2.10). Second, the Orowan strengthening effect is calculated as a function of r for the same f_V range (Eqs. 2.17 and 2.18). Finally, the intersection point of the strengthening curves for shearing and Orowan looping for a given precipitate volume fraction represent the respective transition radius r_t. The relevant materials constants in Eqs. 2.7, 2.8, 2.10, 2.17, and 2.18 have the following values [38]: $M = 3.06$, $\Delta G = 42.5\,\mathrm{GPa}$, $G = 25.4\,\mathrm{GPa}$, $b = 0.286\,\mathrm{nm}$, $m = 0.85$, $\alpha_\varepsilon = 2.6$, and $\nu = 0.34$. The magnitudes of these constants were derived for Al-Sc alloys, but should also hold for Al-Mg-Sc alloys with low Mg-concentration [18].

Modulus strengthening σ_m and coherency strengthening σ_c reach maximum values when the shearing dislocation is close to the Al_3Sc interface. Order strengthening σ_o, on the other hand, is a maximum when the dislocation has already sheared half the precipitate. Accordingly, the strengthening contributions to the shearing law do not reach their maximum strengthening effects at the same time and one has to assess which quantity, $\sigma_m + \sigma_c$ or σ_o, has a higher value. The calculated shearing stress is then taken as the higher one of the two strength maxima [38]. $\sigma_m + \sigma_c$ was calculated from Eqs. 2.7 and 2.8. The linear misfit strain ε (Eq. 2.8) depends on the lattice parameters of precipitate a_p and matrix a_m (Eq. 2.9). Based on literature data, Lee *et al.* [19] proposed that a_m

of α-Al depended linearly on the Mg-concentration in solution:

$$a_m = 4.048 + 0.00452 \cdot \text{Mg (wt.\%)}. \tag{6.1}$$

For a Mg-content of 4 wt.%, the matrix lattice parameter a_m equals 4.066 Å. With the Al_3Sc lattice parameter $a_p = 4.1$ Å [9], it followed that $\varepsilon = 0.00556$. According to Ardell [21] and others [18,38], the maximum order strengthening effect $\sigma_{o,max}$ is radius-independent and is calculated by:

$$\sigma_{o,max} = 0.81 M \frac{\gamma_{apb}}{2b} \left(\frac{3\pi f_V}{8} \right)^{1/2}. \tag{6.2}$$

With $\gamma_{apb} = 0.5\,\text{Jm}^{-2}$ [38], it followed that $\sigma_{o,max} = 136$ MPa for a precipitate volume fraction $f_V = 0.34\%$ (AC), and $\sigma_{o,max} = 204$ MPa for $f_V = 0.76\%$ (EBRS). The values for f_V correspond to the average measured values for AC (0.34%) and EBRS (0.76%) conditions after ageing at 325°C and 400°C for 180 min shown in Table 5.5 and Fig. 5.13 (a), respectively. Independent of the volume fraction, the value of $\sigma_m + \sigma_c$ exceeded that of $\sigma_{o,max}$ for precipitate radii larger than 0.8 nm. Consequently, the transition radius r_t was determined as the point of intersection of $\sigma_m + \sigma_c$ with the Orowan strength σ_{or}.

Fig. 6.1 shows the calculated strengthening effect for particle shearing ($\sigma_m + \sigma_c$) and Orowan looping for AC (a) and EBRS (b) conditions. The transition radius r_t equaled 1.95 nm for AC ($f_V = 0.34\%$) and 2.06 nm for EBRS ($f_V = 0.76\%$) conditions. The maximum precipitate strengthening effect at r_t increased from 186 MPa to 283 MPa by increasing the precipitate volume fraction from 0.34% to 0.76%. This result was in qualitative agreement to the significantly higher hardness values achieved for EBRS material compared to AC condition (Fig. 5.5).

The calculated values of r_t were in a similar range as other data presented in the literature [17,18,38], however, they seemed to be at the lower bound of this range. For a binary Al-Sc alloy, r_t equaled 2.1 nm at $f_V = 0.75\%$ [38], and for an Al-Mg-Sc alloy with 2 wt.% Mg, $r_t = 2.4$ nm at a volume fraction of 0.53% [18], which was slightly higher than the values presented in Fig. 6.1. The increase of r_t by adding Mg was explained by a reduced lattice misfit ε resulting from an increased matrix lattice parameter a_m. This statement is in good agreement to Eq. 6.1. Interestingly, it was not possible to recalculate the values of r_t [18,38] with the numbers given in the mentioned papers. Possibly, the deviation resulted of a different approach to determine the misfit parameter ε. Fazeli *et al.* [17] estimated r_t in a model to predict the strengthening effect of Al_3Sc. They fitted

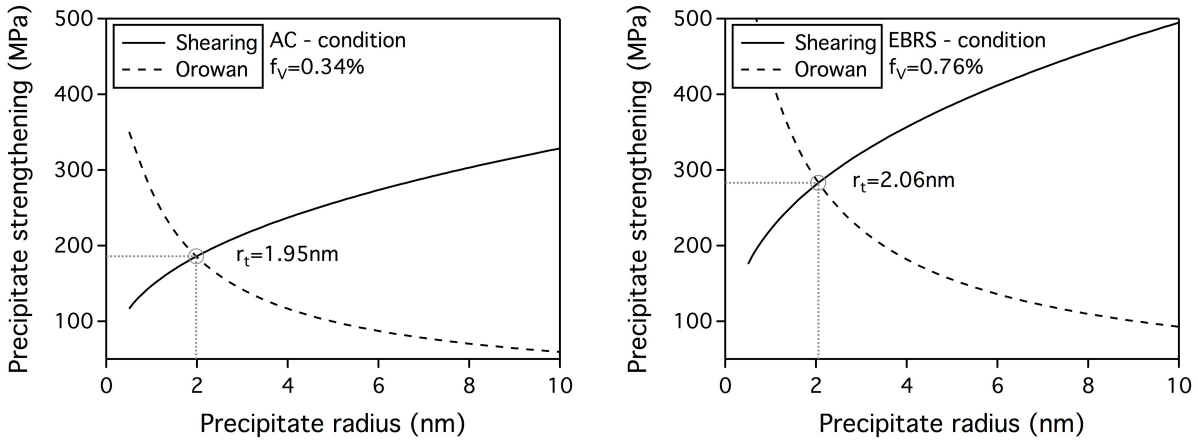

(a) Transition radius for AC condition

(b) Transition radius for EBRS condition

Fig. 6.1: Determination of the transition radius r_t from particle shearing to Orowan looping for AC (a) and EBRS (b) conditions.

the transition radius such, that the modelled hardening curves corresponded best to the experimental data. In that case, $r_t = 3.7\,\text{nm}$ for an Al-alloy containing 2.8 wt.% Mg and 0.16 wt.% Sc having a precipitate volume fraction of 0.45%. Compared to [18,38] and the values calculated in this study, this value seems to be at the upper bound of r_t.

Fig. 6.2 shows the evolution of the transition radius as a function of the Al_3Sc precipitate volume fraction for an Al-Sc and an Al-Mg4-Sc alloy. The values for the Al-Sc alloy were recalculated from [38]. For both alloys, the overview (Fig. 6.2 a) demonstrates a steady increase of r_t with increasing f_V, whereas the Mg-containing alloy presents higher values due to a decreased misfit strain ε, as discussed above. Fig. 6.2 (b) shows a detailed section up to a precipitate volume fraction of 1% indicating the transition radii of AC and EBRS samples after ageing at 325°C and 400°C for 180 min. When considering the precipitation process of EBRS samples, r_t increased from 1.86 nm at $f_V = 0.001\%$ to 2.06 nm at $f_V = 0.76\%$.

The measured precipitate radii of furnace annealed AC and EBRS samples equaled in average 3.6 nm after ageing at 325°C for 180 min, and 5.15 nm after ageing at 400°C for the same time (Fig. 5.12). Accordingly, the measured radii in peak age condition exceeded r_t, thus Orowan looping was the active precipitate-dislocation interaction mechanism in these materials conditions. During growth of the precipitates, on the other hand, it can be assumed that the precipitates were shearable over a long period of time. This assumption also considers, that the calculated r_t values shown in Figs. 6.1 and 6.2 represent lower bounds compared to literature, as discussed above.

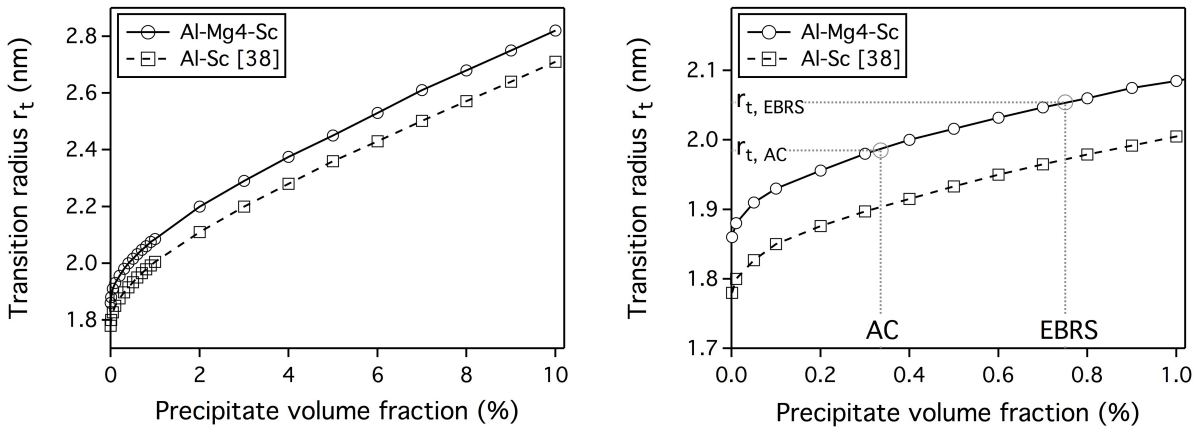

(a) Overview

(b) Detail of relevant section

Fig. 6.2: Transition radius r_t as a function of precipitate volume fraction estimated for an Al-Sc alloy [38] and an Al-Mg4-Sc alloy. Overwiew (a) and detail of the relevant range of volume fractions f_V (b) indicating AC and EBRS conditions.

6.3.2 Precipitation hardening

Figs. 5.5 and 5.6 showed that the hardness due to precipitation was significantly influenced by the ageing temperature and the degree of Sc-supersaturation of up to 0.37 wt.%. After 180 min of ageing at 325°C and 400°C, the measured precipitate radii ranged from 3.2 to 5.2 nm (Table 5.5) and Orowan looping was the active precipitate-dislocation interaction mechanism.

Costa *et al.* [80] studied different lab-scale Al-Sc alloys with 0.5 wt.% to 0.7 wt.% Sc in solid solution, showing a strong dependency of the ageing temperature on the hardening behavior. The amount of Sc in solution, on the other hand, did not influence the hardness. When considering Fig. 5.6 (c) in this context, it can be observed that the hardening potential per wt.% Sc decreased with the degree of Sc-supersaturation. This behavior is shown by the flatter slope of the curve at higher Sc-content in solution. The Orowan strength, or hardness HV, depends on the reciprocal inter-particle spacing λ between Al_3(Sc,Zr) precipitates (Eq. 2.13):

$$HV \propto \frac{1}{\lambda}. \tag{6.3}$$

The inter-particle spacing λ relates to the reciprocal square root of the number density of obstacles in the slip plane n_s (Eq. 2.14). The precipitate size distributions were independent of the precipitate volume fraction for a given ageing temperature, as shown in

Figs. 5.12 and 5.13. For a constant precipitate size distribution, n_s is proportional to the volume fraction f_V (Eq. 2.15 and [38]), thus the hardness increment for a given ageing temperature HV_T reads:

$$HV_T \propto \sqrt{n_s} \propto \sqrt{f_V}. \tag{6.4}$$

Finally, Fig. 5.13 showed a linear dependency of the precipitate volume fraction and number density with the degree of Sc-supersaturation. Accordingly, the hardness increment for a given ageing temperature related to the square root of the Sc-content in solution:

$$HV_T \propto \sqrt{\text{Sc (wt.\%)}}. \tag{6.5}$$

As a result of this square root relation, it can be expected that the hardening potential per wt.% Sc will be further reduced when increasing the Sc-content in solution to values higher than 0.4 wt.%. For a Sc-content of 0.37 wt.% (EBRS), peak ageing could be achieved after ageing at 325°C for 180 min, leading to a maximal hardness increase of around 70%. Higher hardness might be achieved by reducing the ageing temperature and extending the ageing time, as shown for binary Al-Sc alloys [80].

Fig. 6.3 summarizes the influence of the degree of Sc-supersaturation, ageing temperature, and heating rate on the precipitation hardening behavior. The hardness increment was more pronounced for the higher solute Sc-content (Fig. 6.3 a), as discussed in detail above. The influence of the annealing temperature was already shown for the samples annealed in the furnace. In addition, Fig. 6.3 (b) shows the hardness evolution in non-deformed (ND) material of AC samples annealed in the dilatometer. Precipitation hardening was most pronounced for the sample annealed at 325°C, whereas the hardness increment was reduced with increasing temperature. Similar to the furnace annealed samples and in agreement with studies on lab-scale alloys [38,86], this observation was attributed to a rapidly reducing driving force for nucleation and high precipitate growth rate at higher temperature. In consequence, a smaller amount of larger precipitates was formed at higher temperature. Finally, Fig. 6.3 (c) shows the influence of the heating rate on the hardness of AC samples annealed at the same temperature. The heating rate of $1°Cs^{-1}$ refers to furnace annealing, while the heating rate of $5°Cs^{-1}$ relates to dilatometer annealing. In Fig. 6.3 (c), the ageing temperature was 400°C, however, the observations discussed hereafter were consistent for all other temperatures investigated in this study. For a heating rate of $1°Cs^{-1}$, the hardness increase occurred later in time

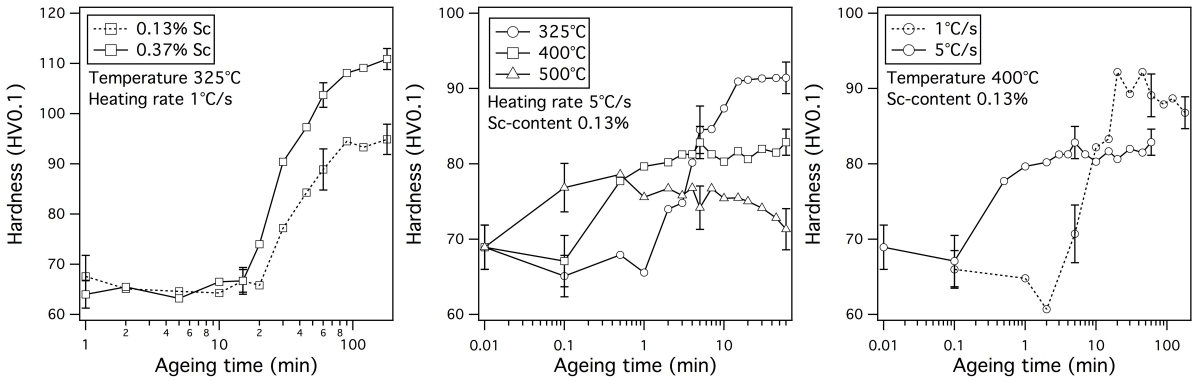

(a) Influence of Sc-content (b) Influence of temperature (c) Influence of heating rate

Fig. 6.3: Influence of the solute Sc-content (a), the ageing temperature (b), and the heating rate (c) on precipitation hardening.

compared to a higher heating rate of $5\,°Cs^{-1}$. The maximal measured hardness was higher for the lower heating rate but this peak-age condition was reached after a longer period of ageing time. In agreement with Deschamps *et al.* [44], both observations could be attributed to the higher driving force for nucleation at lower heating rate leading to a larger number of smaller precipitates.

6.3.3 Quantification of precipitation kinetics

The precipitation kinetics of strengthening phases in multi-component alloy systems is often modeled using commercial or self-written algorithms, simply because the influencing factors are too complex and interdependent to even estimate the kinetics by hand. The interested reader is referred to a textbook by Kozeschnik [35], where the fundamentals of precipitation modeling are explained in detail. There are several papers available reporting on the precipitation behavior of Sc-containing Al-alloys using predictive models to calculate the precipitate volume fraction, number density, and size distribution as a function of chemical composition, ageing temperature, and time [41,84,95,167,168]. On the other hand, there exist studies [42,169] where the precipitation kinetics in terms of precipitate volume fraction was estimated by fitting the JMAK equation (Eq. 2.28) to experimental data. In this section, it is intended to estimate the precipitation kinetics based on experimental results by using JMAK fits. These fits are used to analyze several influencing factors, to compare the given industrial alloy to literature data on binary Al-Sc alloys, and as a basis for further analyses on the recrystallization behavior.

The evaluation of the peaks from in-situ synchrotron XRD measurements in Fig. 5.7 showed that no other phases than Al_3(Sc,Zr) formed during isothermal ageing. This observation was in good agreement to HR-STEM and EFTEM measurements where a fine distribution of Al_3(Sc,Zr) precipitates was found. Furthermore, the temporal evolution of the Al_3(Sc,Zr) XRD peak showed good correlation to the corresponding hardening curve (Fig. 5.9). Taking all these results into consideration, the analysis of the precipitation kinetics using the JMAK relationship based on the hardness evolution is sensible.

6.3.3.1 Furnace annealed samples

Fig. 6.4 shows the JMAK analysis of furnace annealed samples based on the hardness curves shown in Fig. 5.5. The hardness values in Fig. 6.4 (a) were normalized according to Eq. 5.1 and fitted using Eq. 2.28. Based on the in-situ XRD analysis, the evolution of the normalized hardness values was considered as the normalized Al_3(Sc,Zr) precipitate volume fraction. The shapes of the curves in Fig. 6.4 (b) were similar for AC and EBRS samples at a given temperature. However, for either temperature, the precipitation was slightly faster for the EBRS sample with 0.37 wt.% Sc in solution due to the larger driving force for precipitation in case of a higher degree of supersaturation. Similar behavior was reported in previous studies on lab-scale Al-Sc materials [9,83]. At 325°C, the JMAK fits revealed a steeper incline than that at 400°C expressed by higher n-values (Table 6.1). On the other hand, the k-values were lower for the JMAK curves at 325°C compared to 400°C. In general, larger n-values correspond to a stronger influence of nucleation events on the transformation process, whereas larger k-values are associated with higher

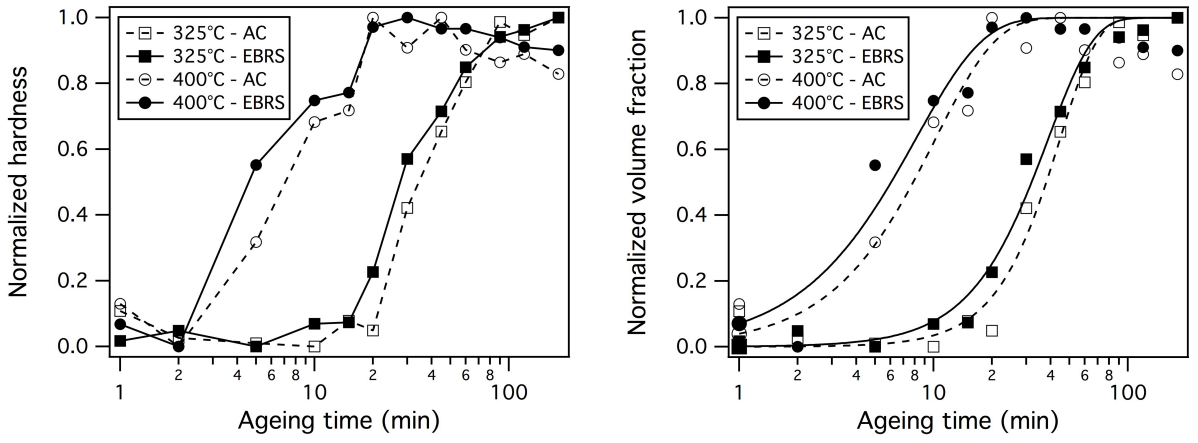

(a) Normalized hardness evolution

(b) Normalized precipitate volume fraction

Fig. 6.4: Normalized hardness evolution (a) and JMAK fits (b) of the normalized hardness during ageing of AC and EBRS samples at 325°C and 400°C for up to 180 min.

Table 6.1: JMAK coefficients k and exponents n for the precipitation kinetics analysis of AC and EBRS samples aged in a furnace at 325°C and 400°C.

Temperature (°C)	Condition	Sc in solution (wt.%)	k	n
325	AC	0.13 ± 0.02	0.0002	2.23
	EBRS	0.37 ± 0.03	0.0011	1.85
400	AC	0.13 ± 0.02	0.0404	1.38
	EBRS	0.37 ± 0.03	0.0735	1.25

growth rates [35]. This behavior was in agreement with the TEM measurements where a larger amount of smaller precipitates was observed for ageing at 325°C compared to 400°C (Figs. 5.12 and 5.13).

The n-values in Table 6.1 were in agreement with the JMAK exponents reported for continuous precipitation in a binary Al-0.2Sc alloy [42]. There, the n-value equaled 1.8 in a temperature range between 275°C and 325°C, and 1.3 between 375°C and 450°C. The values found for n in this study and reported in [42] indicate a precipitation mechanism close to nucleation site saturation [9]. The term nucleation site saturation in the context of homogeneous nucleation refers to a situation, where the nuclei are formed in a short period of time, followed by a fast reduction of the nucleation rate while the existing nuclei grow. Similar behavior was reported by Robson [167], who demonstrated a model to predict the number density, size, and volume fraction of Al_3(Sc,Zr) during precipitation. He found that the precipitate number density increased rapidly in the early stages of transformation as a result of a high nucleation rate. With reduced supersaturation in the matrix, the nucleation rate dropped and the number density remained at a constant level until coarsening was initiated. It was concluded, that the nucleation rate decreased more sharply than the growth rate as the supersaturation decreased. During ageing of a 7050 alloy modified with 0.18 wt.% Sc and 0.13 wt.% Zr at 480°C, for example, it was found that the equilibrium volume fraction of Al_3(Sc,Zr) precipitates was reached after around 30 min, while the number density reached its maximal value already after less than 5 min. In consequence, the precipitate number density remained constant for the larger part during growth [167].

The good agreement of the JMAK parameters found in this study with the JMAK and modeling data found in literature support the hypothesis that the precipitation kinetics can be assessed directly using precipitation hardening curves. Furthermore, it was concluded that the precipitation kinetics of the industrial Al-Mg-Sc-Zr alloy studied in this work does not differ considerably of that of high-purity lab-scale Al-Sc alloys.

6.3.3.2 Dilatometer annealed samples

Fig. 6.5 (a) shows the normalized Al_3(Sc,Zr) precipitation kinetics of AC samples annealed in a dilatometer at 325°C, 400°C, and 500°C for 60 min. The curves represent JMAK fits of the normalized hardness evolution of non-deformed (ND) material shown in Fig. 5.15. The vertical dashed line represents the end of the 1 min heat-up stage, which corresponds to a heating rate of around $5°Cs^{-1}$. At 500°C, precipitation occurred already during the heating stage leading to a normalized precipitate fraction of 0.8 prior to isothermal ageing. The JMAK equation was derived for isothermal ageing and, in fact, does not consider heating or cooling processes [35,39]. Striktly speaking, JMAK is not suitable for any ageing treatments, as the samples are not heated instantaneously. This is commonly neglected, because the influence of the heating cycle is often very little. For the sample dilatometer-annealed at 500°C, however, it is noteworthy that using the JMAK equation represents only a rough estimation of the kinetics. The sample annealed at 400°C showed a normalized Al_3(Sc,Zr) precipitate volume fraction of 0.15 after heating, while the curve representing ageing at 325°C revealed no increase in precipitate volume fraction.

Similar to Fig. 6.4, the JMAK curves in Fig. 6.5 (a) were shifted to shorter ageing times with increasing temperature. Accordingly, the coefficient k increased significantly the higher the annealing temperature. The exponent n was similar for all temperatures revealing values of around 1.1 (Table 6.2). The values determined for n were lower, while the k values were higher than the values observed for furnace annealing (Table 6.1). This difference must be related to the considerably higher heating rates used in the dilatometer. Apparently, even for the sample annealed at 325°C, some nucleation occurred already during the heating stage. The driving force for further nucleation during isothermal ageing was then reduced due to reduced supersaturation, leading to growth of existing nuclei. Low nucleation and high growth rates are in general associated with low n and high k values [35,45].

Fig. 6.5 (b) shows faster kinetics in case of a heating rate of around $5°Cs^{-1}$ (dilatometer) compared to $1°Cs^{-1}$ (furnace). A higher heating rate not only results in faster kinetics but influences the size and number of Al_3(Sc,Zr) precipitates. For a given annealing temperature, larger precipitate radii and smaller number densities are attained the higher the heating rate is [44]. Verifying this conclusion, Fig. 6.3 (c) showed a lower hardness for the sample heated-up with a higher heating rate.

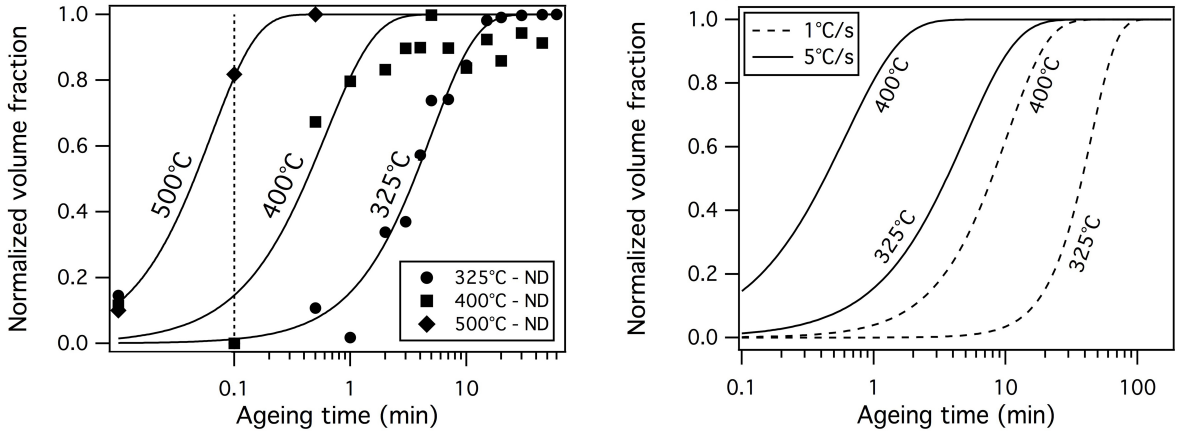

(a) Dilatometer annealed AC (ND) material

(b) Influence of the heating rate

Fig. 6.5: JMAK fits of non-deformed (ND) AC material aged in a dilatometer at 325°C, 400°C, and 500°C (a). Vertical dashed line represents end of 1 min heat-up stage. Influence of the heating rate on the precipitation kinetics (b) of samples annealed in a furnace ($1°Cs^{-1}$) and dilatometer ($\sim 5°Cs^{-1}$).

Table 6.2: JMAK coefficients k and exponents n for the precipitation kinetics analysis of AC samples aged in a dilatometer at 325°C, 400°C, and 500°C.

Temperature (°C)	Condition	Sc in solution (wt.%)	k	n
325	AC	0.13 ± 0.02	0.17	1.1
400	AC	0.13 ± 0.02	1.66	1.0
500	AC	0.13 ± 0.02	20.8	1.1

6.3.4 Analysis of Al_3(Sc,Zr) precipitates

The AC and EBRS samples aged at 325°C and 400°C for 180 min were analyzed in detail by various TEM techniques. These analyses revealed a homogeneous distribution of spherical, coherent Al_3(Sc,Zr) precipitates. Similar to investigations on lab-scale alloys, e.g. [9,85], and in good agreement with a model proposed by Robson *et al.* [41], no preferred nucleation at dislocations or grain boundaries was observed for the investigated Sc-supersaturations and ageing temperatures. Several studies, e.g. [44,95,99], reported on a heterogeneous element distribution in Al_3(Sc,Zr) precipitates, i.e. a Sc-rich core and a Zr-rich shell. In the present work, a visible core-shell structure was not observed. However, in contrast to the mentioned studies, the research focus in this work was not put on the precipitate morphology evolution during ageing, thus the Al_3(Sc,Zr) morphology was not investigated with enough depth to make a clear statement.

6.3.4.1 Precipitate size

As shown in Fig. 5.12, the mean precipitate radius after 180 min of ageing was not significantly affected by the Sc-supersaturation prior to ageing and increased from around 3.5 nm at 325°C to roughly 5 nm at 400°C. These results are difficult to compare with existing literature due to the general lack of investigations focusing on short ageing times. In addition, the precipitate size is strongly influenced by the nucleation and thus the heating rate, which differs considerably from one study to another. However, when extrapolating data published on binary Al-Sc alloys [86] to shorter ageing times, the precipitate radii are in a similar range as in the present study. The results shown in Fig. 5.12 are also comparable to [9], where precipitate sizes in the range of 2 to 6 nm were reported for samples aged between 250°C and 350°C. Hence, the precipitate radii shown for the industry-scale belt-casted Al-Mg-Sc-Zr alloy were in a similar range as in lab-scale Al-Sc alloys.

6.3.4.2 Volume fraction

Peak ageing was achieved after 20 min for the samples aged at 400°C and after 120 min for the samples aged at 325°C in the furnace. In peak-age condition, the Al_3(Sc,Zr) volume fraction corresponded to the equilibrium state, as confirmed by the coinciding measured volume fractions (EFTEM) with the theoretical limit in Fig. 5.13 (a). The findings from EFTEM measurements are compared to atom probe tomography (APT) [97,165] and small-angle X-ray scattering (SAXS) [44] studies, since there are no papers available showing similar results using TEM. The results from [44,97,165] are represented in Fig. 5.13 (a) by individual data points. The measurements from Knipling *et al.* [97] correlate to peak ageing at 400°C of an Al-0.1Sc-0.1Zr (at.%) alloy. The APT results reported by Vo *et al.* [165] relate to peak ageing of a friction stir processed Al-Mg4.1-Sc0.47-Zr0.022 (wt.%) alloy at 290°C. Deschamps *et al.* [44] investigated an Al-0.16Sc-0.1Zr (wt.%) alloy at 450°C. These results included in Fig. 5.13 (a) underpin the findings shown in this study: The solid solubility of Sc in α-Al can be neglected up to a temperature of 400°C, since only the results for ageing at 450°C [44] showed a reduced volume fraction compared to the theoretical limit at room temperature. Furthermore, it is demonstrated that the precipitate volume fraction is independent of the Mg-content. The precipitation of Al_3(Sc,Zr) is driven primarily by the Sc-content, while the influence of Zr on the volume fraction is limited by the generally low Zr-contents. For illustration of the relative importance of Sc compared to Zr, the theoretical equilibrium precipitate volume fraction of an Al-Mg4-Sc0.4-Zr0.12 alloy is only around 10% larger than that of an Al-Mg4-Sc0.4 alloy assuming Sc and Zr are fully interchangeable.

6.3.4.3 Number density

The precipitate number density is the dominant factor to determine the total strength of an age hardened material with homogeneous precipitate distribution, as it denotes nothing less than the number of obstacles for dislocation movement. Consequently, the highest overall hardness was measured for the sample in peak-age condition with the largest number of Al_3(Sc,Zr) precipitates, i.e. the smallest inter-particle spacing λ (Eqs. 2.17 and 2.18). This maximal hardness and number density was achieved for the EBRS sample aged at 325°C, as shown in Fig. 5.6 and Fig. 5.13. The Sc-diffusion in Al at 325°C was slower than at 400°C, leading to more nucleation events and slower growth rates which resulted in a larger amount of smaller precipitates. Consequently, the maximum hardness was higher at 325°C than at 400°C for a given amount of Sc in solution.

The AC sample aged at 325°C had a hardness of 95 ± 3.0 HV0.1 and the EBRS sample aged at 400°C a hardness of 104 ± 2.1 HV0.1 after ageing for 180 min. Despite their different hardness values, these two samples had roughly the same precipitate number density (Fig. 5.13 b). In both cases, Orowan strengthening was the active precipitate-dislocation interaction mechanism, thus the strength depended on the reciprocal inter-particle spacing λ (Eq. 2.17). When calculating λ (Eq. 2.18) using the values for f_V and r from Table 5.5, $\lambda = 91$ nm for the AC sample aged at 325°C, and $\lambda = 82$ nm for the EBRS sample aged at 400°C. These calculations support both the hardness and TEM measurements.

6.3.4.4 Evolution of precipitates

Fig. 6.6 summarizes schematically the evolution of Al_3(Sc,Zr) precipitates during ageing at 325°C (a to d) and 400°C (e to h). The chronological sequence is based on the JMAK analysis obtained for the AC samples annealed in a furnace for 180 min, and considers literature data [9,42,167]. The precipitation process of Al_3(Sc,Zr), in general, was characterized by fast nucleation in the first minutes, followed by growth of the existing precipitates, as shown by the JMAK parameters in Table 6.1 in accordance with [9,167]. At 325°C, nucleation was comparably slow and the growth stage started after around 10 min. Due to the low temperature, a large number of nuclei was formed (Fig. 6.6 b). After 30 min of ageing at 325°C (c), the volume fraction increased to roughly 50% of the maximum, whereas the increase in volume fraction resulted predominantly from the growth of existing nuclei. The equilibrium volume fraction was reached after around 120 min due to precipitate growth, and this precipitate state was unaltered until the end of the heat treatment (d). At 400°C, nucleation occurred in a shorter period of time

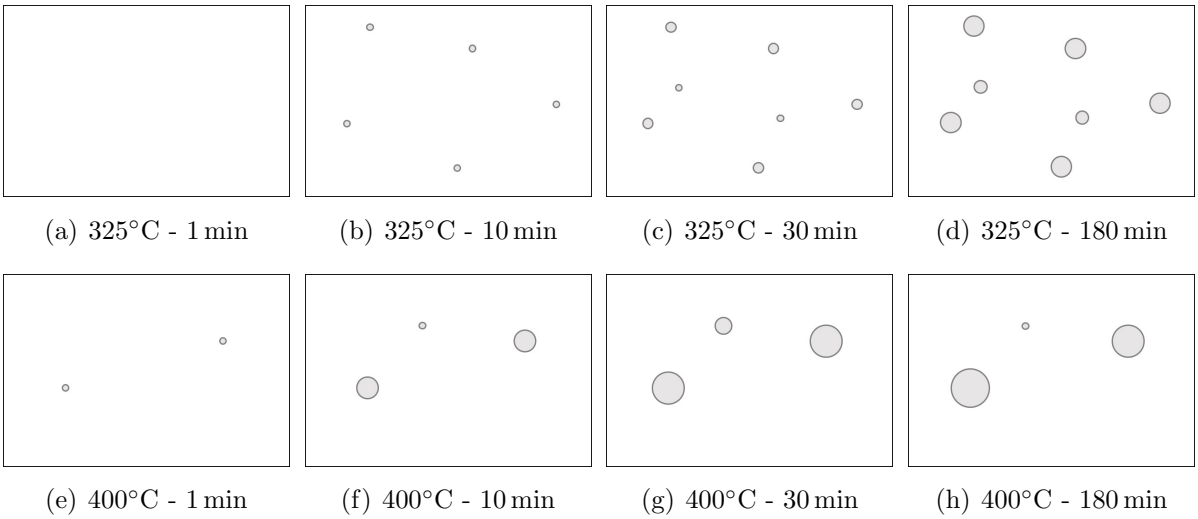

(a) 325°C - 1 min (b) 325°C - 10 min (c) 325°C - 30 min (d) 325°C - 180 min

(e) 400°C - 1 min (f) 400°C - 10 min (g) 400°C - 30 min (h) 400°C - 180 min

Fig. 6.6: Schematic evolution of Al_3(Sc,Zr) precipitates during ageing of AC samples at 325°C (a to d) and 400°C (e to h) for 180 min.

(Fig. 6.6 e). A smaller amount of nuclei was formed compared to 325°C, resulting from a reduction of the driving force for nucleation due to rapid reduction of Sc-supersaturation at higher temperature. Precipitate growth started earlier in time and after 10 min a normalized volume fraction of around 0.65 was reached. Again, precipitate growth was the dominant transformation mechanism. The equilibrium volume fraction was reached after 30 min (Fig. 6.6 g), and slight precipitate coarsening occurred until the end of the heat treatment (h). The behavior of the EBRS samples was similar to that of the AC samples, however, the kinetics was shifted to slightly shorter times and the number of precipitates was around 2 times higher.

6.4 Recrystallization kinetics

The in-situ CLSM approach to study the recrystallization kinetics was used for the first time in this study. Therefore, first the applied methodology is discussed and compared to other available methods. Afterwards, the behavior of deformed material in an annealing process is analyzed in detail, focusing on the influence of plastic deformation, temperature, and precipitate state. In particular, the quantitative description of the isolated softening kinetics as well as the estimation of driving pressure and Zener pinning effect are derived and compared to the microstructural investigations.

6.4.1 In-situ CLSM method

The CLSM approach presented in this study is especially suitable when investigating the recrystallization behavior of a novel age hardening alloy with rather unknown kinetics. Classicaly, such a problem is studied as alternating series of heat treatments and microstructural investigations, requiring a large amount of microstructure characterizations for every single combination of temperature and strain. If the recrystallization kinetics do not follow the JMAK relation, as it is the case when precipitation and recrystallization occur simultaneously, the kinetics can not be estimated and the amount of microstructural investigations increases further. Using the proposed in-situ CLSM approach, in contrast, with just one single experiment per strain and temperature, it is possible to determine the temporal and local sequences of recrystallization even for non-constant growth rates. The benefits of this approach are even more pronounced when considering investigations over longer periods of time. Measurements of the grain structure using standard EBSD is recommended to validate the observations from CLSM, while TEM and EFTEM investigations are necessary for the analysis of the precipitates. The correlation of the recrystallization phenomena between surface and bulk was proved to be good enough for the tested alloy in the investigated parameter range. A proper estimation of the materials behavior could be made in terms of recrystallized area fraction, and size and location of recrystallized grains.

Most available methods to study recrystallization in-situ investigate phenomena related to recrystallization rather than directly observing the microstructure evolution. By using high precision dilatometry [170], for example, the recrystallized volume fraction was studied as a function of time for high purity ultrafine-grained Ni. The measurement was based on the length change of the samples resulting from the release of free volume during recrystallization. There are no similar studies for alloys with several components and phases, as it is probably a very difficult task to isolate the signal responsible for recrystallization in complex alloys. Differential scanning calorimetry (DSC) was successfully applied [171] to study the recrystallization behavior of pure copper during heating with different heating rates. By measuring the exothermic peak associated with the release of stored energy, the recrystallization kinetics was studied as a function of temperature during heating. However, recrystallization during isothermal ageing can not be studied by DSC, since the measurement itself requires a steady temperature increase over time. In DSC studies on commercial 2014 Al-Cu alloy [172] or Al-Mg12 [173], the signals corresponding to recrystallization could not be isolated due to overlapping effects of precipitate formation and recrystallization. Similar behavior can be expected for the

Al-Mg-Sc-Zr alloy used in this study where precipitation and recrystallization occur in a similar temperature range. Using in-situ X-ray diffraction (XRD), the appearance of reflections can be observed during ageing which is a measure for recrystallization in deformed alloys [174,175]. A synchrotron source is required for such a complex experiment to facilitate time-resolved analyses. The local sequence of recrystallization can not be followed with any of the discussed methods.

The only currently available method to observe the microstructure evolution during recrystallization is the use of EBSD combined with a heating stage in a scanning electron microscope. Field *et al.* [163] investigated the recrystallization behavior of commercially pure Cu in-situ using high temperature EBSD. They collected EBSD patterns every 3 min since the scan time equalled $2-3$ min for the investigated 18×18 µm area. This approach could be employed up to a temperature of 175°C, when the recrystallization kinetics was much slower than the scan time. The in-situ EBSD results are striking for the used material but the method itself is only applicable if the evolution kinetics is very slow and the investigated area is in the range of only a few microns. A quasi in-situ approach was presented by Bozzolo *et al.* [176,177] who studied the recrystallization behavior of different materials using a sample stage with heating and cooling rates of up to $175°Cs^{-1}$. Several temperature cycles consisting of annealing at the target temperature followed by cooling to room temperature for EBSD data acquisition allowed to visualize the recrystallization kinetics of the investigated materials stepwise. A comparable approach was presented by Yamamoto *et al.* [178] who investigated the recrystallization kinetics of Al-Mg-Si alloys using cycles of annealing and EBSD measurements of the same sample position. However, in case of investigating several annealing temperatures on a large sample area over long periods of time, the stepwise EBSD method is expected to be rather time consuming.

Compared to the in-situ or quasi in-situ methods explained above, the CLSM approach presented in this work has several advantages and some disadvantages. The in-situ CLSM method itself is a straightforward approach, is easy to apply, and requires only simple data interpretation. The recrystallization process can be observed directly on a surface area of hundreds by hundreds of microns and the start and end of the transformation can be determined. The experimental effort is reduced to only one single experiment that needs to be carried out for every combination of temperature and strain. On the other hand, it was shown that the resolution is limited and that grains in the range of only a few microns are not clearly detectable. Furthermore, the CLSM approach is only useful if the recrystallization kinetics is slow enough to observe boundary migrations.

The precision of the methodology is lower compared to EBSD and is not suitable to study detailed recovery kinetics.

In summary, the proposed in-situ CLSM approach employed in this work is a very suitable method to roughly characterize the recrystallization kinetics of alloys that exhibit recrystallization and precipitation in a similar temperature regime.

6.4.2 Softening of deformed samples

In the current context, softening refers to the reduction of hardness due to the restoration of an initially cold deformed microstructure in an annealing treatment. Both, softening due to recrystallization or recovery, and hardening from Al_3(Sc,Zr) precipitates, occurred simultaneously during annealing of deformed AC samples, as shown in Figs. 5.15, 5.20, 5.23, and 5.24. According to various authors [9,41,82], the precipitation kinetics in Al-Sc alloys is not affected by the degree of plastic deformation within the regimes of Sc-content and temperature considered in this study. This statement is in good agreement with the hardness measurements shown in Fig. 5.15, where the end of the incubation time was identical for deformed and non-deformed (ND) material at a given temperature. The same applies regarding the time period to achieve the maximum hardness. In consequence, the Al_3(Sc,Zr) precipitate state for a given Sc-concentration and heating rate depended only on the ageing temperature and time. The JMAK analysis of the dilatometer-annealed samples shown in Fig. 6.5 (a) is valid for both deformed and non-deformed materials for a given temperature.

In this section, the connection between strain hardening, precipitation hardening, and softening is discussed in detail. Fig. 6.7 shows a schematic illustration of the full process of sample preparation, cold deformation, and dilatometer annealing for the AC and PA samples deformed to 0.5 strain prior to annealing at 400°C for 60 min. For each of the processing steps, the respective sample hardness is shown. In addition, the hardness difference compared to the previous step resulting from hardening or softening phenomena is displayed. The process starts with the non-deformed (ND) AC sample with a hardness of 69 HV0.1. By ageing at 325°C for 60 min, the hardness was increased by 25 HV0.1 due to precipitation of Al_3(Sc,Zr). The resulting materials condition was the non-deformed pre-aged (PA) one, with a hardness of 94 HV0.1. The second process step was cold deformation to a strain of 0.5. The hardness of the AC sample increased by 30 HV0.1 to a value of 99 HV0.1 due to strain hardening. The strain hardening increment for the PA sample, on the other hand, equalled only 19 HV0.1, resulting in a hardness value of the PA (D) sample of 113 HV0.1. A reduced strain hardening increment in the

particles-containing condition was not expected [107]. However, this somewhat unusual behavior was not further investigated, as the main intention was to analyze the influence of $Al_3(Sc,Zr)$ precipitates on the softening kinetics. The third step, annealing in a dilatometer at 400°C for 60 min, promoted precipitation hardening and softening due to restoration of the deformed microstructures. For the AC (D) sample, the precipitation hardening increment equalled 14 HV0.1 (Fig. 5.15 b). The hardness decrement, mainly due to recrystallization (Fig. 5.23 c to e), equalled 28 HV0.1 to achieve a final hardness of 85 HV0.1. In contrast, no precipitation hardening occurred for the PA (D) sample and a hardness reduction of 21 HV0.1 was measured due to annealing, as shown in step 3 of Fig. 6.7. Since hardly any recrystallization occurred in PA condition (Fig. 5.30), the softening from 113 HV0.1 to 92 HV0.1 resulted mainly from recovery.

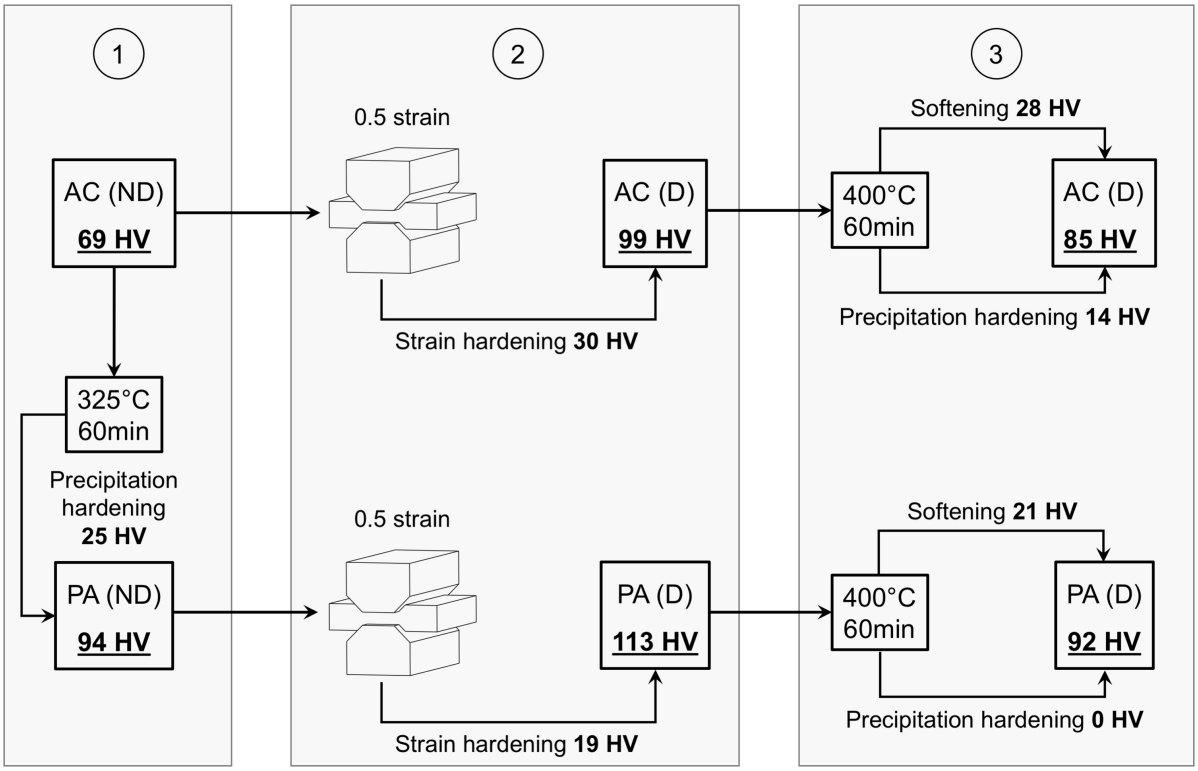

Fig. 6.7: Schematic illustration of the full process of sample preparation (1), cold deformation to 0.5 strain (2), and dilatometer annealing (3) at 400°C for 60 min for AC and PA samples. The schematic flow chart shows the influence of each processing step on the respective hardness considering precipitation and strain hardening as well as softening due to restoration.

Table 6.3 gives an overview of the hardness values of deformed materials before and after 60 min of ageing as well as the corresponding hardness contributions for all investigated AC and PA samples. The calculation of the individual hardness contributions is schematically illustrated in Fig. 6.8 and was carried out as follows:

$$HV_{D,red} = HV_{D,0} - HV_{D,60} \tag{6.6}$$

$$HV_{prec} = HV_{ND,60} - HV_{ND,0} \tag{6.7}$$

$$HV_{D,soft} = HV_{D,red} + HV_{prec}. \tag{6.8}$$

The acronyms in Table 6.3 and in Eqs. 6.6 to 6.8 have the following meaning: $HV_{D,0}$ is the initial hardness of the deformed samples corresponding to step 2 in Fig. 6.7. $HV_{D,60}$ is the hardness after 60 min of ageing (Step 3 in Fig. 6.7). $HV_{D,red}$ is the corresponding total hardness reduction between step 2 and 3. HV_{prec} is the hardness contribution from precipitates (Step 3) measured in non-deformed (ND) material. $HV_{D,soft}$ is the hardness reduction due to softening of the deformed microstructure during annealing in step 3. The value $\Delta\,HV_i$ (Fig. 6.8 a) is the hardness difference between deformed and non-deformed material at a given time step and will be introduced in detail in section 6.4.4.

Table 6.3: Summary of initial hardness ($HV_{D,0}$), hardness after 60 min of ageing ($HV_{D,60}$), corresponding total hardness reduction ($HV_{D,red}$), hardness increment due to precipitation (HV_{prec}), and hardness reduction due to restoration processes ($HV_{D,soft}$) at various temperatures for AC and PA samples deformed to 0.5 and 1.5 strain.

Condition	Strain ( )	Temperature (°C)	$HV_{D,0}$	$HV_{D,60}$	$HV_{D,red}$	HV_{prec}	$HV_{D,soft}$
AC	0.5	325	99	96	3	22	25
		400		85	14	14	28
		500		73	26	3	29
AC	1.5	325	111	102	9	22	31
		400		90	21	14	35
		500		77	34	3	37
PA	0.5	400	113	92	21	0	21
	1.5	400	123	93	30	0	30

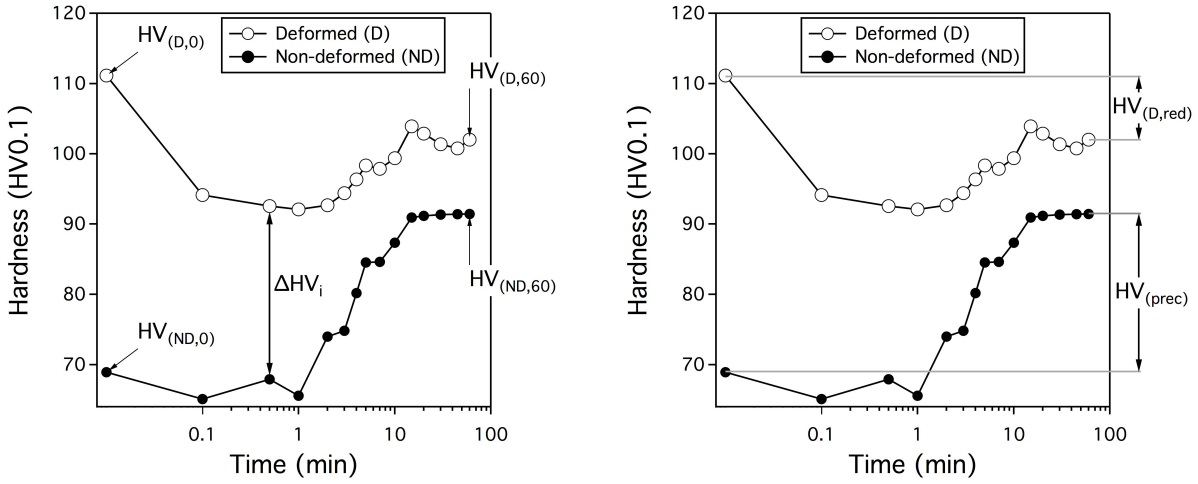

(a) Initial and final hardness values

(b) Calculation of hardness contributions

Fig. 6.8: Schematic illustration of the calulation of individual hardness values from the hardness curves of deformed (D) and non-deformed (ND) materials upon dilatometer annealing. Initial (index 0) and final (index 60) hardness values and difference between D and ND material ($\Delta\,\mathrm{HV}_i$) (a). Calculation of precipitation hardening increment ($\mathrm{HV}_{\mathrm{prec}}$) and total hardness reduction of deformed material ($\mathrm{HV}_{\mathrm{D,red}}$) (b). Curves correspond to the sample heat treated at 325°C for 60 min.

The values from Table 6.3 are illustrated in Figs. 6.9 and 6.10. In AC condition, the hardness after 60 min of ageing $\mathrm{HV}_{\mathrm{D,60}}$ (Fig. 6.9 a) was reduced linearly with increasing temperature for both degrees of cold deformation. For each temperature, the hardness of the samples deformed to 1.5 strain exceeded the hardness values of those deformed to 0.5 strain by around 10 HV0.1. The corresponding total hardness reduction $\mathrm{HV}_{\mathrm{D,red}}$ in Fig. 6.9 (b) showed a linear increase with increasing temperature and a rather constant offset to higher values for the more severely deformed AC samples. The hardness after 60 min of ageing at 400°C was slightly higher in PA compared to AC condition (Fig. 6.9 a). The total hardness reduction for PA samples was higher than for AC samples, as no precipitation hardening occurred during annealing of PA material (Fig. 6.9 b).

Fig. 6.10 (a) shows the hardness reduction adjusted for precipitation hardening $\mathrm{HV}_{\mathrm{D,soft}}$, i.e. pure softening due to restoration processes (Eq. 6.8). Here, the hardness reduction increased with increasing temperature for the AC samples, and again, the samples deformed to 1.5 strain showed more pronounced softening than those deformed to 0.5 strain. The progress of the AC curves in Figs. 6.9 (b) and 6.10 (a) was very similar to that in Fig. 5.25, where a steady increase of the recrystallized area fraction with temperature was observed, and higher values were measured for more severe deformation.

The similar dependencies of softening and recrystallized area fraction with annealing temperature support both measurements. The PA samples showed reduced softening due to restoration processes compared to the AC samples (Fig. 6.10 a), which is in good agreement to the in-situ CLSM and EBSD investigations (Fig. 5.30), where hardly any recrystallization was observed.

Fig. 6.10 (b) exemplarily summarizes the hardening and softening contributions occurring during annealing in the dilatometer and CLSM for an AC sample deformed to 1.5 strain, that was aged for 60 min. The hardness increment from $Al_3(Sc,Zr)$, HV_{prec}, decreased with increasing annealing temperature. Softening due to restoration processes occurring in the deformed microstructure, $HV_{D,soft}$, increased slightly with temperature. The total hardness reduction considering restoration and precipitation processes, $HV_{D,red}$, increased with increasing temperature. In other words, the total measured hardness reduction increased with increasing temperature but was partly compensated by the hardening increment from $Al_3(Sc,Zr)$ precipitates.

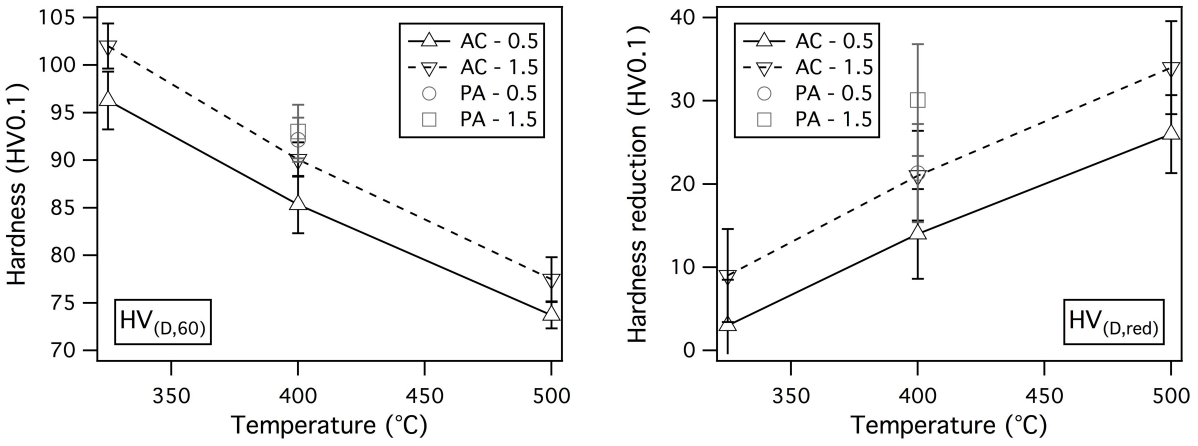

(a) Hardness ($HV_{D,60}$) after 60 min of ageing

(b) Total hardness reduction ($HV_{D,red}$)

Fig. 6.9: Hardness of cold deformed (0.5 and 1.5 strain) AC and PA samples after 60 min of ageing ($HV_{D,60}$) at various temperatures (a) and corresponding total hardness reduction ($HV_{D,red}$) with respect to the hardness of the cold deformed state (b) showing increasing softening with increasing annealing temperature.

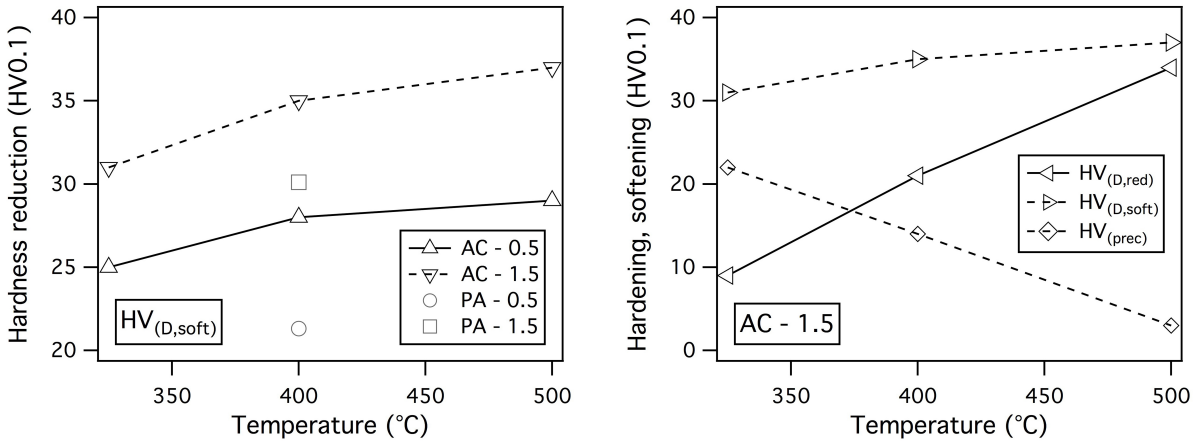

(a) Hardness reduction ($HV_{D,soft}$) due to RX/RV

(b) Summary of hardening and softening

Fig. 6.10: Hardness reduction ($HV_{D,soft}$) due to recrystallization and recovery (a); Summary of total hardness reduction ($HV_{D,red}$), softening due to restoration processes ($HV_{D,soft}$), and precipitation hardening (HV_{prec}) for an AC sample deformed to 1.5 strain (b). Error bars are in similar range as in Fig. 6.9 (b) but were removed to improve readability.

6.4.3 Softening mechanisms

The mechanisms to which softening occurred during annealing of deformed AC samples depended on both the initial strain and the ageing temperature, as shown in the CLSM and EBSD images (Fig. 5.23 and Fig. 5.24). The AC sample deformed to 0.5 strain that was heat treated at 325°C did not show any recrystallized grains. Thus, softening occurred purely due to recovery. For all other samples, a certain fraction of recrystallized grains was observed that increased with increasing temperature and initial plastic deformation. However, the maximum reached recrystallized area fraction was only 27% after ageing at 500°C for 60 min. In comparison, conventional Al-Mg3 alloys deformed to a true strain of about 0.8 showed full recrystallization after only 5 min of isothermal ageing at 360°C [108].

Jones *et al.* [82] proposed that recrystallization was fully inhibited for several hours up to 500°C in a high-purity binary Al-Sc alloy with 0.25 wt.% Sc in solution deformed to a true strain of 1.6. On the other hand, they showed that in an alloy with only 0.12 wt.% Sc in solution, recrystallization was impeded below 370°C, whereas at temperatures above $\sim$ 400°C full recrystallization was observed. They explained these observations with the relative magnitude of the driving force for precipitation compared to the driving force for recrystallization. At higher Sc-content (0.25 wt.%), precipitation was faster than re-

crystallization leading to Zener pinning even at 500°C. At lower Sc-content (0.12 wt.%), it was suggested that the driving force for recrystallization was higher than that of precipitation at temperatures higher 400°C and the other way round at temperatures below 370°C. The Al-Mg4-Sc0.4-Zr0.12 alloy in AC condition used in the present study had a solute Sc content of 0.13 wt.%. It would be expected that the alloy behaved like the Al-Sc0.12 alloy in the mentioned study [82] in case of similar deformation. This, however, was not the case and precipitation and recrystallization occurred simultaneously for the AC samples deformed to 1.5 strain even at 500°C. This behavior is explained with the reduced solid solubility of Sc in Al in the presence of Mg and Zr [42,90] leading to an increased driving force for Al_3(Sc,Zr) precipitation, thus faster kinetics. In consequence of the faster precipitation kinetics, the Zener pinning effect exerted by the Al_3(Sc,Zr) particles in the used Al-Mg-Sc-Zr alloy occurred earlier in time compared to the binary Al-Sc0.12 alloy shown in [82].

The EBSD images after annealing in a CLSM at 400°C for 60 min (Fig. 5.18 e, f) showed several recrystallized grains, but also few large recovered subgrains that were not fully surrounded by HAGBs, thus not termed recrystallized. These subgrains, highlighted with arrows in Fig. 5.18, were free of local misorientations and revealed orientations similar to their respective grain of origin. The mechanism behind such transformation is strain induced boundary migration (SIBM), whereas in case of the large recovered subgrains, the process was not finished due to pinning effects from Al_3(Sc,Zr) precipitates. Therefore, the morphology of the recovered subgrains was similar to that of growing subgrains in single-phase Al during early stages of SIBM [179]. When analyzing the recrystallized grains in Fig. 5.18 (f), it was recognized that also the recrystallized grains revealed orientations similar to their original grain (Fig. 5.18 c). Therefore, SIBM was considered as the main recrystallization mechanism, in agreement with studies on Al-Sc [82] and other dispersoid-containing Al-alloys [67].

For the samples deformed to 0.5 strain, recrystallization initiated at grain boundary triple points (Figs. 5.19 and 5.23). The samples deformed more severely to 1.5 strain revealed recrystallized grains located in distinct bands. Again, the grains nucleated at locations with highest dislocation densities. These nucleation sites were the grain boundaries of highly deformed, very flat grains indicated with a low CI (black) in Fig. 5.21 (b, c). As a consequence, the recrystallized grains were aligned along the original boundaries in bands. For all investigated sample conditions of AC and PA materials, large primary Al_3(Sc,Zr) phases were present. Particle-stimulated nucleation (PSN), however, was not observed in any case.

The pre-aged (PA) samples deformed to 0.5 and 1.5 strain showed less than 1% recrystallized area fraction after 60 min of ageing at 400°C, compared to 7% and 12% for the AC samples deformed to 0.5 and 1.5 strain, respectively. The fact that recrystallization was inhibited in the presence of Al_3(Sc,Zr) precipitates was in good agreement with previous studies, e.g. [88,108]. The softening effect during annealing observed in Fig. 5.29, therefore, occurred mainly due to recovery, in accordance with the reduced softening due to restoration $HV_{D,soft}$ for the PA samples compared to the AC samples (Table 6.3 and Fig. 6.10 a). In other words, the hardness decrement due to recovery was less pronounced than that of recrystallization. The degree to which recrystallization occurred was determined from EBSD measurements, whereas a quantification of recovery was not carried out.

6.4.4 Quantitative softening kinetics

In 6.4.2 it was explained that the precipitation kinetics in deformed and non-deformed positions of as-cast (AC) samples depended on temperature and time, but not on the degree of plastic deformation. This consideration allowed to isolate the hardness decrease caused by recrystallization or recovery from the hardening effect due to precipitation (Table 6.3). In this section, the temporal evolution of softening is derived by simply subtracting the hardness value in ND condition (HV_{ND}) from that of the deformed material (HV_D) at every time step i based on the data from Fig. 5.15:

$$\Delta HV_i = HV_{D,i} - HV_{ND,i}. \tag{6.9}$$

The value of ΔHV_i represents the remaining strain hardening increment at every time step (Fig. 6.8 a). The outcome of this evaluation for the AC samples aged at 325°C, 400°C, and 500°C is given in Fig. 6.11. The normalized Al_3(Sc,Zr) volume fraction is represented by the respective JMAK fits of Fig. 6.5 (a), while the hardness difference between deformed and non-deformed conditions (Eq. 6.9) is given by ΔHV. The initial values of ΔHV obviously represent the hardness increase due to cold deformation prior to ageing. It was found that the softening kinetics followed a power law relation:

$$\Delta HV = a + b \cdot t^{-r}, \tag{6.10}$$

where a and b are constants, t represents the time, and r is an exponent. The results of the individual fits from Eq. 6.10 are also incorporated in Fig. 6.11. At 325°C, ΔHV decreased steadily during ageing demonstrating a continuous reduction of the initial strain

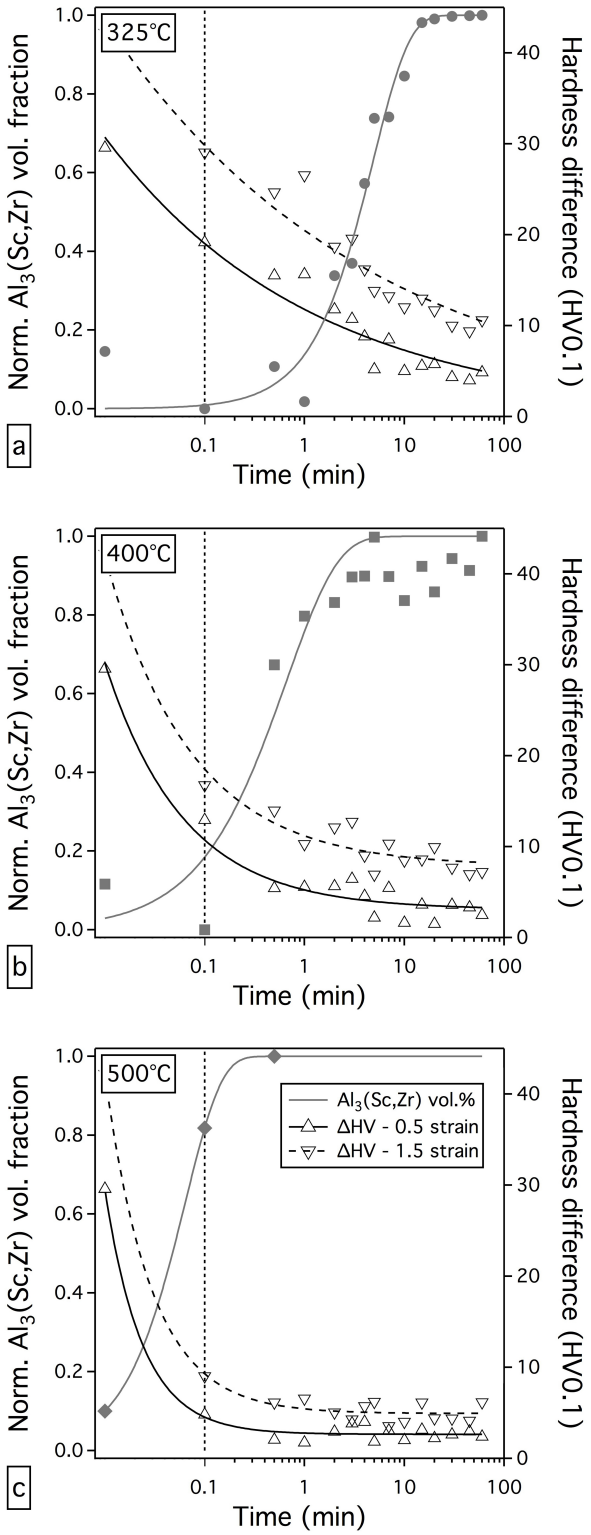

Fig. 6.11: Normalized $Al_3(Sc,Zr)$ precipitate volume fraction and evolution of the hardness difference between deformed and non-deformed AC material (ΔHV) as a function of ageing time at 325°C (a), 400°C (b), and 500°C (c).

hardening effect (Fig. 6.11 a). The fitted curves were similar in shape for different strains, whereas ΔHV was always larger for the sample deformed to 1.5 strain compared to that deformed to 0.5 strain. The general behavior during ageing at 400°C (Fig. 6.11 b) was similar to that observed at 325°C, however, the hardness loss during heat-up was more pronounced and the curves flattened significantly after around 5 min. The flattening of the ΔHV curves coincided with the rise of the Al_3(Sc,Zr) volume fraction and the end of grain boundary migrations observed by in-situ CLSM at 400°C in Fig. 5.23 and Fig. 5.24. At 500°C this behavior was even more pronounced and ΔHV reached a steady state after ageing for around 30 s. Again, the ΔHV curves reached their minima at the same time as the Al_3(Sc,Zr) volume fraction reached its maximum and the microstructure modifications shown by in-situ CLSM ceased (Fig. 5.23 and 5.24). The exponents from Eq. 6.10 were similar for strains of 0.5 and 1.5 for a given temperature and equaled $r = 0.2$ at 325°C, $r = 0.5$ at 400°C, and $r = 1$ at 500°C. For the investigated range of temperatures, times, and degrees of plastic deformation, ΔHV did not reach the minimum value of 0. In other words, the hardness increment introduced by cold deformation was never fully removed. This observation is in agreement with the microstructure characterizations from CLSM and EBSD revealing only partial recrystallization.

The same separation of softening and precipitation hardening was carried out for the PA samples aged at 400°C. Fig. 6.12 shows the normalized Al_3(Sc,Zr) precipitate volume fraction and the hardness difference ΔHV between deformed (PA) and ND (PA) material. The Al_3(Sc,Zr) precipitate volume fraction reached its equilibrium state already before deformation, and therefore equaled a normalized value of 1 over the entire heat treatment. Despite the different precipitate state, ΔHV showed the same power-law dependency for the PA samples as determined for the AC material, given in Eq. 6.10. The exponent r from Eq. 6.10 equaled roughly 0.6 and a steady-state was already reached after around 1 min for both strains of 0.5 and 1.5. The latter obervation is again in good agreement with the early stop of grain boundary migrations observed by in-situ CLSM in the presence of precipitates (Fig. 5.30).

In summary, softening could be described with a simple power-law relation from Eq. 6.10 independent of the acting mechanism. According to literature [39], similar functions were often used to describe growth rates that decreased significantly with time. This interpretation makes sense when considering that both recrystallization and recovery are increasingly impeded in the presence of precipitates that are growing in size, volume fraction, and number density with time. In such a situation, the Zener pinning effect becomes stronger while the growth rates of grains and subgrains decrease.

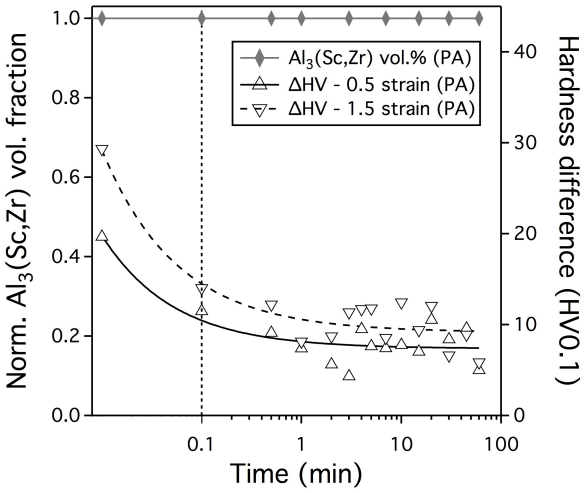

Fig. 6.12: Normalized Al_3(Sc,Zr) precipitate volume fraction and evolution of the hardness difference between deformed and non-deformed PA material (ΔHV) as a function of ageing time at 400°C.

6.4.5 Estimation of the driving pressure for recrystallization

The EBSD images of the deformed AC samples after annealing (Figs. 5.23 and 5.24) revealed local misorientations and deformation bands in the non-recrystallized grains, similar to a deformed microstructure (Fig. 5.14). A fully recovered substructure, on the other hand, was not observed. When comparing Figs. 5.23 and 5.24 with the EBSD image of the ND material in Fig. 5.14 (a), it can be expected that there exists still considerable driving force for recrystallization in the form of an increased dislocation density after annealing. It is well established [39] that the pressure for boundary movement in the situation of partial recrystallization can be described by:

$$P = P_D - P_C - P_Z, \tag{6.11}$$

where:

$$P_D = \alpha_2 \, \rho \, G \, b^2 \tag{6.12}$$

represents the driving pressure, as explained in detail in section 2.2.2.1. Based on these formulations, it is intended to derive a relative estimation of the driving pressure P_D from the measured ΔHV values. It is known that hardness and strength have a linear

dependency, e.g. [180,181]:

$$HV = k_3\,\sigma, \tag{6.13}$$

with a constant k_3, and that the strength can be represented as a sum of strength contributions from different barriers to dislocation movement (e.g. [16]):

$$\sigma = \sigma_0 + \sigma_{sol} + \sigma_{gs} + \sigma_{prec} + \sigma_{dis}. \tag{6.14}$$

Similar to Eq. 6.9, the difference between the strength of deformed (D) and non-deformed (ND) material is expressed by:

$$\Delta\sigma = \sigma_D - \sigma_{ND}. \tag{6.15}$$

It was shown that all strengthening contributions apart from that of dislocation density σ_{dis} were equivalent in deformed and non-deformed conditions. Therefore, the strength difference can be expressed as:

$$\Delta\sigma = \Delta\sigma_{dis} = \sigma_{dis,D} - \sigma_{dis,ND}. \tag{6.16}$$

Since [39]:

$$\sigma_{dis} = \alpha_1 G\,b\sqrt{\rho}, \tag{6.17}$$

it follows that:

$$\Delta\sigma_{dis} = k_4\,(\sqrt{\rho_D} - \sqrt{\rho_{ND}}), \tag{6.18}$$

where k_4 is a constant, and ρ_D and ρ_{ND} are the dislocation densities in deformed and ND material, respectively. The dislocation density in case of ND material is usually several orders of magnitude smaller than in deformed condition [58]. Consequently, ρ_{ND} was neglected in Eq. 6.18. From Eq. 6.13, 6.16, and 6.18 the following relationship was derived:

$$\rho_{def} \propto \Delta HV^2. \tag{6.19}$$

Using Eq. 6.12 and 6.19, the relative driving pressure between deformed and ND material finally relates to:

$$P_D \propto \Delta HV^2. \tag{6.20}$$

This notation of the relative driving pressure implies a value of $P_D = 0$ for the ND material.

6.4.6 Estimation of the Zener pinning pressure

The Zener pinning pressure for coherent, spherical particles [39] is described by:

$$P_Z = \frac{6 f_V \gamma}{2r}. \tag{6.21}$$

In section 6.3.3, it was concluded that the precipitate number density increased rapidly in the early stages of precipitation but remained constant during the larger part of the precipitate growth stage. To estimate the temporal evolution of the Zener pinning pressure, an approximation was used assuming that all precipitate nuclei were formed simultaneously at the beginning of the ageing treatment. The precipitate number density was assumed to remain constant during the growth stage. Under these considerations, the increasing radius r of the spherical precipitates lead to an increase in volume fraction with:

$$f_V = \frac{4\pi}{3} r^3. \tag{6.22}$$

Using Eq. 6.22 to substitute r from Eq. 6.21, lead to the estimation:

$$P_Z \propto f_V^{\frac{2}{3}}. \tag{6.23}$$

6.4.7 Comparison of driving pressure and Zener pressure

Both driving pressure and Zener pinning pressure were normalized for graphical interpretation. The driving pressure P_D (Eq. 6.20) for a temperature T and a strain ε was normalized with respect to the initial $\Delta\mathrm{HV}^2$ value of the 1.5 strain sample for the respective AC or PA condition:

$$P_{D,n\,(T,\varepsilon)} = \frac{\Delta HV^2_{T,\varepsilon}}{\Delta HV^2_{\varepsilon=1.5,\,t=0}}. \tag{6.24}$$

The Zener pressure (Eq. 6.23) was already calculated from the evolution of the normalized Al_3(Sc,Zr) precipitate volume fraction (Fig. 6.11), thus $P_Z = P_{Z,n}$, with the normalized Zener pinning pressure $P_{Z,n}$. It is noteworthy that the values of $P_{D,n}$ and $P_{Z,n}$ are not to be compared with respect to their magnitude, as they do not represent absolute values. Rather, they are only comparable regarding their temporal evolution.

Fig. 6.13 illustrates the evolution of the normalized driving pressure $P_{D,n}$ and the normalized Zener pinning pressure $P_{Z,n}$ for samples deformed to 0.5 and 1.5 strain. Fig. 6.13 (a to c) represents ageing of AC material at 325°C (a), 400°C (b), and 500°C (c). The evolution of $P_{D,n}$ and $P_{Z,n}$ for PA samples aged at 400°C is shown in Fig. 6.13 (d).

During ageing at 325°C (Fig. 6.13 a) the driving pressure $P_{D,n}$ was continuously reduced without reaching a steady minimum. The Zener pinning pressure $P_{Z,n}$ increased due to Al_3(Sc,Zr) precipitation reaching a maximum after around 20 min. In case of ageing at 400°C, $P_{D,n}$ was reduced over time but reached a rather flat region when $P_{Z,n}$ reached its maximum value after around 5 min, as shown in Fig. 6.13 (b). This observation was in agreement with the ceasing recrystallization process detected from the in-situ CLSM and EBSD investigations. At 500°C, the minimum of $P_{D,n}$ and the maximum of $P_{Z,n}$ were reached after around 30 s, as it was observed from the microstructure characterizations. In contrast to the AC samples annealed at lower temperatures, a reduction in hardness due to precipitate coarsening was observed at 500°C (Fig. 5.15 c). Consequently, the Zener pinning pressure $P_{Z,n}$ was reduced after reaching a maximum, indicated with an arrow in Fig. 6.13 (c). However, despite the reduced Zener pinning pressure, the driving pressure for recrystallization was not large enough to proceed recrystallization in the considered annealing time. It is expected that recrystallization would continue, once the precipitate number density was low enough so that, in absolute values, $P_D > P_Z$. The relative driving pressure for recrystallization after 60 min of ageing decreased with increasing temperature for the AC samples (Fig. 6.13 a to c). These observations are in agreement with the measured recrystallized area fraction (Fig. 5.25) and hardness reduction (Figs. 6.9 and 6.10).

Fig. 6.13 (d) shows the normalized driving pressure $P_{D,n}$ and Zener pinning pressure $P_{Z,n}$ for the PA samples annealed at 400°C. The maximum Zener pinning pressure was exhibited at the beginning of the annealing procedure and was constant until coarsening initiated after around 2 min, as shown by the hardness reduction of non-deformed PA material in Fig. 5.29. The high Zener pinning pressure at the beginning of the annealing procedure resulted in an almost full inhibition of recrystallization, as shown in Fig. 5.30. The normalized driving pressure $P_{D,n}$ reached a minimum value already after 1 min of

ageing at 400°C, in accordance with the CLSM and EBSD investigations. Despite the reduction of $P_{Z,n}$ after 2 min due to coarsening, apparently, the absolute Zener pinning pressure exceeded the absolute driving pressure for recrystallization until the end of the experiment. A quantitative comparison between the $P_{D,n}$ values in AC and PA condition in Fig. 6.13 is not possible due to the difference of the initial ΔHV^2 values.

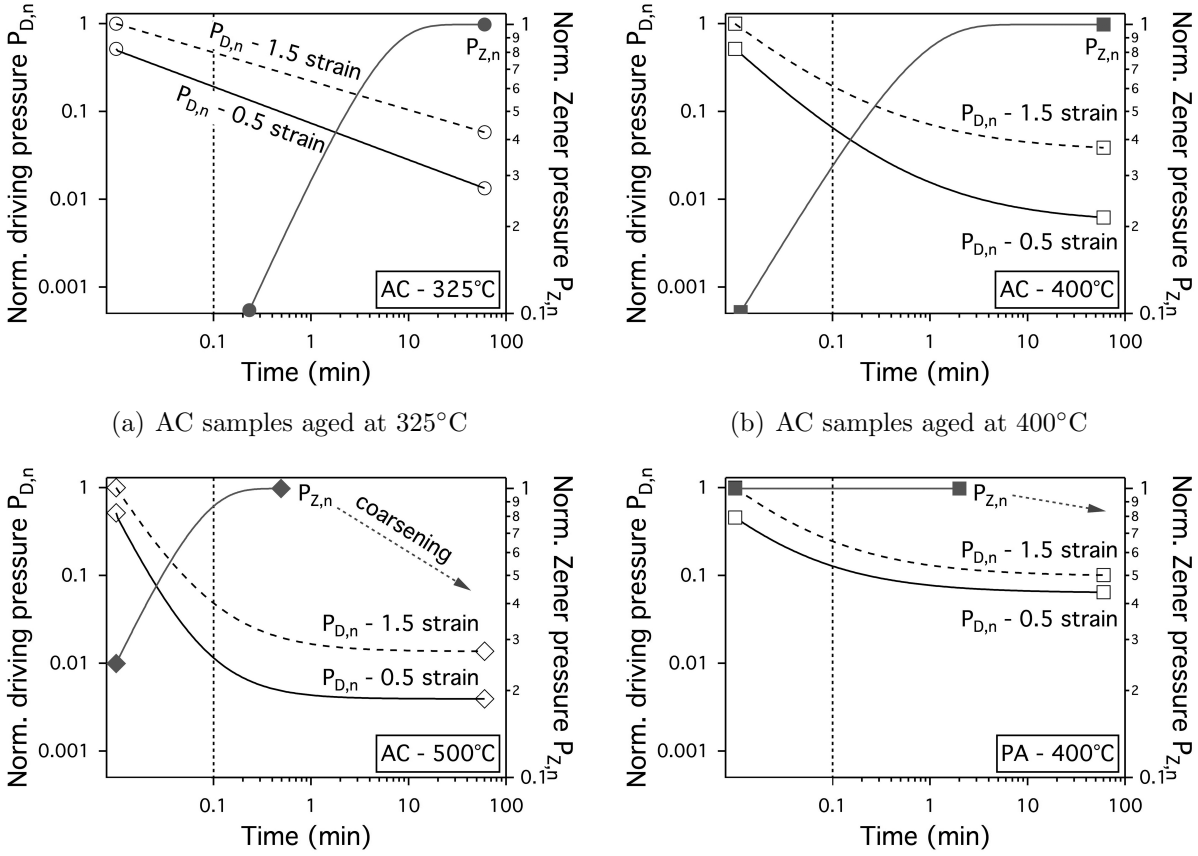

(a) AC samples aged at 325°C

(b) AC samples aged at 400°C

(c) AC samples aged at 500°C

(d) PA samples aged at 400°C

Fig. 6.13: Estimation of the evolution of normalized driving pressure $P_{D,n}$ and Zener pinning pressure $P_{Z,n}$ during ageing of AC material at 325°C (a), 400°C (b), and 500°C (c), as well as PA material at 400°C (d). Normalization of $P_{D,n}$ with respect to initial ΔHV^2 of the 1.5 strain sample for the respective condition. $P_{Z,n}$ calculated from normalized Al_3(Sc,Zr) volume fraction. Vertical dashed lines represent end of 1 min heating stage.

6.5 Recommendations for alloy and stringer production

The production process of a welded Al-Mg-Sc-Zr stringer in the context of the current research project "OscAR" is intended to consist of the following steps:

1. Casting using a rapid solidification method.
2. Thermo-mechanical processing to produce sheet metal.
3. Roll forming of the sheet into a stringer.
4. Welding of the stringer on a sheet panel.
5. Creep forming of the welded component.

Based on the fundamental outcome presented in this work and published in [182–185], some recommendations can be derived in order to appropriately design an industrial production process. In addition to the precipitation and rerystallization kinetics, the deformation behavior [186–188] and the weldability [189] of the used Al-Mg-Sc-Zr alloys were investigated.

6.5.1 Casting

After belt casting, in AC materials condition, a fairly large amount of primary and eutectic Al_3(Sc,Zr) phases was present leading to a reduced supersaturation in Sc. However, it was demonstrated in this study, that a high degree of Sc-supersaturation is the key factor in order to achieve high strength. Therefore, it is recommended to optimize the used belt-caster towards higher solidification and cooling rates. If this is not possible, the use of an alternative casting technique with high solidification and cooling rates such as twin roll casting (TRC) [190–192] is suggested.

6.5.2 Thermo-mechanical processing

The casted material needs to be processed into sheet metal by rolling. This rolling operation can be done at room temperature or at elevated temperature. Both cold and hot deformation up to 400°C was investigated using plane-strain compression testing to simulate industrial rolling processes [186,188]. Defect-free samples could be produced with both cold and hot deformation using appropriate processing parameters. The flow curves for the samples deformed with a strain rate of $10\,s^{-1}$ are shown in Fig. 6.14 for the entire investigated temperature range. The flow stress was reduced with increasing

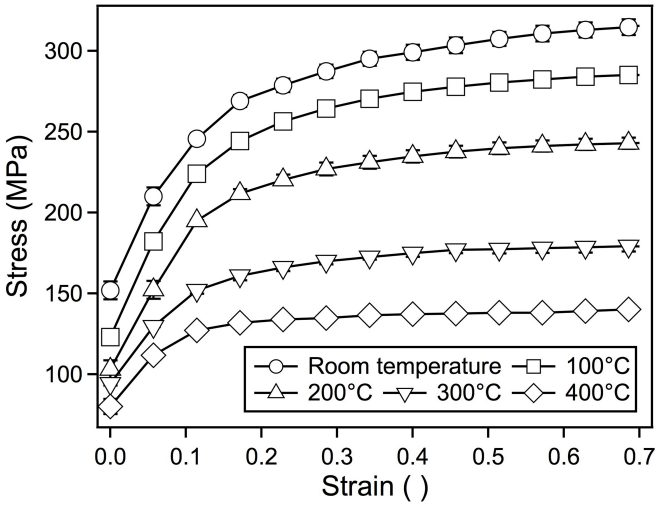

Fig. 6.14: Flow curves of AC samples deformed with a strain rate of $10\,s^{-1}$ using plane-strain compression tests in a temperature range from room temperature to 400°C.

temperature as a result of dynamic recovery effects. Al_3(Sc,Zr) precipitates formed during deformation at temperatures higher than 350°C only if the strain rate was as low as $10^{-2}\,s^{-1}$. However, the strengthening precipitates could not compensate for the dynamic softening effect, as shown by hardness measurements at room temperature [186]. Higher hardness values could be achieved if cold deformation was followed by an ageing treatment. In order to achieve maximum strength, therefore, cold deformation is recommended. On the other hand, cold deformed sheet metal without any additional heat treatment showed a very brittle behavior with fracture elongations of only $2-3\%$. To form a stringer from sheet metal by roll forming, the ductility of the Al-Mg-Sc-Zr sheet needs to be improved to around 10%. One way to increase the ductility in the entire sheet is annealing in a temperature regime, where recrystallization or recovery occurs.

In the present study, the behavior of cold deformed Al-Mg-Sc-Zr during annealing was investigated in detail. The recrystallization of cold deformed AC material was significantly inhibited at 325°C even if the Al_3(Sc,Zr) precipitates were not present prior to the heat treatment. The hardness of the cold deformed material was maintained to a large extent since softening was partly compensated by the precipitation of strengthening Al_3(Sc,Zr) particles. According to the findings in 5.3 and 6.4, annealing of cold deformed material at temperatures higher than 325°C should be avoided if the strength should be maintained at a high level. In additional activities in the project, it was found that the desired fracture elongation of 10% in a cold rolled sheet was only achieved after several hours of ageing at temperatures as high as 400°C leading to an unacceptable loss

in strength. These results on a macroscopic level are in agreement with results of the present study obtained from laboratory tests, where it was found that recrystallization and softening occurred predominantly at temperatures higher than 325°C.

6.5.3 Forming of a stringer

Roll forming at room temperature was successfully applied in the project if the fracture elongation of the rolled sheet was higher than 10%. The required heat treatment to achieve enough ductility for cold roll forming, however, was accompanied by an unacceptable loss in strength, as mentioned above. Therefore, it was aimed to integrate an induction heating system into the roll forming process to facilitate local heating in the severely deformed regions of the cold rolled sheet to locally increase the formability. The fracture elongation of the non-heat treated cold rolled Al-Mg-Sc-Zr sheet was assessed as a function of temperature in a preliminary hot tensile testing study. Fig. 6.15 (a) shows the outcome of this investigation. The test cycle consisted of heating to the respective testing temperature with $5\,\mathrm{Ks}^{-1}$, followed by a 10 s holding time prior to testing. It was found that a temperature of 200°C was high enough to achieve the desired fracture elongation. Temperatures higher than 325°C, on the other hand, should be avoided to limit potential softening effects and to prevent precipitation of $Al_3(Sc,Zr)$ phases. A preliminary hot roll forming test was successfully applied based on these recommendations. Fig. 6.15 (b) shows the first prototype of a hot roll formed stringer made of Al-Mg-Sc-Zr.

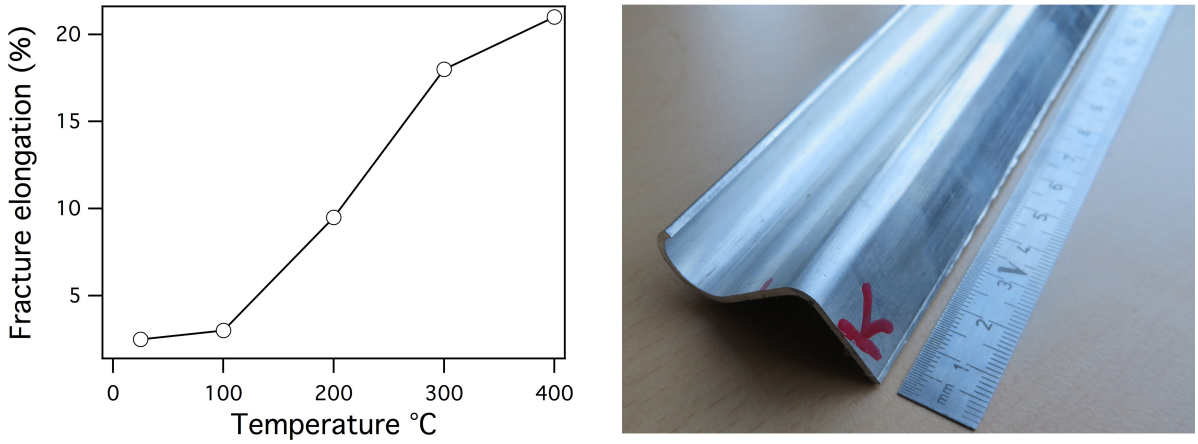

(a) Fracture elongation vs. temperature

(b) Prototype of a stringer

Fig. 6.15: Fracture elongation of a cold rolled Al-Mg-Sc-Zr sheet as a function of temperature obtained from hot tensile tests (a). Prototype of a hot roll formed stringer (b) made of Al-Mg-Sc-Zr (Courtesy of H. Kerstan, Welser Profile Austria GmbH).

6.5.4 Welding

Laser and friction stir welding (FSW) are considered as relevant welding processes to join stringers and skin panels. In general, Al-Mg-Sc(-Zr) alloys show good weldability similar to conventional Al-Mg alloys using both fusion [193,194] and friction stir welding [195,196]. The mentioned studies [193–196] were carried out using materials where Al_3Sc precipitates were present prior to welding and the Al matrix was free of solute Sc.

In the present work, it was intended to characterize a rapidly solidifed alloy with a certain amount of Sc in solid solution prior to welding. Laser welding was not investigated in the project but it can be assumed that the degree of Sc-supersaturation will increase in the weld region, similar to what was observed in the EBRS material. FSW of as-cast (AC) Al-Mg-Sc-Zr material was studied in detail [189] to analyze the influence of the welding parameters on the Al_3(Sc,Zr) precipitation using an ISTIR FSW machine (MTS). Blind welds on 8 mm thick casted material were accomplished using a threaded pin tool (Stirtec) with a shoulder diameter of 15 mm and a pin length of 5.5 mm. The basic processing parameters were a tilt angle of 0° and a tool rotation speed of 1200 min^{-1}. Two different parameter sets were studied aiming for a variation in heat input. The high heat input weld was carried out using a welding speed of 100 $\mathrm{mm\,min}^{-1}$ and a vertical down force of 6.5 kN, while the low heat input weld was done at 1000 $\mathrm{mm\,min}^{-1}$ and 32.5 kN vertical down force. The hardness across the welds was studied in as-welded and in post-weld heat treated (PWHT) conditions (325°C for 60 min).

Fig. 6.16 shows hardness patterns across the friction stir welds of low (a) and high heat input (b). The acronym AS refers to the advancing side of the weld, and RS refers to the retreating side [197]. The respective dashed lines represent the as-welded conditions, while the full lines correspond to the PWHT conditions. In case of low heat input (Fig. 6.16 a), the hardness in as-welded condition was at a similar level in the unaffected base material and the different zones inside the weld. After PWHT, the hardness increased in average by 22 HV0.1 due to precipitation of Al_3(Sc,Zr) phases leading to a rather constant hardness plateau across the entire weld. In case of high heat input (Fig. 6.16 b), the hardness in as-welded condition increased with decreasing distance to the weld center with the highest hardening increment of around 12 HV0.1 inside the stir-zone. However, after PWHT no further hardening was observed inside the weld and the hardness of the unaffected base material was not reached.

Temperature measurements were carried out during welding at various distances from the weld center using K-type thermocouples. The most relevant measuring position was

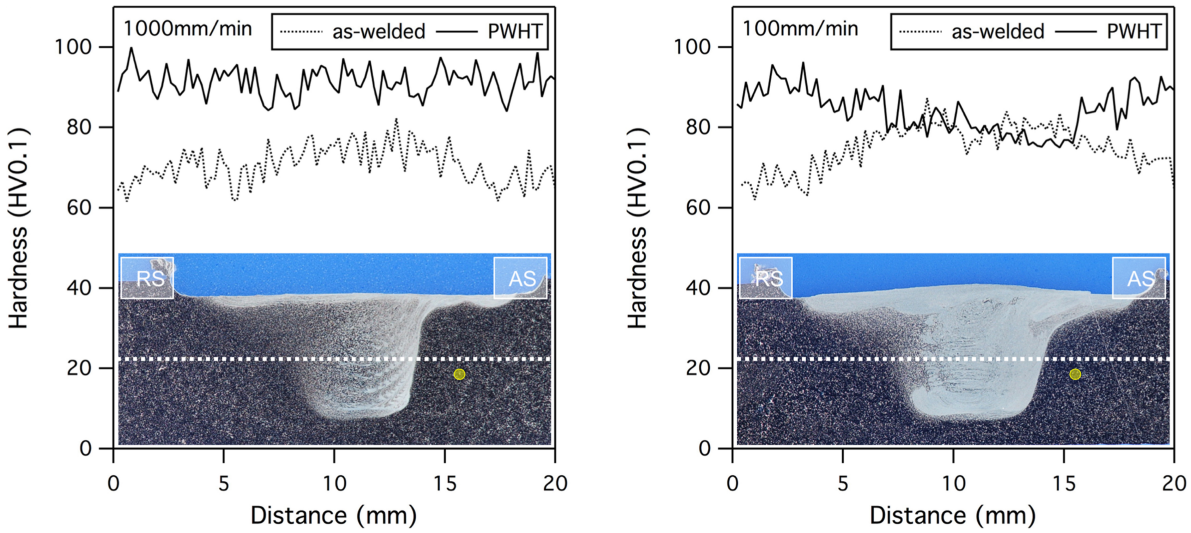

(a) Low heat input weld

(b) High heat input weld

Fig. 6.16: Macrosections and hardness patterns across low (a) and high (b) heat input friction stir welds showing the influence of the welding parameters and post-weld heat treatment on the $Al_3(Sc,Zr)$ precipitation. Yellow circles indicate positions of temperature measurements 5 mm from the weld center [189].

located 5 mm away from the weld center on the advancing side, as indicated by the yellow circles in Fig. 6.16. The peak temperature at this point equaled 460°C for low heat input and 475°C for high heat input, thus the temperature difference at this point was surprisingly small. However, it was found that the exposure to high temperatures was significantly longer in case of high heat input welds. As the temperatures inside the welds were certainly higher than the measured temperatures beside the weld, it was concluded, that strengthening $Al_3(Sc,Zr)$ precipitates were formed already during the welding process at temperatures higher than 475°C in the high heat input weld. In consequence, the hardness in as-welded condition increased slightly in the weld zone of the high heat input weld. In such a case, the precipitates are expected to be coarse and have a low number density, as shown in 5.2 and 6.3. During PWHT at 325°C, therefore, no additional precipitation hardening could be achieved. In contrast, the maximum hardness was lower inside the weld compared to the unaffected base material. For low heat input welds, the exposure to elevated temperatures was short enough to prevent the formation of $Al_3(Sc,Zr)$ precipitates during welding. In consequence, the hardness was constant across the entire weld and base material. In summary, friction stir welding with low heat input is recommended for industrial application, because the strength of the weld can be controlled by a PWHT and can reach the same level as the base material.

6.5.5 Forming of a welded component

The final step in the production routine is a creep forming process of the welded component, as explained in [198]. The primary goal of this process is to form a component of specific shape. In addition, the process can be used to achieve peak-age condition for the given Al-Mg-Sc-Zr alloy having Sc in solid solution prior to creep forming using appropriate processing parameters. According to the findings in this study, the forming temperature should not exceed 325°C, since the maximum achievable hardness decreased. Lower annealing temperatures might result in higher final hardness but would require ageing times longer than 180 min. The heating rate should be lower than $\sim 5°Cs^{-1}$ to promote precipitate nucleation and achieve a high precipitate number density.

Fig. 6.17 summarizes the optimized processing routine. After belt casting using an optimized process with a solidification rate high enough to dissolve large amounts of Sc, the material is cold rolled into sheet metal condition. Hot roll forming to stringer profiles is carried out by locally increasing the temperature to around 200°C to locally increase the ductility while preventing the formation of Al_3(Sc,Zr) due to short exposure time. The stringers are welded to the skin panels by FSW using low heat input to keep Sc in solid solution. In the final creep forming process, the alloy is peak aged at maximum 325°C to promote the formation of a fine distribution of Al_3(Sc,Zr) precipitates.

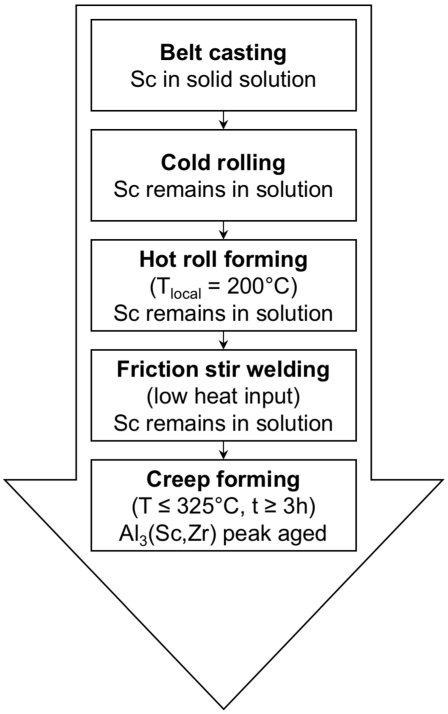

Fig. 6.17: Summary of the optimized processing routine with respect to the presence of Sc.

7 Summary and conclusions

Al-Mg alloys modified with Sc and Zr possess superior mechanical properties than conventional Al-Mg alloys while maintaining the positive materials characteristics such as weldability and corrosion behavior. This unique combination of materials properties makes this type of alloys a promising candidate for applications in aircraft fuselage components, in particular for stringers. However, so far there exist no Al-Mg-Sc-Zr alloys that reach the required strength level of the currently used Al-Cu-Mg alloys. One of the main drawbacks of Al-Mg-Sc-Zr alloys is the need for rapid solidification, since a solution heat treatment in practice is not possible. Here, a new material developed and produced using an industrial belt-casting process was characterized to correlate the microstructure evolution and the corresponding mechanical properties to the thermo-mechanical processing routine.

The novel industry-scale belt-casted Al-Mg4-Sc0.4-Zr0.12 alloy was analyzed for the first time. It was found that in as-cast condition, only 0.13 wt.% of a potential of 0.4 wt.% Sc was in solution. The remaining 0.27 wt.% Sc was bound in primary and eutectic Al_3(Sc,Zr) phases and did not contribute to precipitation strengthening. Using an electron-beam re-solidification (EBRS) process, it was possible to dissolve almost the entire content of Sc and, thus, increase the degree of Sc-supersaturation.

Precipitation kinetics

The precipitation kinetics was quantitatively determined as a function of ageing time, temperature, and degree of Sc-supersaturation. The age hardening behavior of furnace annealed samples was correlated to in-situ synchrotron XRD measurements and HR-STEM and EFTEM analyses. The conclusions can be summarized as follows:

1. Within 180 min of isothermal ageing, peak-age condition was achieved at 325°C and 400°C, not at lower temperatures. For each temperature, the samples with a higher degree of Sc-supersaturation showed more pronounced age hardening response. The maximum hardness increase of around 70% was achieved for the material with 0.37 wt.% Sc in solution (EBRS) after ageing at 325°C for 180 min.

2. The hardness increase was solely due to the precipitation of coherent, nano-sized Al_3(Sc,Zr) precipitates distributed homogeneously in the matrix.

3. The number of Al_3(Sc,Zr) nucleation events decreased and the precipitate growth rate increased with increasing temperature. For a given temperature, the precipitation kinetics was slightly faster for a higher degree of Sc-supersaturation.

4. In peak-age condition, the precipitate volume fraction was close to the theoretical limits of the binary Al-Sc system. The influence of Mg and Zr on the precipitation kinetics could be neglected.

5. The mean precipitate radius increased with increasing temperature but was rather unaffected by the varying amount of Sc in solution prior to ageing. The Al_3(Sc,Zr) number density, in contrast, showed a linear dependency with the degree of Sc-supersaturation. Furthermore, the number density decreased with increasing ageing temperature.

6. For the studied material, the JMAK analysis could be carried out directly on the hardness values to determine the precipitation kinetics of Al_3(Sc,Zr). The precipitation process occurred by a fast increase of the precipitate number density in the early stages, followed by a rapid decrease of the nucleation rate with decreasing supersaturation and the growth of existing precipitates until an equilibrium volume fraction was reached.

In-situ CLSM approach

A novel process based on confocal laser scanning microscopy (CLSM) was introduced to study the recrystallization kinetics of age hardening alloys in-situ. This precedure was shown for the first time using the newly developed Al-Mg4-Sc0.4-Zr0.12 alloy. The following conclusions can be drawn:

1. CLSM is a powerful method to observe the migration of existing and the formation of new grain boundaries during recrystallization. The in-situ technique allows pursuing the temporal sequence and local initiation of recrystallization in a single experiment.

2. The observed grain structure evolution in CLSM was in good agreement with EBSD measurements both before and after annealing. The accuracy of the CLSM observations decreased with increasing deformation and decreasing grain size due to limited resolution.

3. The in-situ observations at the surface correlated to the microstructure modifications inside the bulk material both in terms of recrystallized area fraction and grain size, as well as to the measured hardness evolution.

4. Pros of the proposed CLSM approach:
   - Straightforward approach, easy to apply, simple data interpretation
   - Direct observation on a surface area of hundreds by hundreds of microns
   - Start and end of recrystallization process determined in a single experiment
   - Local evolution of recrystallization can be directly observed

5. Cons of the proposed CLSM approach:
   - Limited spatial resolution in case of large deformation and small grains
   - Recrystallization kinetics slow enough to observe boundary migrations

Recrystallization kinetics

The kinetics of softening was studied using a combined approach of heat treatments in a dilatometer, hardness testing, in-situ CLSM observations, and electron microscopy techniques. The softening kinetics was isolated from that of precipitation hardening by calculating the difference in the hardness evolution between deformed and non-deformed material assuming deformation-independent Al_3(Sc,Zr) precipitation. Hereafter a summary of the most relevant conclusions:

1. In as-cast (AC) material condition, the Al_3(Sc,Zr) precipitation occurred by fast growth of nuclei that formed after short ageing times. In this case, the Zener pinning effect increased with increasing precipitate volume fraction. In pre-aged (PA) material condition, an Al_3(Sc,Zr) precipitate volume fraction close to equilibrium was present prior to annealing, thus the maximum Zener pinning pressure was exerted from the beginning of the heat treatment.

2. Recovery was the dominant softening mechanism for AC material deformed to a strain of 0.5 prior to ageing at 325°C. For larger strain and/or higher annealing temperature, recrystallization was the dominant mechanism. In pre-aged (PA) condition, recrystallization was almost fully inhibited and recovery was the dominant mechanism even at 400°C.

3. For the as-cast (AC) material, recrystallization ceased after around 5 min at 400°C and after 0.5 min at 500°C due to significant Zener pinning. The ceasing grain

boundary migrations were observed in-situ using CLSM. The effect of Zener pinning of Al_3(Sc,Zr) precipitates was confirmed by TEM investigations where particle-boundary interactions were observed.

4. Full recrystallization was not observed in the investigated range of plastic strains and annealing temperatures. The maximum recrystallized area fraction for the AC sample deformed to 1.5 strain aged at 500°C equaled 27%.

5. The total hardness reduction of deformed samples due to annealing increased with increasing ageing temperature, whereas the hardness reduction associated with recovery or recrystallization was partly compensated by the precipitation of Al_3(Sc,Zr) phases in AC material.

6. The isolated softening kinetics followed a simple power law relation, independent of the precipitate state prior to ageing and independent of whether recovery or recrystallization was the dominant softening mechanism. The power law kinetics corresponds to a decreasing growth rate of recrystallized grains.

8 Outlook

The potentials and drawbacks of belt-casted Al-Mg-Sc-Zr alloys were fundamentally analyzed in this thesis. One of the most relevant outcomes, the quantitative description of the Al_3(Sc,Zr) precipitation as a function of the Sc-content, will be used as a reference to implement the Al-Mg-Sc-Zr alloy system in the software application MatCalc. This software is capable of calculating phase equilibria and precipitation kinetics in multi-component systems, provided that the used thermodynamic and diffusion databases are optimized using reliable experimental data. In consequence, ressource-consuming experimental studies can be reduced to a minimum in the future.

The findings of this study need to be implemented in the relevant industrial processes to take a practical step forward towards producing an Al-Mg-Sc-Zr stringer. Preliminary studies on the behavior of the alloy in some of the production steps showed rather positive results. The production of parts and components from Al-Mg-Sc-Zr sheet metal with high strength is possible if higher cooling rates can be achieved in the casting process to avoid any formation of Al_3(Sc,Zr) phases. If this is the case, a production route consisting of cold rolling, roll forming at locally increased temperatures, friction stir welding, and creep forming may be promising. In addition, Al-Mg-Sc-Zr alloys are highly interesting for additive manufacturing. As shown in the present study, the most beneficial mechanical properties can be achieved only by rapid solidification, which is the most relevant characteristic of many additive manufacturing processes. The suitability of Al-Sc powders for the selective laser melting (SLM) process was already demonstrated, e.g. [137,138]. In these studies, exceptional mechanical properties were achieved in the additive manufactured materials. It would be interesting to study the suitability of wire based additive manufacturing processes using arc or electron beam as a power source.

Based on the promising properties of the alloy investigated in this study and its future application potential, this thesis is finished with a statement of Gunnar Raade, a senior curator at the Geological Museum of the University of Oslo, Norway [10]:

> "I am convinced that scandiums's heyday is ahead of us."

References

[1] Airbus, *Global Market Forecast - Flying By Numbers*. Blagnac Cedex, France: AIRBUS, 2015.

[2] H. Helms and U. Lambrecht, "The potential contribution of lightweighting to reduce transport energy consumption," *The International Journal of Life Cycle Assessment*, vol. 12, pp. 58–64, 2007.

[3] L. Frommberg, "A30X: Ein ganz neuer Airbus," *aerotelegraph*, 2013.

[4] M. C.-Y. Niu, *Airframe structural design: practical design information and data on aircraft structures*. Hong Kong: Conmilit Press Ltd., 2000.

[5] S. Gudmundsson, *General aviation aircraft design: Applied methods and procedures*. Oxford, UK: Butterworth-Heinemann, 1 ed., 2014.

[6] A. Stephan, "Structural component and method for stiffening an external skin," 2011. Patent EP2195234 B1.

[7] J. C. Williams and E. A. Starke, "Progress in structural materials for aerospace systems," *Acta Materialia*, vol. 51, no. 19, pp. 5775–5799, 2003.

[8] A. Heinz, A. Haszler, C. Keidel, S. Moldenhauer, R. Benedictus, and W. Miller, "Recent development in aluminium alloys for aerospace applications," *Materials Science and Engineering A*, vol. 280, no. 1, pp. 102–107, 2000.

[9] J. Røyset and N. Ryum, "Scandium in aluminium alloys," *International Materials Reviews*, vol. 50, no. 1, pp. 19–44, 2005.

[10] G. Raade, "Scandium," *Chemical and Engineering News*, vol. 81, no. 36, 2003.

[11] J. Kaiser, "Fast and Slow Trains out of the Bear Market Trough," in *Canadian Investor Conference*, (Vancouver, CA), 2015.

[12] H. Kuhn and D. Medlin, eds., *ASM Handbook Volume 8 - Mechanical Testing and Evaluation*. Ohio, USA: ASM International, 2007.

[13] W. D. Callister and D. G. Rethwisch, *Materials Science and Engineering: An Introduction*. Hoboken, USA: John Wiley and Sons, Inc., 8. ed., 2010.

[14] J. F. Shackelford, *Introduction to Materials Science for Engineers*. New York, USA: Macmillan Publishing Company, 3. ed., 1992.

[15] J. R. Davis, ed., *Aluminum and Aluminum Alloys*. Ohio, USA: ASM International, 1993.

[16] M. Tiryakioglu and J. T. Staley, "Physical Metallurgy and the Effect of Alloying Additions in Aluminum Alloys," in *Handbook of Aluminum Volume 1 - Physical Metallurgy and Processes* (G. E. Totten and D. S. MacKenzie, eds.), ch. 3, pp. 81–209, New York, USA: Marcel Dekker, Inc., 2003.

[17] F. Fazeli, W. Poole, and C. Sinclair, "Modeling the effect of Al_3Sc precipitates on the yield stress and work hardening of an Al-Mg-Sc alloy," *Acta Materialia*, vol. 56, no. 9, pp. 1909–1918, 2008.

[18] E. A. Marquis, D. N. Seidman, and D. C. Dunand, "Effect of Mg addition on the creep and yield behavior of an Al-Sc alloy," *Acta Materialia*, vol. 51, no. 16, pp. 4751–4760, 2003.

[19] B.-H. Lee, S.-H. Kim, J.-H. Park, H.-W. Kim, and J.-C. Lee, "Role of Mg in simultaneously improving the strength and ductility of Al-Mg alloys," *Materials Science and Engineering: A*, vol. 657, pp. 115–122, 2016.

[20] I. Holzer and E. Kozeschnik, "Computer simulation of the yield strength evolution in Cu-precipitation strengthened ferritic steel," *Materials Science and Engineering A*, vol. 527, no. 15, pp. 3546–3551, 2010.

[21] A. Ardell, "Precipitation hardening," *Metallurgical Transactions A*, vol. 16A, pp. 2131–2165, 1985.

[22] I. Toda-Caraballo and P. E. J. Rivera-Díaz-Del-Castillo, "Modelling solid solution hardening in high entropy alloys," *Acta Materialia*, vol. 85, pp. 14–23, 2015.

[23] A. Yilmaz, "The Portevin-Le Chatelier effect: a review of experimental findings," *Science and Technology of Advanced Materials*, vol. 12, pp. 1–16, 2011.

[24] M. Jobba, R. K. Mishra, and M. Niewczas, "Flow stress and work-hardening behaviour of Al-Mg binary alloys," *International Journal of Plasticity*, vol. 65, pp. 43–60, 2015.

[25] H. Ait-Amokhtar, C. Fressengeas, and K. Bouabdallah, "On the effects of the Mg content on the critical strain for the jerky flow of Al-Mg alloys," *Materials Science and Engineering A*, vol. 631, pp. 209–213, 2015.

[26] S. Zhao, C. Meng, F. Mao, W. Hu, and G. Gottstein, "Influence of severe plastic deformation on dynamic strain aging of ultrafine grained Al-Mg alloys," *Acta Materialia*, vol. 76, pp. 54–67, 2014.

[27] R. C. Picu and D. Zhang, "Atomistic study of pipe diffusion in Al-Mg alloys," *Acta Materialia*, vol. 52, no. 1, pp. 161–171, 2004.

[28] H. Halim, D. S. Wilkinson, and M. Niewczas, "The Portevin-Le Chatelier (PLC) effect and shear band formation in an AA5754 alloy," *Acta Materialia*, vol. 55, no. 12, pp. 4151–4160, 2007.

[29] D. Zhemchuzhnikova, A. Mogucheva, and R. Kaibyshev, "Mechanical properties and fracture behavior of an Al-Mg-Sc-Zr alloy at ambient and subzero temperatures," *Materials Science and Engineering A*, vol. 565, pp. 132–141, 2012.

[30] E. Ghali, *Corrosion Resistance of Aluminum and Magnesium Alloys*. Hoboken, NJ: John Wiley and Sons, Inc., 2010.

[31] G. B. Burger, A. K. Gupta, P. W. Jeffrey, and D. J. Lloyd, "Microstructural control of aluminum sheet used in automotive applications," *Materials Characterization*, vol. 35, no. 1, pp. 23–39, 1995.

[32] Y. Wang and H. Choo, "Influence of texture on Hall-Petch relationships in an Mg alloy," *Acta Materialia*, vol. 81, pp. 83–97, 2014.

[33] M. Y. Seok, I. C. Choi, J. Moon, S. Kim, U. Ramamurty, and J. I. Jang, "Estimation of the Hall-Petch strengthening coefficient of steels through nanoindentation," *Scripta Materialia*, vol. 87, pp. 49–52, 2014.

[34] T. D. Shen, R. B. Schwarz, S. Feng, J. G. Swadener, J. Y. Huang, M. Tang, J. Zhang, S. C. Vogel, and Y. Zhao, "Effect of solute segregation on the strength of nanocrystalline alloys: Inverse Hall-Petch relation," *Acta Materialia*, vol. 55, no. 15, pp. 5007–5013, 2007.

[35] E. Kozeschnik, *Modeling Solid-State Precipitation*. Momentum Press, 2013.

[36] R. E. Smallman and R. J. Bishop, *Modern Physical Metallurgy and Materials Engineering*. Oxford, UK: Butterworth-Heinemann, 6 ed., 1999.

[37] D. R. Askeland, *The Science and Engineering of Materials*. London, UK: Chapman and Hall, 3. ed., 1996.

[38] D. Seidman, E. Marquis, and D. Dunand, "Precipitation strengthening at ambient and elevated temperatures of heat-treatable Al (Sc) alloys," *Acta Materialia*, vol. 50, no. 16, pp. 4021–4035, 2002.

[39] F. Humphreys and M. Hatherly, *Recrystallization and related annealing phenomena*. Pergamon, 2. ed., 2004.

[40] I. J. Polmear, *Light Alloys*. Burlington, USA: Elsevier, 4. ed., 2006.

[41] J. Robson, M. Jones, and P. Prangnell, "Extension of the N-model to predict competing homogeneous and heterogeneous precipitation in Al-Sc alloys," *Acta Materialia*, vol. 51, no. 5, pp. 1453–1468, 2003.

[42] J. Røyset and N. Ryum, "Kinetics and mechanisms of precipitation in an Al-0.2 Sc alloy," *Materials Science and Engineering A*, vol. 396, no. 1-2, pp. 409–422, 2005.

[43] K. A. Jackson, *Kinetic Processes*. Weinheim, Germany: Wiley-VCH Verlag GmbH & Co. KGaA, 2004.

[44] A. Deschamps, L. Lae, and P. Guyot, "In situ small-angle scattering study of the precipitation kinetics in an Al-Zr-Sc alloy," *Acta Materialia*, vol. 55, no. 8, pp. 2775–2783, 2007.

[45] J. W. Christian, *The Theory of Transformations in Metals and Alloys*. Elsevier Science Ltd, 3 ed., 2002.

[46] L. Katgerman and D. Eskin, "Hardening, Annealing, and Ageing," in *Handbook of Aluminum Volume 1 - Physical Metallurgy and Processes* (G. E. Totten and D. S. MacKenzie, eds.), ch. 5, pp. 259–303, New York, USA: Marcel Dekker, Inc., 2003.

[47] A. Deschamps, T. J. Bastow, F. De Geuser, A. J. Hill, and C. R. Hutchinson, "In situ evaluation of the microstructure evolution during rapid hardening of an Al-2.5Cu-1.5Mg (wt.%) alloy," *Acta Materialia*, vol. 59, no. 8, pp. 2918–2927, 2011.

[48] G. Edwards, K. Stiller, G. Dunlop, and M. Couper, "The precipitation sequence in Al-Mg-Si alloys," *Acta Materialia*, vol. 46, no. 11, pp. 3893–3904, 1998.

[49] S. Pogatscher, H. Antrekowitsch, H. Leitner, T. Ebner, and P. J. Uggowitzer, "Mechanisms controlling the artificial aging of Al-Mg-Si Alloys," *Acta Materialia*, vol. 59, no. 9, pp. 3352–3363, 2011.

[50] M. W. Zandbergen, Q. Xu, A. Cerezo, and G. D. W. Smith, "Study of precipitation in Al-Mg-Si alloys by Atom Probe Tomography I. Microstructural changes as a function of ageing temperature," *Acta Materialia*, vol. 101, pp. 136–148, 2015.

[51] K. Matsumoto, Y. Aruga, H. Tsuneishi, H. Iwai, M. Mizuno, and H. Araki, "Effects of Zn addition and aging conditions on serrated flow in Al-Mg alloys," *Materials Science Forum*, vol. 794-796, pp. 483–488, 2014.

[52] M. Kumar, C. Poletti, and H. P. Degischer, "Precipitation kinetics in warm forming of AW-7020 alloy," *Materials Science and Engineering A*, vol. 561, pp. 362–370, 2013.

[53] J. Zhong, Z. Zheng, and X. Luo, "A new ultrahigh strength Al-Cu-Li alloy," *Materials Science Forum*, vol. 794-796, pp. 1050–1056, 2014.

[54] Y. Filatov, V. Yelagin, and V. Zakharov, "New Al-Mg-Sc alloys," *Materials Science and Engineering A*, vol. 280, pp. 97–101, 2000.

[55] E. Nes, "Modelling of work hardening and stress saturation in FCC metals," *Progress in Materials Science*, vol. 41, no. 3, pp. 129–193, 1998.

[56] A. Rollett and U. F. Kocks, "A review of the stages of work hardening," *Solid State Phenomena*, vol. 35-36, pp. 1–18, 1994.

[57] U. F. Kocks and H. Mecking, "Physics and phenomenology of strain hardening: The FCC case," *Progress in Materials Science*, vol. 48, no. 3, pp. 171–273, 2003.

[58] B. Verlinden, J. Driver, I. Samajdar, and R. Doherty, *Thermo-mechanical processing of metallic materials*. Oxford, UK: Pergamon, 2007.

[59] T. Schulthess, P. Turchi, A. Gonis, and T.-G. Nieh, "Systematic Study

of Stacking Fault Energies of Random Al-based Alloys," *Acta Materialia*, vol. 46, no. 6, pp. 2215–2221, 1998.

[60] T. Morishige, T. Hirata, T. Uesugi, Y. Takigawa, M. Tsujikawa, and K. Higashi, "Effect of Mg content on the minimum grain size of Al-Mg alloys obtained by friction stir processing," *Scripta Materialia*, vol. 64, no. 4, pp. 355–358, 2011.

[61] W. Poole, J. Embury, and D. LLoyd, "Work hardening in aluminium alloys," in *Fundamentals of Aluminium Metallurgy* (R. Lumley, ed.), ch. 11, pp. 307–344, Philadelphia, USA: Woodhead Publishing Ltd, 2011.

[62] W. Mao, "Recrystallization and Grain Growth," in *Handbook of Aluminum Volume 1 - Physical Metallurgy and Processes* (G. E. Totten and D. S. MacKenzie, eds.), ch. 4, pp. 211–258, New York, USA: Marcel Dekker, Inc., 2003.

[63] K. Lo, C. Shek, and J. Lai, "Recent developments in stainless steels," *Materials Science and Engineering: R: Reports*, vol. 65, pp. 39–104, may 2009.

[64] R. Doherty, D. Hughes, F. Humphreys, J. Jonas, D. Jensen, M. Kassner, W. King, T. McNelley, H. McQueen, and A. Rollett, "Current issues in recrystallization: a review," *Materials Science and Engineering: A*, vol. 238, no. 2, pp. 219–274, 1997.

[65] E. Nes, N. Ryum, and O. Hunderi, "On the Zener drag," *Acta Metallurgica*, vol. 33, no. 1, pp. 11–22, 1985.

[66] F. J. Humphreys and M. Hatherly, *Recrystallization and related annealing phenomena*. Pergamon, 1996.

[67] D. Tsivoulas and P. B. Prangnell, "The effect of Mn and Zr dispersoid-forming additions on recrystallization resistance in Al-Cu-Li AA2198 sheet," *Acta Materialia*, vol. 77, pp. 1–16, 2014.

[68] P. A. Manohar, M. Ferry, and T. Chandra, "Five Decades of the Zener Equation," *ISIJ International*, vol. 38, no. 9, pp. 913–924, 1998.

[69] D. Ke, L. Hengcheng, J. Qiumin, and T. Yun, "Effect of hot extrusion on mechanical properties and microstructure of near eutectic Al-12.0%Si-0.2%Mg alloy," *Materials Science and Engineering A*, vol. 527, no. 26, pp. 6887–6892, 2010.

[70] F. Humphreys, "The nucleation of recrystallization at second phase particles in deformed aluminium," *Acta Metallurgica*, vol. 25, pp. 1323–1344, 1977.

[71] A. Sverdlin, "Properties of Pure Aluminum," in *Handbook of Aluminum Volume 1 - Physical Metallurgy and Processes* (G. E. Totten and D. S. MacKenzie, eds.), ch. 2, pp. 33–80, New York, NY: Marcel Dekker, Inc., 2003.

[72] A. Sverdlin, "Introduction to Aluminum," in *Handbook of Aluminum Volume 1 - Physical Metallurgy and Processes* (G. E. Totten and D. S. MacKenzie, eds.), ch. 1, pp. 1–32, New York, USA: Marcel Dekker, Inc., 2003.

[73] G. E. Totten and D. S. MacKenzie, eds., *Handbook of Aluminum Volume 1 - Physical Metallurgy and Processes*. New York, USA: Marcel Dekker, Inc., 2003.

[74] G. E. Totten and D. S. MacKenzie, eds., *Handbook of Aluminum Volume 2 - Alloy Production and Materials Manufacturing*. New York, USA: Marcel Dekker, Inc., 2003.

[75] "www.scandium.org - Scandium Information Center, retrieved: 2013-07-17."

[76] G. Cacciamani, P. Riani, G. Borzone, N. Parodi, A. Saccone, R. Ferro, A. Pisch, and R. Schmid-Fetzer, "Thermodynamic measurements and assessment of the Al-Sc system," *Intermetallics*, vol. 7, no. 1, pp. 101–108, 1999.

[77] V. Davydov and T. Rostova, "Scientific principles of making an alloying addition of scandium to aluminium alloys," *Materials Science and Engineering A*, vol. 280, pp. 30–36, 2000.

[78] K. Hyde, A. Norman, and P. Prangnell, "The effect of cooling rate on the morphology of primary Al_3Sc intermetallic particles in Al-Sc alloys," *Acta Materialia*, vol. 49, pp. 1327–1337, 2001.

[79] A. Norman, P. Prangnell, and R. McEwen, "The solidification behaviour of dilute aluminium-scandium alloys," *Acta Materialia*, vol. 46, no. 16, pp. 5715–5732, 1998.

[80] S. Costa, H. Puga, J. Barbosa, and A. Pinto, "The effect of Sc additions

on the microstructure and age hardening behaviour of as cast Al-Sc alloys," *Materials and Design*, vol. 42, pp. 347–352, 2012.

[81] G. Novotny and A. Ardell, "Precipitation of Al_3Sc in binary Al-Sc alloys," *Materials Science and Engineering A*, vol. 318, pp. 144–154, 2001.

[82] M. Jones and F. Humphreys, "Interaction of recrystallization and precipitation: The effect of Al_3Sc on the recrystallization behaviour of deformed aluminium," *Acta Materialia*, vol. 51, pp. 2149–2159, may 2003.

[83] V. V. Zakharov, "Stability of the solid solution of scandium in aluminium," *Metal Science and Heat Treatment*, vol. 39, no. 1-2, pp. 61–66, 1997.

[84] S. Iwamura and Y. Miura, "Loss in coherency and coarsening behavior of Al_3Sc precipitates," *Acta Materialia*, vol. 52, no. 3, pp. 591–600, 2004.

[85] R. Hyland, "Homogeneous nucleation kinetics of Al_3Sc in a dilute Al-Sc alloy," *Metallurgical Transactions A*, vol. 23, no. July, pp. 1947–1955, 1992.

[86] E. A. Marquis and D. N. Seidman, "Nanoscale structural evolution of Al_3Sc precipitates in Al(Sc) alloys," *Acta Materialia*, vol. 49, no. 11, pp. 1909–1919, 2001.

[87] N. Belov, A. Alabin, and I. Matveeva, "Optimization of phase composition of Al-Cu-Mn-Zr-Sc alloys for rolled products without requirement for solution treatment and quenching," *Journal of Alloys and Compounds*, vol. 583, pp. 206–213, 2014.

[88] J. Røyset and Y. Riddle, "The Effect of Sc on the Recrystallisation Resistance and Hardness of an Extruded and Subsequently Cold Rolled Al-Mn-Mg-Zr Alloy," in *Proceedings of the 9th International Conference on Aluminium Alloys*, vol. 3, pp. 1210–1215, 2004.

[89] B. Smola, I. Stulikova, V. Ocenasek, and J. Pelcová, "Effect of Sc and Zr additions on the microstructure and age hardening of an AlMg3MnCr alloy: Structure and age hardening of AlMgMnCrScZr," *Materials characterization*, vol. 51, no. 1, pp. 11–20, 2003.

[90] M. Mousavi, C. Cross, and Ø. Grong, "Effect of scandium and titanium-boron on grain refinement and hot cracking of aluminium alloy 7108," *Science and Technology of Welding and Joining*, vol. 4, no. 6, pp. 381–388, 1999.

[91] R. R. Sawtell and C. L. Jensen, "Mechanical properties and microstructures of Al-Mg-Sc alloys.," *Metallurgical Transactions A*, vol. 21, pp. 421–430, 1990.

[92] D. Tsivoulas, J. D. Robson, C. Sigli, and P. B. Prangnell, "Interactions between zirconium and manganese dispersoid-forming elements on their combined addition in Al-Cu-Li alloys," *Acta Materialia*, vol. 60, no. 13-14, pp. 5245–5259, 2012.

[93] J. D. Robson and P. B. Prangnell, "Dispersoid precipitation and process modelling in zirconium containing commercial aluminum alloys," *Acta Materialia*, vol. 49, no. 4, pp. 599–613, 2001.

[94] J. D. Robson and P. B. Prangnell, "Modelling Al_3Zr dispersoid precipitation in multicomponent aluminium alloys," *Materials Science and Engineering A*, vol. 352, no. 1-2, pp. 240–250, 2003.

[95] E. Clouet, L. Laé, T. Epicier, W. Lefebvre, M. Nastar, and A. Deschamps, "Complex precipitation pathways in multicomponent alloys," *Nature materials*, vol. 5, no. 6, pp. 482–488, 2006.

[96] S. Lee, A. Utsunomiya, H. Akamatsu, K. Neishi, M. Furukawa, Z. Horita, and T. G. Langdon, "Influence of scandium and zirconium on grain stability and superplastic ductilities in ultrafine-grained Al-Mg alloys," *Acta Materialia*, vol. 50, no. 3, pp. 553–564, 2002.

[97] K. E. Knipling, R. A. Karnesky, C. P. Lee, D. C. Dunand, and D. N. Seidman, "Precipitation evolution in Al-0.1Sc, Al-0.1Zr and Al-0.1Sc-0.1Zr (at.%) alloys during isochronal aging," *Acta Materialia*, vol. 58, no. 15, pp. 5184–5195, 2010.

[98] K. E. Knipling, D. N. Seidman, and D. C. Dunand, "Ambient- and high-temperature mechanical properties of isochronally aged Al-0.06Sc, Al-0.06Zr and Al-0.06Sc-0.06Zr (at.%) alloys," *Acta Materialia*, vol. 59, no. 3, pp. 943–954, 2011.

[99] B. Forbord, W. Lefebvre, F. Danoix, H. Hallem, and K. Marthinsen, "Three dimensional atom probe investigation on the formation

of Al_3(Sc,Zr)-dispersoids in aluminium alloys," *Scripta Materialia*, vol. 51, no. 4, pp. 333–337, 2004.

[100] C. Fuller, J. Murray, and D. Seidman, "Temporal evolution of the nanostructure of Al(Sc,Zr) alloys: Part I - Chemical compositions of $Al_3(Sc_{1-x}Zr_x)$ precipitates," *Acta Materialia*, vol. 53, no. 20, pp. 5401–5413, 2005.

[101] C. Fuller and D. Seidman, "Temporal evolution of the nanostructure of Al(Sc,Zr) alloys: Part II - coarsening of $Al_3(Sc_{1-x}Zr_x)$ precipitates," *Acta Materialia*, vol. 53, no. 20, pp. 5415–5428, 2005.

[102] W. Lefebvre, F. Danoix, H. Hallem, B. Forbord, A. Bostel, and K. Marthinsen, "Precipitation kinetic of Al_3(Sc,Zr) dispersoids in aluminium," *Journal of Alloys and Compounds*, vol. 470, no. 1-2, pp. 107–110, 2009.

[103] A. Tolley, V. Radmilovic, and U. Dahmen, "Segregation in Al_3(Sc,Zr) precipitates in Al-Sc-Zr alloys," *Scripta Materialia*, vol. 52, no. 7, pp. 621–625, 2005.

[104] M. Kaiser, S. Datta, A. Roychowdhury, and M. Banerjee, "Effect of scandium on the microstructure and ageing behaviour of cast Al-6Mg alloy," *Materials Characterization*, vol. 59, no. 11, pp. 1661–1666, 2008.

[105] Z. Yin, Q. Pan, Y. Zhang, and F. Jiang, "Effect of minor Sc and Zr on the microstructure and mechanical properties of Al-Mg based alloys," *Materials Science and Engineering A*, vol. 280, pp. 151–155, 2000.

[106] J. Røyset and N. Ryum, "Some comments on the misfit and coherency loss of Al_3Sc particles in Al-Sc alloys," *Scripta Materialia*, vol. 52, no. 12, pp. 1275–1279, 2005.

[107] J. Røyset, N. Ryum, D. Bettella, A. Tocco, Z. Jia, J. Solberg, and O. Reiso, "On the addition of precipitation-and work-hardening in an Al-Sc alloy," *Materials Science and Engineering A*, vol. 483, pp. 175–178, 2008.

[108] V. Ocenasek and M. Slamova, "Resistance to recrystallization due to Sc and Zr addition to Al-Mg alloys," *Materials Characterization*, vol. 47, pp. 157–162, 2001.

[109] R. Roumina and C. W. Sinclair, "Recovery kinetics in the presence

of precipitates: The softening response of an Al-Mg-Sc alloy," *Acta Materialia*, vol. 58, no. 1, pp. 111–121, 2010.

[110] J. S. Vetrano, S. M. Bruemmer, L. M. Pawlowski, and I. M. Robertson, "Influence of the particle size on recrystallization and grain growth in Al-Mg-X alloys," *Materials Science and Engineering A*, vol. 238, no. 1, pp. 101–107, 1997.

[111] J. Røyset and N. Ryum, "Precipitation and recrystallization of an Al-Mg-Sc-alloy," in *Proceedings of the 4th International Conference on Aluminium Alloys (ICAA4)*, (Atlanta, GA), pp. 194–201, 1994.

[112] W. Yang, D. Yan, and L. Rong, "The separation of recrystallization and precipitation processes in a cold-rolled Al-Mg-Sc solid solution," *Scripta Materialia*, vol. 68, no. 8, pp. 587–590, 2013.

[113] A. Yamashita, D. Yamaguchi, Z. Horita, and T. G. Langdon, "Influence of pressing temperature on microstructural development in equal-channel angular pressing," *Materials Science and Engineering A*, vol. 287, no. 1, pp. 100–106, 2000.

[114] Z. Horita, M. Furukawa, M. Nemoto, A. Barnes, and T. G. Langdon, "Superplastic forming at high strain rates after severe plastic deformation," *Acta Materialia*, vol. 48, no. 9, pp. 3633–3640, 2000.

[115] H. Akamatsu, T. Fujinami, Z. Horita, and T. G. Langdon, "Influence of rolling on the superplastic behavior of an Al-Mg-Sc alloy after ECAP," *Scripta Materialia*, vol. 44, pp. 759–764, 2001.

[116] M. Furukawa, A. Utsunomiya, K. Matsubara, Z. Horita, and T. G. Langdon, "Influence of magnesium on grain refinement and ductility in a dilute Al-Sc alloy," *Acta Materialia*, vol. 49, pp. 3829–3838, 2001.

[117] S. Komura, P. Berbon, M. Furukawa, Z. Horita, M. Nemoto, and T. G. Langdon, "High strain rate superplasticity in an Al-Mg alloy containing scandium," *Scripta materialia*, vol. 38, no. 12, pp. 1851–1856, 1998.

[118] K. Park, D. Hwang, Y. Lee, Y. Kim, and D. Shin, "High strain rate superplasticity of submicrometer grained 5083 Al alloy containing scandium fabricated by severe plastic deformation," *Materials Science and Engineering A*, vol. 341, no. 1-2, pp. 273–281, 2003.

[119] O. Sitdikov, T. Sakai, E. Avtokratova, R. Kaibyshev, Y. Kimura, and K. Tsuzaki, "Grain refinement in a commercial Al-Mg-Sc alloy under

hot ECAP conditions," *Materials Science and Engineering A*, vol. 444, no. 1-2, pp. 18–30, 2007.

[120] K. Dám, P. Lejček, and A. Michalcová, "In situ TEM investigation of microstructural behavior of superplastic Al-Mg-Sc alloy," *Materials Characterization*, vol. 76, pp. 69–75, 2013.

[121] N. Kumar, R. Mishra, C. Huskamp, and K. Sankaran, "Microstructure and mechanical behavior of friction stir processed ultrafine grained Al-Mg-Sc alloy," *Materials Science and Engineering A*, vol. 528, no. 18, pp. 5883–5887, 2011.

[122] N. Kumar and R. Mishra, "Thermal stability of friction stir processed ultrafine grained AlMgSc alloy," *Materials Characterization*, vol. 74, pp. 1–10, 2012.

[123] I. Charit and R. Mishra, "Low temperature superplasticity in a friction-stir-processed ultrafine grained Al-Zn-Mg-Sc alloy," *Acta Materialia*, vol. 53, no. 15, pp. 4211–4223, 2005.

[124] F. Liu and Z. Ma, "Achieving exceptionally high superplasticity at high strain rates in a micrograined Al-Mg-Sc alloy produced by friction stir processing," *Scripta Materialia*, vol. 59, no. 8, pp. 882–885, 2008.

[125] F. Liu, Z. Ma, and L. Chen, "Low-temperature superplasticity of Al-Mg-Sc alloy produced by friction stir processing," *Scripta Materialia*, vol. 60, no. 11, pp. 968–971, 2009.

[126] A. Gholinia, F. J. Humphreys, and P. B. Prangnell, "Production of ultra-fine grain microstructures in Al-Mg alloys by coventional rolling," *Acta Materialia*, vol. 50, no. 18, pp. 4461–4476, 2002.

[127] R. Kaibyshev, E. Avtokratova, A. Apollonov, and R. Davies, "High strain rate superplasticity in an Al-Mg-Sc-Zr alloy subjected to simple thermomechanical processing," *Scripta Materialia*, vol. 54, no. 12, pp. 2119–2124, 2006.

[128] T. Nieh, L. Hsiung, J. Wadsworth, and R. Kaibyshev, "High strain rate superplasticity in a continuously recrystallized Al-6% Mg-0.3% Sc alloy," *Acta Materialia*, vol. 46, no. 8, pp. 2789–2800, 1998.

[129] Y. F. Shen, R. G. Guan, Z. Y. Zhao, and R. D. K. Misra, "Ultrafine-grained Al-0.2Sc-0.1Zr alloy: The mechanist contribution of nano-sized

precipitates on grain refinement during the novel process of accumulative continuous extrusion," *Acta Materialia*, vol. 100, pp. 247–255, 2015.

[130] M. Nicolas and A. Deschamps, "Characterisation and modelling of precipitate evolution in an Al-Zn-Mg alloy during non-isothermal heat treatments," *Acta Materialia*, vol. 51, no. 20, pp. 6077–6094, 2003.

[131] P. Duwez, "Structure and Properties of Alloys Rapidly Quenched from the Liquid State," in *Rapid Solidification Technology Source Book* (R. Ashbrook, ed.), ch. 1, pp. 3–29, ASM International, 1983.

[132] H. Jones, "Rapid Solidification," in *Non-Equilibrium Processing of Materials* (C. Suryanarayana, ed.), ch. 3, pp. 23–48, Pergamon, 1999.

[133] M. J. Aziz, "Model for solute redistribution during rapid solidification," *Journal of Applied Physics*, vol. 53, no. 2, pp. 1158–1168, 1982.

[134] W. Boettinger, L. Bendersky, S. Coriell, R. Schaefer, and F. Biancaniello, "Microsegregation in rapidly solidified Ag-15wt%Cu," *Journal of Crystal Growth*, vol. 80, pp. 17–25, 1987.

[135] W. Kurz, B. Giovanola, and R. Trivedi, "Microsegregation in rapidly solidified Ag-15wt%Cu," *Journal of Crystal Growth*, vol. 91, no. 1-2, pp. 123–125, 1988.

[136] T. Herding, O. Keßler, and H. W. Zoch, "Spray formed and rolled aluminium-magnesium-scandium alloys with high scandium content," *Materialwissenschaft und Werkstofftechnik*, vol. 38, no. 10, pp. 855–861, 2007.

[137] K. Schmidtke, F. Palm, A. Hawkins, and C. Emmelmann, "Process and mechanical properties: Applicability of a scandium modified Al-alloy for laser additive manufacturing," *Physics Procedia*, vol. 12, no. 12, pp. 369–374, 2011.

[138] P. A. Rometsch, H. Zhong, K. M. Nairn, T. Jarvis, and X. Wu, "Characterization of a laser-fabricated hypereutectic Al-Sc alloy bar," *Scripta Materialia*, vol. 87, pp. 13–16, 2014.

[139] S. Mousavi Anijdan, D. Kang, N. Singh, and M. Gallerneault, "Precipitation behavior of strip cast Al-Mg-0.4Sc-0.15Zr alloy under single and multiple-stage aging processes," *Materials Science and Engineering A*, vol. 640, pp. 275–279, 2015.

[140] D. G. Eskin, *Physical Metallurgy of Direct Chill Casting of Aluminum Alloys*. Taylor and Francis Group, 2008.

[141] H. Schultz, *Electron beam welding*. Cambridge, UK: Abington publishing, 2004.

[142] D. W. Rees, "Plane strain compression of aluminium alloy sheets," *Materials and Design*, vol. 39, pp. 495–503, 2012.

[143] M. Hutchings, P. Withers, T. Holden, and T. Lorentzen, *Introduction to the characterization of residual stress by neutron diffraction*. Taylor and Francis Group, 2005.

[144] V. Randle, "Theoretical framework for electron backscatter diffraction," in *Electron Backscatter Diffraction in Materials Science* (J. Schwartz, M. Kumar, and B. Adams, eds.), ch. 2, New York, USA: Kluwer Academic, 2000.

[145] T. Ezquerra, M. Garcia-Gutierrez, A. Nogales, and M. Gomez, eds., *Applications of Synchrotron Light to Scattering and Diffraction in Materials and Life Sciences*. Heidelberg, Germany: Springer, 2009.

[146] S. Mobilio, F. Boscherini, and C. Meneghini, eds., *Synchrotron Radiation: Basics, Methods and Applicaitons*. Heidelberg, Germany: Springer, 2015.

[147] H. Amenitsch, S. Bernstorff, M. Kriechbaum, D. Lombardo, H. Mio, M. Rappolt, and P. Laggner, "Performance and First Results of the ELETTRA High-Flux Beamline for Small-Angle X-ray Scattering," *Journal of Applied Crystallography*, vol. 30, no. 5, pp. 872–876, 1997.

[148] S. Paddock, ed., *Confocal Microscopy: Methods and Protocols*. New Jersey, USA: Humana Press Inc., 1999.

[149] H. Terasaki and Y. Komizo, "Time-resolved in-situ analysis of phase evolution for the directional solidification of carbon steel weld metal," *Metallurgical and Materials Transactions A*, vol. 37, pp. 1261–1266, 2006.

[150] M. Attallah, H. Terasaki, R. Moat, S. Bray, Y. Komizo, and M. Preuss, "In-Situ observation of primary γ melting in Ni-base superalloy using confocal laser scanning microscopy," *Materials Characterization*, vol. 62, no. 8, pp. 760–767, 2011.

[151] L. Deillon, J. Zollinger, D. Daloz, M. Založnik, and H. Combeau, "In-situ observations of solutal melting using laser scanning confocal microscopy: The Cu/Ni model system," *Materials Characterization*, vol. 97, pp. 125–131, 2014.

[152] S. Nambu, N. Shibuta, M. Ojima, J. Inoue, T. Koseki, and H. Bhadeshia, "In situ observations and crystallographic analysis of martensitic transformation in steel," *Acta Materialia*, vol. 61, no. 13, pp. 4831–4839, 2013.

[153] H. Chen, E. Gamsjäger, S. Schider, H. Khanbareh, and S. Van Der Zwaag, "In situ observation of austenite-ferrite interface migration in a lean Mn steel during cyclic partial phase transformations," *Acta Materialia*, vol. 61, pp. 2414–2424, 2013.

[154] D. Zhang, H. Terasaki, and Y.-I. Komizo, "In situ observation of the formation of intragranular acicular ferrite at non-metallic inclusions in C-Mn steel," *Acta Materialia*, vol. 58, no. 4, pp. 1369–1378, 2010.

[155] P. Wanjara, M. Brochu, and M. Jahazi, "Ti-6Al-4V electron beam weld qualification using laser scanning confocal microscopy," *Materials Characterization*, vol. 54, no. 3, pp. 254–262, 2005.

[156] D. Phelan, M. Reid, N. Stanford, and R. Dippenaar, "In-situ observations of phase transformations in titanium," *Jom*, vol. 58, no. 9, pp. 67–69, 2006.

[157] M. Mirza and C. Sellars, "Modelling the hot plane strain compression test Part 1 - Effect of specimen geometry, strain rate, and friction on deformation," *Materials Science and Technology*, vol. 17, no. 9, pp. 1133–1141, 2001.

[158] L. Sun, M. J. Thomas, B. P. Wynne, E. J. Palmiere, K. P. Mingard, and B. Roebuck, "Mapping microstructure inhomogeneity using electron backscatter diffraction in 316L stainless steel subjected to hot plane strain compression tests," *Materials Science and Technology*, vol. 26, no. 12, pp. 1477–1486, 2010.

[159] P. Uranga, I. Gutiérrez, and B. López, "Determination of recrystallization kinetics from plane strain compression tests," *Materials Science and Engineering A*, vol. 578, pp. 174–180, 2013.

[160] L. Reimer, *Scanning electron microscopy: Physics of image formation and microanalysis*. Heidelberg, Germany: Springer, 2. ed., 1998.

[161] J. Schwartz, M. Kumar, and B. Adams, eds., *Electron Backscatter Diffraction in Materials Science*. New York, USA: Kluwer Academic, 2000.

[162] S. I. Wright, M. M. Nowell, and D. P. Field, "A review of strain analysis using electron backscatter diffraction.," 2011.

[163] D. P. Field, L. T. Bradford, M. M. Nowell, and T. M. Lillo, "The role of annealing twins during recrystallization of Cu," *Acta Materialia*, vol. 55, pp. 4233–4241, 2007.

[164] D. Williams and C. Carter, *Transmission Electron Microscopy: A Textbook for Materials Science*. New York, USA: Springer, 2. ed., 2009.

[165] N. Q. Vo, D. C. Dunand, and D. N. Seidman, "Atom probe tomographic study of a friction-stir-processed Al-Mg-Sc alloy," *Acta Materialia*, vol. 60, no. 20, pp. 7078–7089, 2012.

[166] W. W. Mullins, "Theory of Thermal Grooving," *Journal of Applied Physics*, vol. 28, no. 3, pp. 333–339, 1957.

[167] J. D. Robson, "A new model for prediction of dispersoid precipitation in aluminium alloys containing zirconium and scandium," *Acta Materialia*, vol. 52, no. 6, pp. 1409–1421, 2004.

[168] E. Clouet, A. Barbu, L. Lae, and G. Martin, "Precipitation kinetics of Al_3Zr and Al_3Sc in aluminum alloys modeled with cluster dynamics," *Acta Materialia*, vol. 53, no. 8, pp. 2313–2325, 2005.

[169] J. Røyset and N. Ryum, "Precipitation kinetics and mechanisms in a binary Al-Sc alloy," in *Proceedings of the 6th International Conference on Aluminium Alloys*, pp. 793–798, 1998.

[170] B. Oberdorfer, E. M. Steyskal, W. Sprengel, R. Pippan, M. Zehetbauer, W. Puff, and R. Würschum, "Recrystallization kinetics of ultrafine-grained Ni studied by dilatometry," *Journal of Alloys and Compounds*, vol. 509, pp. S309–S311, 2011.

[171] G. Benchabane, Z. Boumerzoug, I. Thibon, and T. Gloriant, "Recrystallization of pure copper investigated by calorimetry and microhardness," *Materials Characterization*, vol. 59, pp. 1425–1428, 2008.

[172] A. Dhal, S. Panigrahi, and M. Shunmugam, "Precipitation phenomena, thermal stability and grain growth kinetics in an ultra-fine grained Al

2014 alloy after annealing treatment," *Journal of Alloys and Compounds*, vol. 649, pp. 229–238, 2015.

[173] A. Hayoune and D. Hamana, "A dilatometric and high-temperature X-ray diffraction study of cold deformation effect on the interaction between precipitation, recovery and recrystallization reactions in Al-12wt.% Mg alloy," *Materials Science and Engineering A*, vol. 527, no. 27-28, pp. 7261–7264, 2010.

[174] K. D. Liss, U. Garbe, H. Li, T. Schambron, J. D. Almer, and K. Yan, "In situ observation of dynamic recrystallization in the bulk of zirconium alloy," *Advanced Engineering Materials*, vol. 11, no. 8, pp. 637–640, 2009.

[175] K. D. Liss and K. Yan, "Thermo-mechanical processing in a synchrotron beam," *Materials Science and Engineering A*, vol. 528, no. 1, pp. 11–27, 2010.

[176] N. Bozzolo, S. Jacomet, and R. E. Logé, "Fast in-situ annealing stage coupled with EBSD: A suitable tool to observe quick recrystallization mechanisms," *Materials Characterization*, vol. 70, pp. 28–32, 2012.

[177] Y. Jin, B. Lin, M. Bernacki, G. S. Rohrer, A. D. Rollett, and N. Bozzolo, "Annealing twin development during recrystallization and grain growth in pure nickel," *Materials Science and Engineering A*, vol. 597, pp. 295–303, 2014.

[178] A. Yamamoto, M. Tsukamoto, and D. Okai, "Changes in Microstructures during Annealing after Cold-Rolling at 30% and 50% Reduction on Al-Mg-Si Alloy," *Materials Transactions*, vol. 52, no. 5, pp. 876–881, 2011.

[179] P. J. Hurley and F. J. Humphreys, "Modelling the recrystallization of single-phase aluminium," *Acta Materialia*, vol. 51, no. 13, pp. 3779–3793, 2003.

[180] P. Zhang, S. Li, and Z. Zhang, "General relationship between strength and hardness," *Materials Science and Engineering: A*, vol. 529, pp. 62–73, 2011.

[181] M. Tiryakioglu, J. Robinson, M. Salazar-Guapuriche, Y. Zhao, and P. Eason, "Hardness-strength relationships in the aluminum alloy 7010," *Materials Science and Engineering: A*, vol. 631, pp. 196–200, 2015.

[182] J. Taendl, F. Palm, K. Anders, R. Gradinger, and C. Poletti, "Investigation of the precipitation kinetics of a new Al-Mg-Sc-Zr alloy," *Materials Science Forum*, vol. 794-796, pp. 1038–1043, 2014.

[183] J. Taendl, S. Nambu, A. Orthacker, G. Kothleitner, J. Inoue, T. Koseki, and C. Poletti, "In-situ observation of recrystallization in an AlMgScZr alloy using confocal laser scanning microscopy," *Materials Characterization*, vol. 108, pp. 137–144, 2015.

[184] J. Taendl, S. Nambu, J. Inoue, T. Koseki, and C. Poletti, "Kinetics of hardening and softening in an Al-Mg-Sc-Zr alloy: Analyses of the driving pressure and Zener pinning effect," *in submission*, 2016.

[185] J. Taendl, A. Orthacker, H. Amenitsch, G. Kothleitner, and C. Poletti, "Influence of the degree of scandium supersaturation on the precipitation kinetics of rapidly solidified Al-Mg-Sc-Zr alloys," *Acta Materialia*, vol. 117, pp. 43–50, 2016.

[186] J. Taendl, M. Dikovits, and C. Poletti, "Investigation of the hot deformation behavior of an Al-Mg-Sc-Zr alloy under plane strain condition," *Key Engineering Materials*, vol. 611-612, pp. 76–83, 2014.

[187] J. Taendl and C. Poletti, "Influence of Al3(Sc,Zr) Precipitates on Deformability and Friction Stir Welding Behavior of Al-Mg-Sc-Zr Alloys," *BHM Berg- und Hüttenmännische Monatshefte*, vol. 161, no. 7, pp. 330–333, 2016.

[188] M. Dikovits, J. Taendl, and C. Poletti, "Study of the deformation behaviour of a rapidly solidified Al-Mg-Sc-Zr alloy," *in submission*, 2016.

[189] J. Taendl and C. Poletti, "Characterization of electron beam and friction stir welds in a novel Al-Mg-Sc-Zr alloy," in *Proceedings of the 10th International Conference on Trends in Welding Research*, 2016.

[190] R. Cook, P. G. Grocock, P. M. Thomas, D. V. Edmonds, and J. D. Hunt, "Development of the twin-roll casting process," *Journal of Materials Processing Tech.*, vol. 55, no. 2, pp. 76–84, 1995.

[191] T. Haga, K. Tkahashi, M. Ikawaand, and H. Watari, "Twin roll casting of aluminum alloy strips," *Journal of Materials Processing Technology*, vol. 153-154, no. 1-3, pp. 42–47, 2004.

[192] M. Yun, S. Lokyer, and J. Hunt, "Twin roll casting of aluminium al-

loys," *Materials Science and Engineering: A*, vol. 280, pp. 116–123, 2000.

[193] J. Zhao, F. Jiang, H. Jian, K. Wen, L. Jiang, and X. Chen, "Comparative investigation of tungsten inert gas and friction stir welding characteristics of Al-Mg-Sc alloy plates," *Materials and Design*, vol. 31, no. 1, pp. 306–311, 2010.

[194] A. C. Muñoz, G. Rückert, B. Huneau, X. Sauvage, and S. Marya, "Comparison of TIG welded and friction stir welded Al-4.5Mg-0.26Sc alloy," *Journal of Materials Processing Technology*, vol. 197, no. 1-3, pp. 337–343, 2008.

[195] X. Sauvage, A. Dédé, A. C. Muñoz, and B. Huneau, "Precipitate stability and recrystallisation in the weld nuggets of friction stir welded Al-Mg-Si and Al-Mg-Sc alloys," *Materials Science and Engineering A*, vol. 491, no. 1-2, pp. 364–371, 2008.

[196] Y. Tao, Z. Zhang, D. Ni, D. Wang, B. Xiao, and Z. Ma, "Influence of welding parameter on mechanical properties and fracture behavior of friction stir welded Al-Mg-Sc joints," *Materials Science and Engineering A*, vol. 612, pp. 236–245, 2014.

[197] P. L. Threadgill, "Terminology in friction stir welding," *Science and Technology of Welding and Joining*, vol. 12, pp. 357–360, may 2007.

[198] S. Jambu, B. Lenczowski, R. Rauh, and K. Juhl, "Creep forming of AlMgScZr alloys for aeronautic and space applications," in *ICAS 2002 Congress*, (Toronto, CA), pp. 632.1 – 632.7, 2002.